

**Development of
mechanical-hydraulic
models for the prediction
of the long-term sealing
capacity of concrete
based sealing materials
in rock salt**

Supported by:



Federal Ministry
for Economic Affairs
and Energy

on the basis of a decision
by the German Bundestag

**Development of
mechanical-hydraulic
models for the prediction
of the long-term sealing
capacity of concrete
based sealing materials
in rock salt**

Project Titel LASA

Oliver Czaikowski
Jürgen Dittrich
Uwe Hertes
Kyra Jantschik
Klaus Wieczorek
Bernd Zehle

August 2016

Remark:

The underlying work of this report has received funding from the German Federal Ministry of Economic Affairs and Energy (BMWi) under contract no. 02E11132

The work was conducted by the Gesellschaft für Anlagen- und Reaktorsicherheit (GRS) gGmbH.

The authors are responsible for the content of this report.

Keywords:

rock salt, concrete based sealing materials, salt concrete, HM behaviour

Foreword

The research work leading to these results has received funding from the German Federal Ministry of Economic Affairs and Energy (BMWi) under contract no. 02E11132.

This report presents the current state of laboratory investigations and modelling activities related to the LASA project. The work is related to the research and development of plugging and sealing for repositories in salt rock and is of fundamental importance for the salt option which represents one of the three European repository options in addition to the clay rock and the crystalline rock options.

Table of contents

1	Introduction.....	1
2	Testing material	3
3	Laboratory experiments	5
3.1	Material stability – triaxial compression test	5
3.1.1	Experimental layout	5
3.1.2	Testing procedure.....	7
3.1.3	Measurement results and interpretation	11
3.2	Multi-stage triaxial compression test	14
3.2.1	Experimental layout	14
3.2.2	Testing procedure.....	14
3.2.3	Measurement results and interpretation	15
3.3	Long-term deformation behaviour – uniaxial-testing method.....	20
3.3.1	Experimental layout	20
3.3.2	Testing procedure.....	21
3.3.3	Measurement results and interpretation	23
3.4	Long-term deformation behaviour – triaxial-testing method.....	27
3.4.1	Experimental layout	27
3.4.2	Testing procedure.....	28
3.4.3	Measurement results and interpretation	30
3.5	Long-term deformation behaviour – temperature effects.....	33
3.5.1	Experimental layout	33
3.5.2	Testing procedure.....	34
3.5.3	Measurement results and interpretation	36
3.6	Sealing capacity of rock salt / sealing system	38
3.6.1	Experimental layout	38
3.6.2	Testing procedure.....	40
3.6.3	Measurement results and interpretation	40
4	Modelling work.....	45

4.1	Physical Modelling	45
4.2	Numerical simulation of the triaxial compression test.....	48
4.2.1	Model geometry	48
4.2.2	Boundary conditions and material properties	49
4.2.3	Modelling results versus experimental data	52
4.2.4	Discussion	61
4.3	Simulation of the uniaxial creep test.....	63
4.3.1	Model geometry.....	63
4.3.2	Boundary conditions and material properties	64
4.3.3	Modelling results versus experimental data	66
4.3.4	Discussion	92
4.4	Simulation of the triaxial creep test	95
4.4.1	Model geometry.....	95
4.4.2	Boundary conditions and material properties	96
4.4.3	Modelling results versus experimental data	98
4.4.4	Discussion	111
5	Summary and outlook.....	114
6	Zusammenfassung und Ausblick.....	116
7	Acknowledgements	118
	References	119
	Figures	122
	Tables	130

1 Introduction

The research work leading to these results has received funding from the German Federal Ministry of Economic Affairs and Energy (BMWi) under contract no. 02E11132 and from the European Union's European Atomic Energy Community's (Euratom) Seventh Framework Programme FP7/2007-2013 under Grant agreement no. 323273, the DOPAS project.

This report presents the final state of laboratory investigations and modelling activities related to the LASA project. LASA was performed by GRS as part of the European project DOPAS (Full Scale Demonstration of Plugs and Seals) under WP 3 task 2 and WP 5 task 1 on “Design and technical construction feasibility of the plugs and seals” and “Performance assessment of plugs and seal systems”. The work is related to the research and development of plugging and sealing for repositories in salt rock and is of fundamental importance for the salt option which represents one of the three European repository options in addition to the clay rock and the crystalline rock options.

In the German concept for the final disposal of radioactive and hazardous wastes in salt formations, cements and cement-based systems are proposed as technical barriers (shaft and drift seals). Due to the specific boundary conditions in salt host rock formations these materials (salt and sored concretes) contain crushed salt instead of sand or gravel. The programme aims at providing experimental data needed for the theoretical analysis of the long-term sealing capacity of these sealing materials.

In order to demonstrate hydro-mechanical material stability under representative load scenarios, the long-term deformation material behaviour as well as the sealing capacity of the seal, a comprehensive laboratory testing programme is carried out.

One of the most challenging aspects is the determination of the pre-experimental status of the core material that was provided for laboratory investigations, since the salt concrete was taken from an existing dam that has been loaded in situ by creeping rock salt for more than 10 years. Therefore, it is obvious that material properties, such as e.g. the initial gas permeability, have to be measured under a load which is comparable to the in situ minimum stress.

This final technical GRS-report at hand summarises the work and results achieved in the DOPAS tasks 3.2 and 5.1 during the whole 4-years project lifetime and supersedes the previous technical report (D3.31) /CZA 16/.

Chapter 2 gives a short overview of the core material that was provided for laboratory investigations. The status of the laboratory experiments on the salt concrete samples is illustrated in chapter 3. The modelling work is reported on in chapter 4. The summary and the outlook on the further work programme is given in chapter 5.

2 Testing material

Salt concrete is a mass concrete that is used for the construction of dam structures or for the backfilling of drifts in rock salt. The backfilling of excavations and construction of dam structures aims to receive the integrity of the geological barrier, to stabilize the disturbed rock zone at the contour and to limit and decelerate the inflow of brine.

There are different mixtures of salt concrete, like the salt concrete M1 and M2 used in ERAM (Morsleben repository) or the type "Asse", which was used in the Asse mine. In the context of this work the numerical simulations are conducted on the basis of laboratory tests on specimens from the salt concrete type "Asse".

The composition of salt concrete consists of a matrix from cement with inclusion of crushed salt. The proportion is defined in Tab. 2.1.

Tab. 2.1 Composition of salt concrete type „Asse“ related to 1 m³/MÜL 10/

Component of salt concrete	Proportion in [kg/m ³]	Proportion in mass-%
Blast furnace cement	380	18.3
Crushed salt	1 496	72.1
NaCl-brine	198	9.6
Total	2 074	100.0

The specimens for the uniaxial and triaxial tests were extracted from the in situ construction "Asse-Vordamm". The drift sealing element was constructed at the 945 m level from November 1991 to January 1992 /STA 94/. Its dimensions are 8.0 m in length, 5.5 m in width and 3.4 m in height. The "Asse-Vordamm" constitutes only a part of the whole dam structure, which was constructed in the Asse as shown in Fig. 2.1.

The sealing element is composed of three devices: the salt concrete itself, the contact zone between concrete and host rock and the excavation damaged zone (EDZ). The specimens used by GRS for the laboratory tests were extracted from boreholes B4 and B5 (compare to Fig. 2.2).

At this time the salt concrete was exposed to the convergence of the rock salt for about ten years.

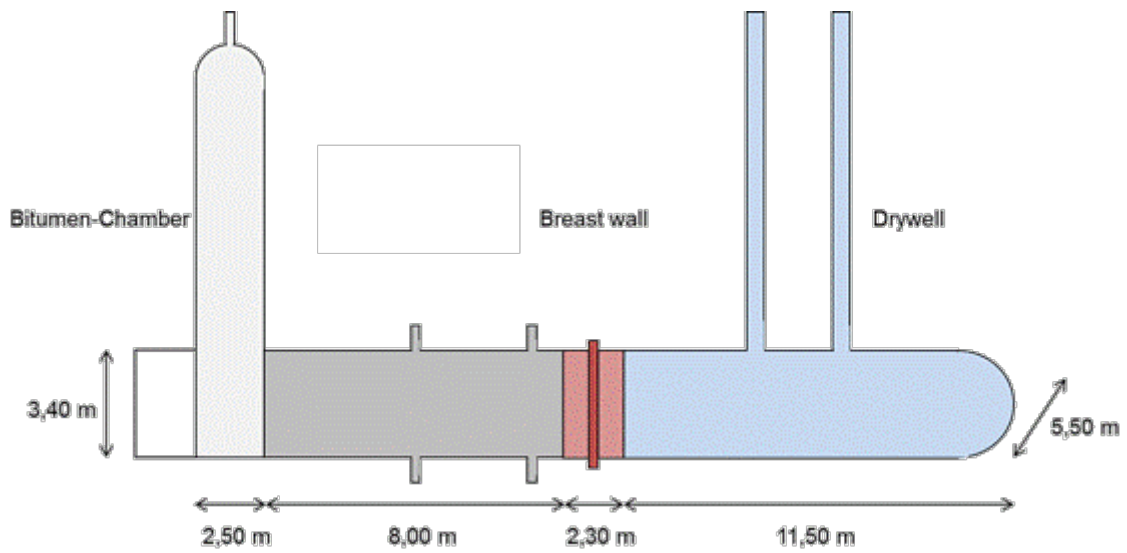


Fig. 2.1 Simplified illustration of the whole dam structure

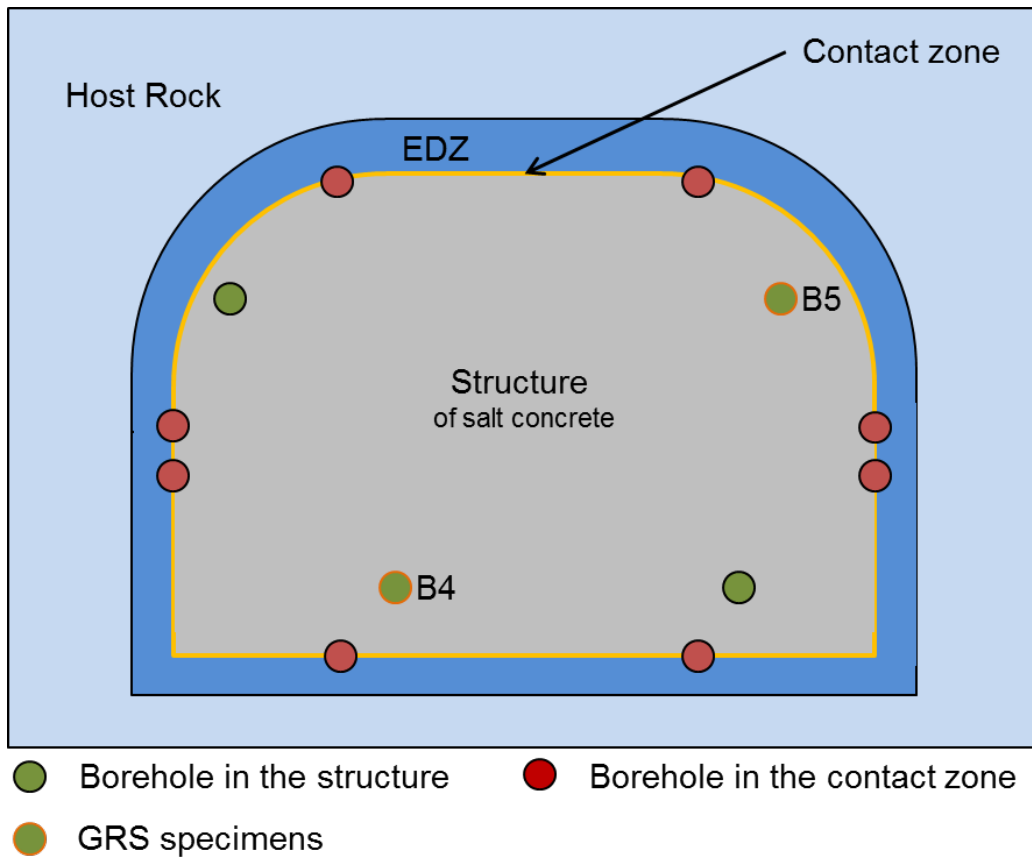


Fig. 2.2 Definition of the three devices of a sealing element and identification of the boreholes

3 Laboratory experiments

3.1 Material stability – triaxial compression test

3.1.1 Experimental layout

Damage tests were carried out on salt concrete samples in a triaxial apparatus with measurement of deformation and gas permeability under various stress conditions. From the pictures in Fig. 3.1 one can clearly recognize the open voids marked in red and filled with resin during the sample preparation procedure.

The average porosity of the samples is about $\phi = 6\%$ with a grain density of $2.17 - 2.2 \text{ g/cm}^3$. The average water content is at a level of $w = 2$ weight-%.



Sample B4KK3-P1

Sample B4KK3-P3

Sample B4KK4-P6

Fig. 3.1 Salt concrete samples before testing

Fig. 3.2 illustrates schematically the assembly of a sample in a triaxial cell. The sample was isolated in a jacket and porous discs at top and bottom.

The samples were subjected to two phases with different loading regimes. The purpose of the initial isostatic pre-compaction phase was to re-establish the intact state of the samples with respect to permeability. It has to be pointed out, though, that no effective healing was expected during the pre-compaction phase. This phase was performed by

simultaneously increasing axial and radial stress to $\sigma_a = \sigma_r = 5$ MPa at a loading rate of 1 MPa/min, then keeping stress constant for 22 hours. After this, the axial and radial stresses were increased twice up to a level of 20 MPa. After 24 hours, the pre-compaction phase ended. The idea of this pre-compaction phase is to reach the state of compaction that the specimens had before extraction from the drift sealing element.

In the second step of the test the specimens were deformed under deviatoric stress. For that purpose, three specimens were subjected to three confining stresses of 1 to 5 MPa. The axial stress was increased until the failure load level of the sample was reached. A low strain rate of $\dot{\epsilon}_a = 1 \cdot 10^{-7} \text{ s}^{-1}$ was applied.

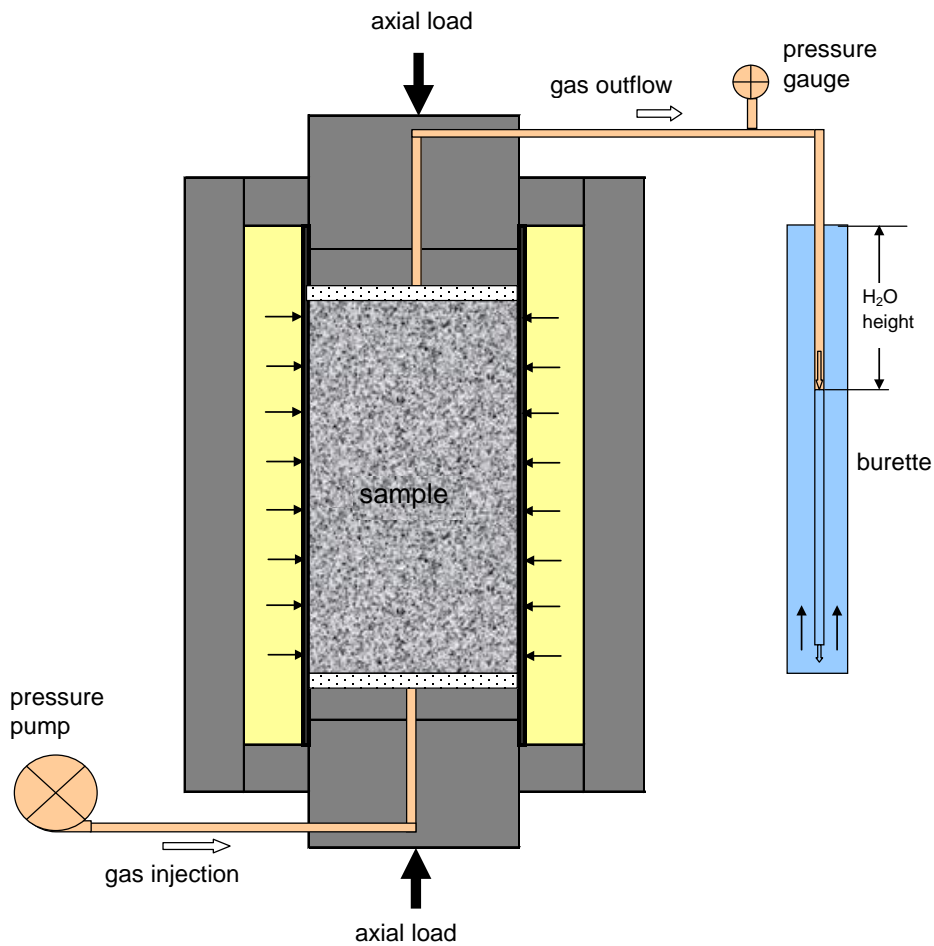


Fig. 3.2 Principle of triaxial compression tests with permeability measurement

During the load tests, axial strain was measured by a displacement-transducer installed outside of the cell, while volumetric strain was determined both directly from the volume change of the confining oil in the cell by using a pressure/volume controller and indirectly by strain gauges attached on the sample surface at the middle of the length.

Permeability changes induced by the mechanical loading were measured along the sample axis by injecting dry nitrogen gas to the bottom at constant pressure and recording the outflow on the opposite side. The gas outflow was continuously recorded by using a burette. During steady state gas flow, the permeability is determined according to Darcy's law for compressive media (eq. 3.1):

$$k = \frac{2 \cdot Q \cdot \mu \cdot L \cdot p_o}{A \cdot (p_g^2 - p_o^2)} \quad (3.1)$$

where k is the intrinsic permeability (m^2), Q is the flow rate of the gas (m^3/s), μ is the gas dynamic viscosity ($\text{Pa}\cdot\text{s}$), L is the length of the sample (m), A is the cross section of the sample (m^2), p_o is the atmospheric pressure (Pa), p_g is the gas injection pressure (Pa). The measuring system allows a precise determination of low permeabilities down to $\sim 1 \cdot 10^{-21} \text{ m}^2$.

3.1.2 Testing procedure

Triaxial compression tests (TC-Test) were performed in order to investigate the mechanical stability of salt concrete with respect to its sealing capacity. Onset of dilatancy, start of gas flux and failure of the samples were determined under different radial stresses. The results of the TC-Tests aim at a better understanding of the onset of gas flux and development of permeability during deformation.

The tests were performed on 9 samples under stress control in the GRS laboratory. The samples for the triaxial compaction tests had a diameter of 70 mm and a length of 140 mm before testing and had been obtained by core-drilling from a real plug installed in a salt mine.

In the first step, the samples were compacted for about 22 hours at an isotropic stress level of 5 MPa. Then, the axial and radial stresses were increased twice up to a level of 20 MPa. After 24 hours, the compaction phase ended. The idea of this compaction phase is to reach the state of compaction that the samples had before extraction from the drift sealing element, see Fig. 3.3, Fig. 3.4 and Fig. 3.5.

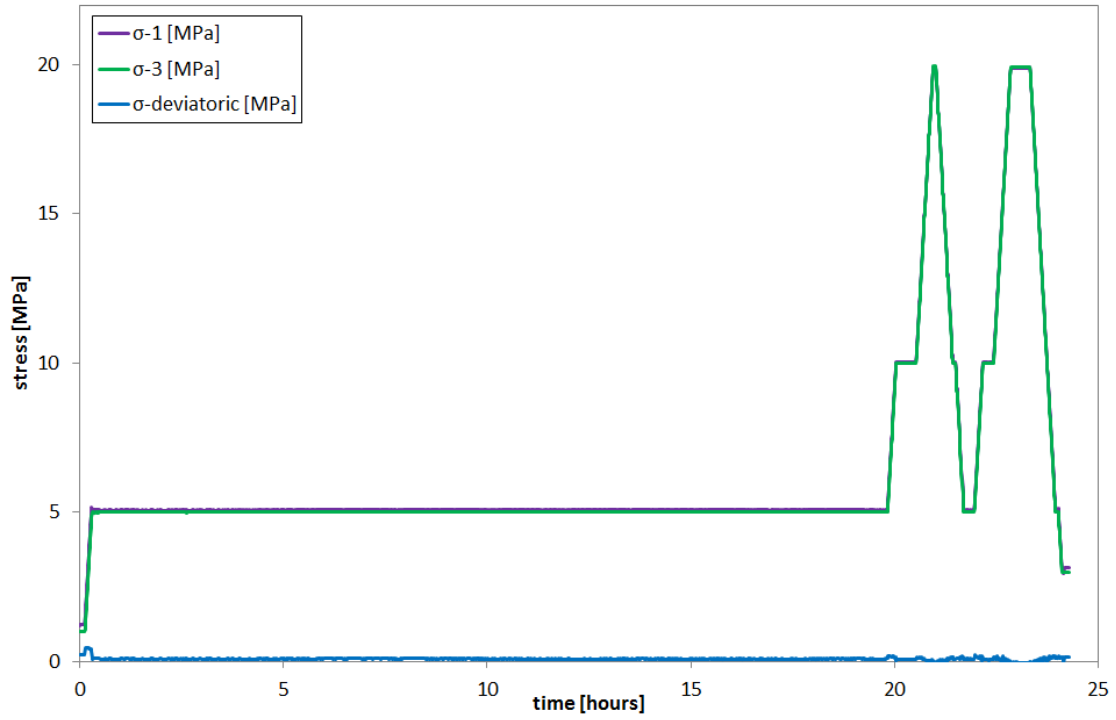


Fig. 3.3 Stress evolution of a salt concrete sample under isostatic compaction

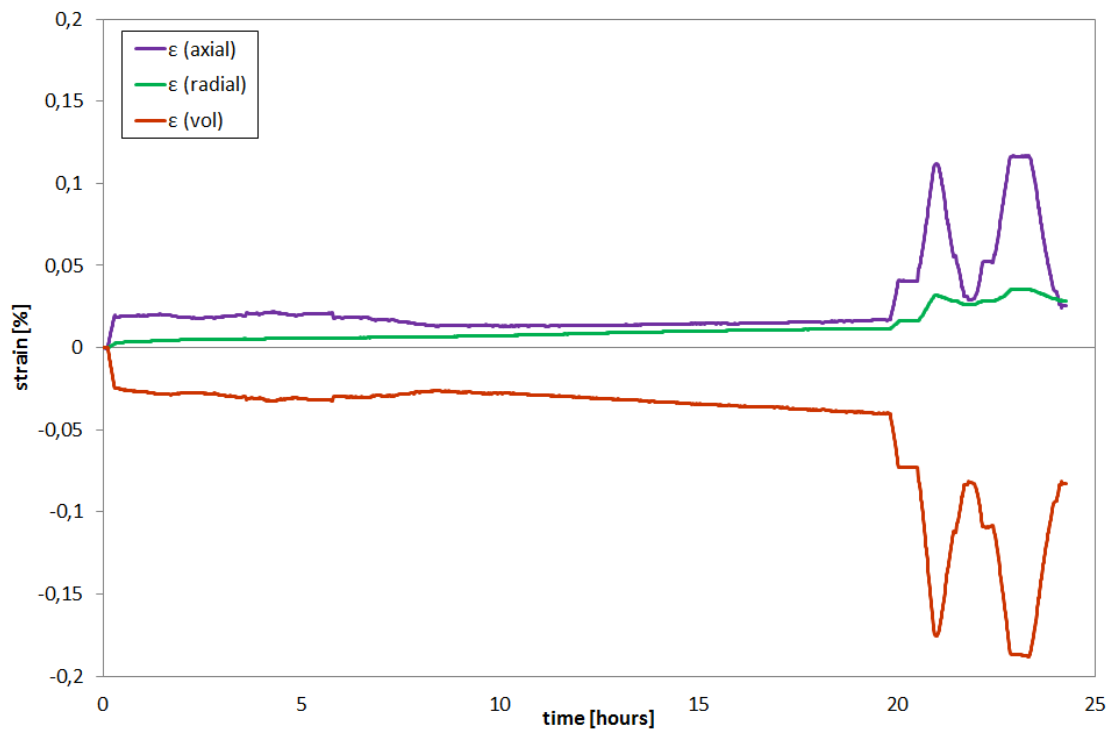


Fig. 3.4 Strain evolution of a salt concrete sample under isostatic compaction

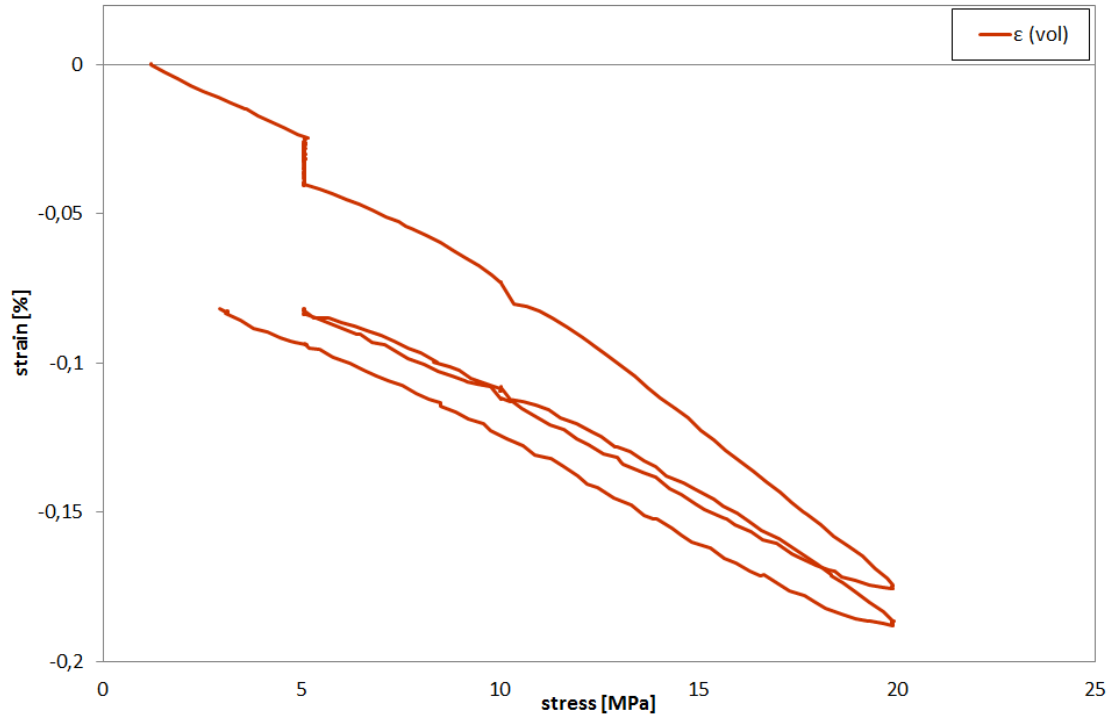


Fig. 3.5 Isostatic pre-compaction behaviour of a salt concrete sample

Second step of the test was to deform the samples under deviatoric stress. For that purpose, eight samples were subjected to confining stresses of 1-5 MPa. The tests were performed under strain control and loaded until the failure load level of the sample was reached. During the tests gas was injected in axial direction for permeability measurement.

Tab. 3.1 Test samples that were subjected to confining stresses of 1-5 MPa

Sample name	B4KK1 - 0.68	B4KK1 - 1.38	B4KK3 P2	B4KK4 P5	B4KK4 P8	B4KK4 P10	B4KK4 P12	B4KK4 P13
Confining stress	4	1	2	2	2	3	3	5

The results of the TC-Tests with a confining stress of 3 MPa are presented in Fig. 3.6. Full deformation behaviour is exemplified in one sample as the other samples behave very similarly. The difference lies in the failure point, the dilatancy boundary and the onset of gas flux. In the figure, the deviatoric stress and the volumetric strain are shown versus the axial strain. The deviatoric stress increases up to a stress level of 40.3 MPa.

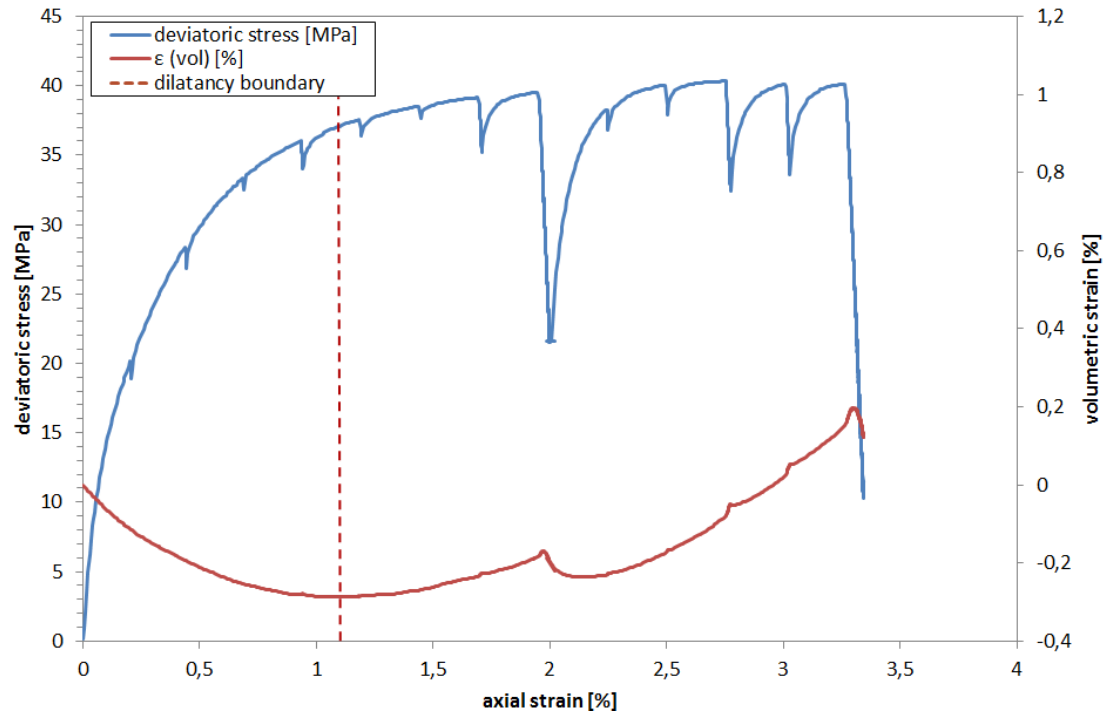


Fig. 3.6 Stress-strain behaviour of a salt concrete sample B4KK4 P10 deformed by deviatoric loading at confining stress of 3 MPa

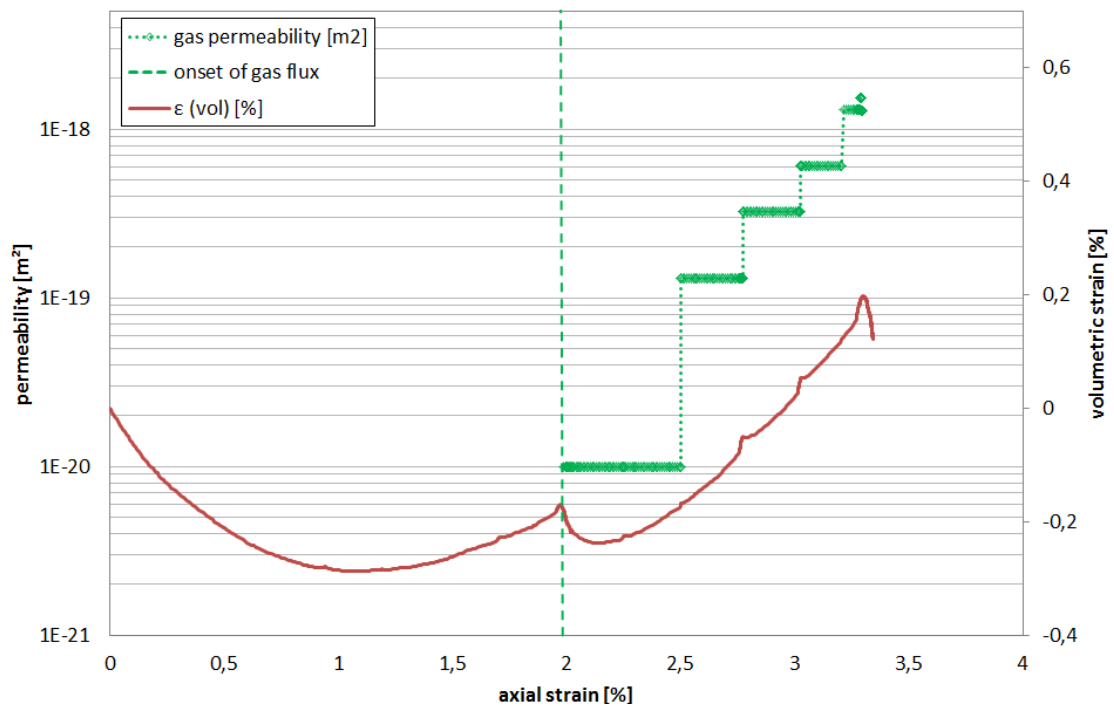


Fig. 3.7 Strain-permeability behaviour of a salt concrete sample B4KK4 P10 deformed by deviatoric loading at confining stress of 3 MPa

The failure stress is reached at an axial strain of 2.75 %. Gas permeability measurements are performed continuously while axial deformation is kept constant. The volumetric strain decreases in the beginning of the test, due to the compaction of the sample. Volumetric strain starts to increase when axial strain reaches values of about 1.1 %. This point is defined as the dilatancy boundary, which is marked by formation of micro cracks leading to volumetric extension. At this point, the deviatoric stress is about 37.2 MPa. By ongoing increase of deviatoric stress the micro cracking and the sample volume increases further. At an axial strain of 2 %, an onset of gas flow could be detected (Fig. 3.7), which implies that a connection of the micro cracks enables percolation.

3.1.3 Measurement results and interpretation

The results of the triaxial compression tests show that salt concrete exhibits elastic and plastic material behaviour during the compaction phase showing reversible and irreversible deformations. This compaction test phase was identical for all samples.

During the deviatoric stress phase (shown for salt concrete in Fig. 3.8), maximum reached deviatoric stresses clearly depend on the confining pressure. It is possible to identify the onset of dilatancy for each sample by the evolution of volumetric strains (Fig. 3.9). In all tests, the onset of gas flux is measured at higher deviatoric stress levels than the onset of dilatancy (Fig. 3.10). The onset of gas flux occurs during stress relaxation (decrease of deviatoric stress) in some samples. In this case, the correspondent deviatoric stress values of the preceding load maximum were taken, as this is the point where micro cracks are likely to connect. The failure stress of the samples generally increases with higher confining stress, analogue to the dilatancy boundary and the onset of gas flux. However, where multiple measurements were taken at one confining stress level, data strongly deviates. This irregularity might be attributed to differences in samples, as salt concrete is a heterogeneous material. The onset of gas flux coincided with failure for most samples. Only samples B4KK4 P2 and B4KK4 P10 show gas flux at stresses about 2.5 MPa and 1 MPa below the load limit. Data from /CZA 15/ obtained on salt concrete with the same testing procedure is in good agreement with the results of the present study.

Consequently, the test results show that no damage was induced below deviatoric stress of 32 MPa and that gas flux mostly coincides with failure of the sample.

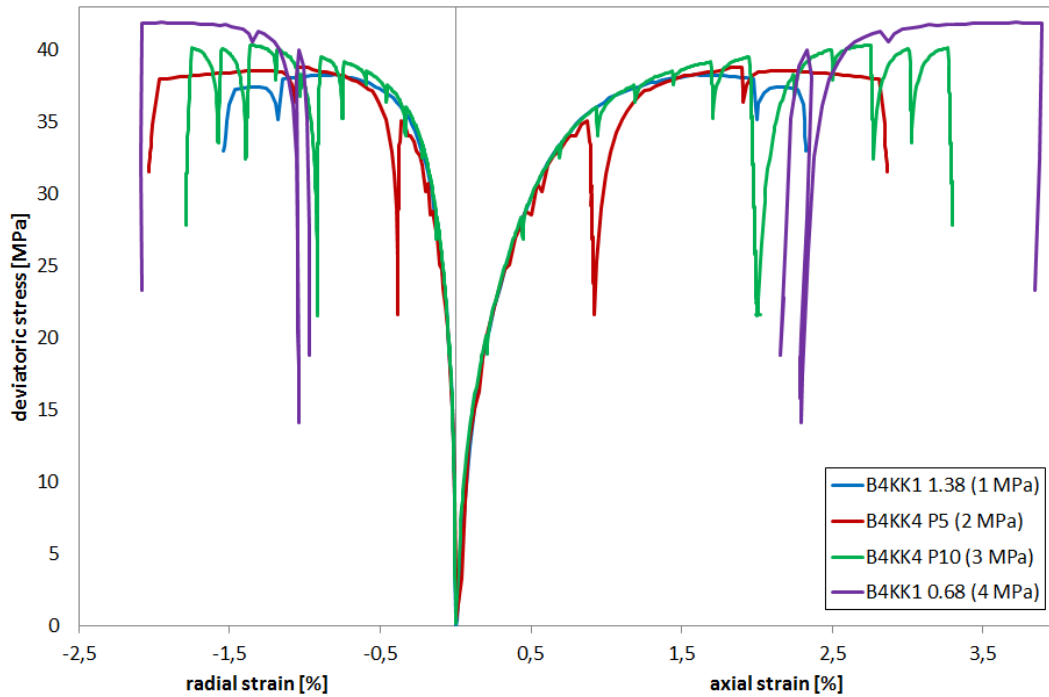


Fig. 3.8 Stress-strain curves obtained on four of the eight salt concrete samples at different confining stresses. *Curve of sample B4KK1 0.68 has been cut at axial strains below 2%, as multiple reloading cycles were executed in this interval, which would confuse the illustration*

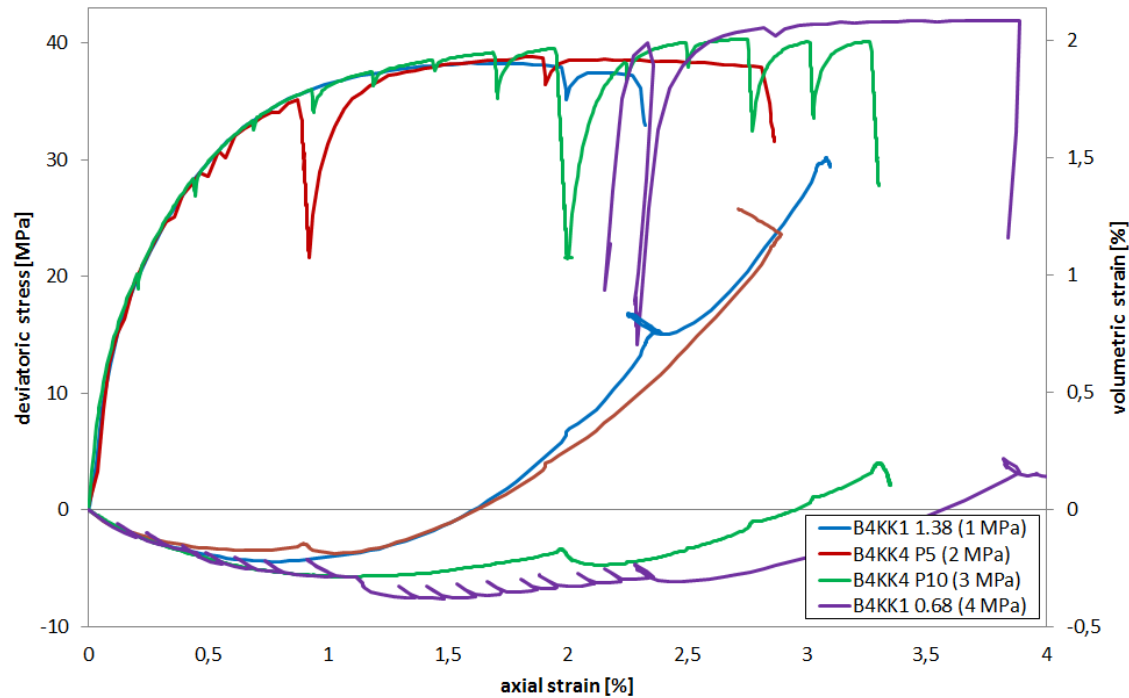


Fig. 3.9 Stress-strain curves obtained on the salt concrete samples at different confining stresses

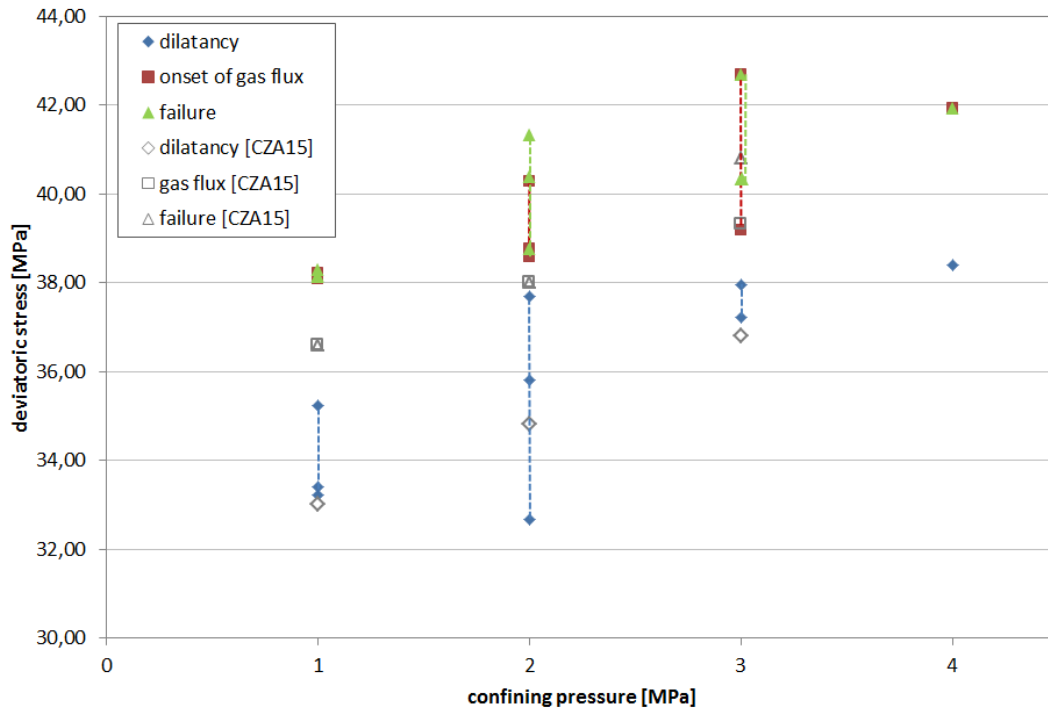


Fig. 3.10 Dilatancy boundary, onset of gas flux and failure of the tested samples compared with data from /CZA 15/. Range of values is indicated by dashed lines

3.2 Multi-stage triaxial compression test

3.2.1 Experimental layout

The experimental layout, pre-compaction testing procedure and sample dimensions are as explained in chapter 3.1.1 and 3.1.2.

3.2.2 Testing procedure

Deviatoric loading was applied at different confining stresses, with a stepwise increase of 1 MPa until the final stage of 5 MPa is reached. During each of these stages, axial stress was increased until a gas flow could be detected. Then deviatoric stress was decreased to 0 MPa every time, before the confining stress was increased. The testing procedure and resulting deformations can be seen in Fig. 3.11. The dilatancy boundary was identified at 33.2 MPa deviatoric stress with the confining stress being 1 MPa.

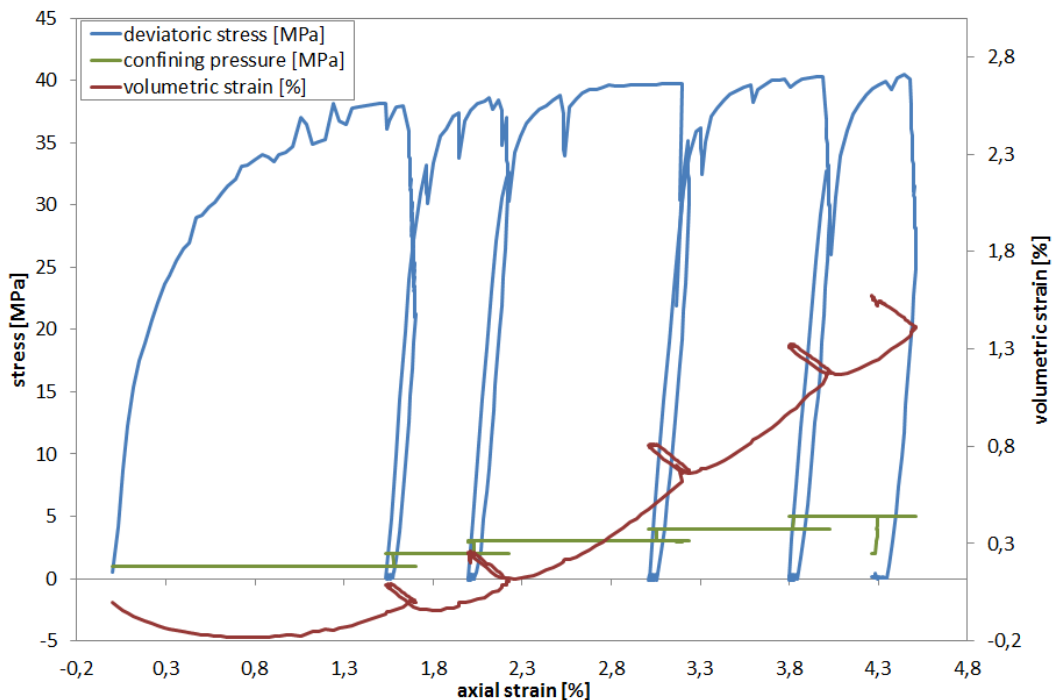


Fig. 3.11 Stress-strain behaviour of salt concrete sample B4KK4 P9 deformed by deviatoric loading at multiple confining stresses

At each increase of confining stress, the sample initially compacts, before volumetric extension by dilatancy is resumed. This occurs at lower deviatoric stress, compared to

the first excess of the dilatancy boundary. The increase in volumetric strain with simultaneous decrease in axial strain at the beginning of each “loop” is due to a relaxation of the material of the triaxial cell during deviatoric stress decrease. The onset of gas flux occurred at 38.1 MPa deviatoric stress, before the load limit was reached. Fig. 3.12 shows the development of permeability with axial strain. Towards the end of the 1 MPa stage, gas flux sets in with a permeability of $3 \cdot 10^{-19} \text{ m}^2$ and increases rapidly. During relaxation, permeability plummets in the order of $1 \cdot 10^{-22} \text{ m}^2$, before it rises again with deviatoric stress increase in the 2 MPa stage. This behaviour repeatedly occurs at each stage. Lower permeability at the beginning of each deviatoric loading can be explained by the initial volumetric compaction observed when confining stress is increased.

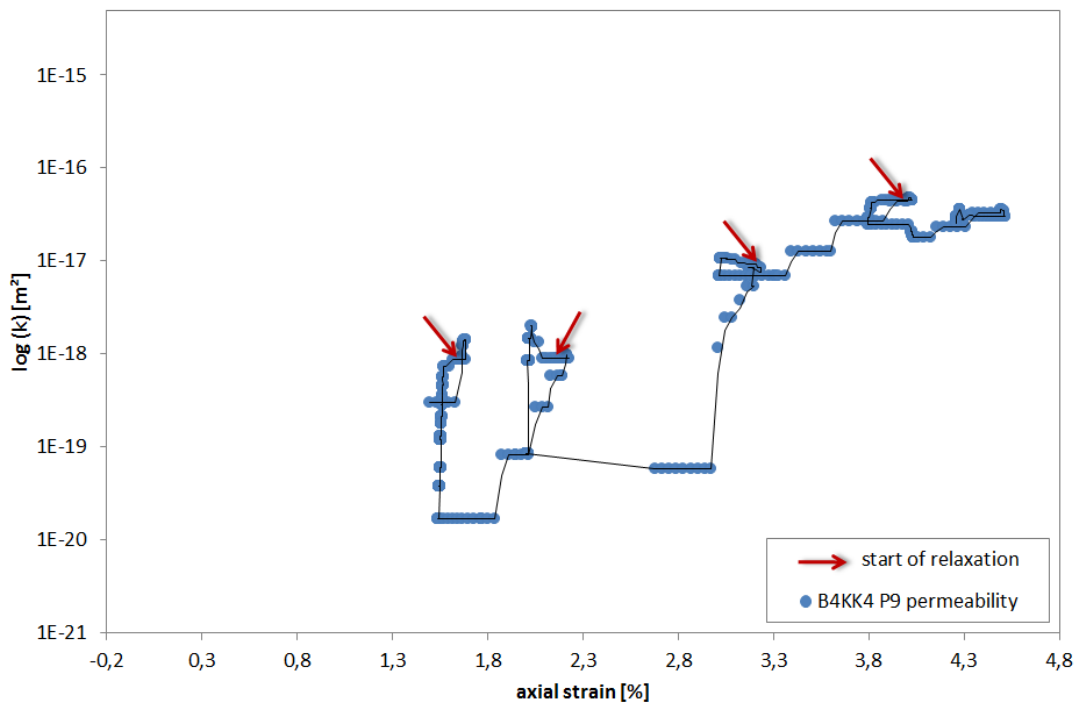


Fig. 3.12 Permeability development of salt concrete sample B4KK4 P9 deformed by deviatoric loading at multiple confining stresses. Deformation path is delineated by the black line

3.2.3 Measurement results and interpretation

The porosity-permeability relationships examined in the present study are the same as examined in /WIE 10/. As no relationship has been developed specifically for salt concrete, basic porosity-permeability relationships and models considering fracture development were used here. During laboratory measurement, the development of porosity

could not be tracked, so volumetric strain is used as a proxy for porosity here. This is applicable in so far, as volumetric extension represents the increase in porosity and there is no other extending mechanism present. The porosity-permeability relations examined here are:

1. A Kozeny-type function:

$$k = k_0 \left(\frac{V}{V_0} \right)^n$$

$$k_0 = 5e^{-19}V_0 = 0.07697 \text{ m}^2n = 8$$

2. A micro fracture model after Olivella /OLI 08/ with spacing of fractures and variable aperture as a function of volumetric strain:

$$k = k_{matrix} + \frac{b^3}{12s} b = b_0 + \Delta b \Delta b = s(\varepsilon - \varepsilon_0)$$

$$k_{matrix} = 1e^{-20}; \quad b_0 = 3e^{-13} - 1e^{-10}; s = 5e^{-8} - 1e^{-7};$$

ε_0 = volumetric strain at onset of gas flow

The threshold parameter ε_0 is associated with failure of the sample, which in this case is defined as the point, when microcracks connect to enable gas flow.

3. A percolation model for rock salt in the EDZ, modified from Alkan /ALK 09/:

$$k = k_f \cdot A \cdot \left[\left(1 - e^{\left(\frac{V}{V_p} \right)} \right) - 0.63 \right]^2 V_p = V_0 \cdot (1 + \varepsilon_p)$$

$$k_f = \text{maximum measured permeability} \quad A = 35V_0 = 0.07697 \text{ m}^2$$

The parameter V_p (percolation threshold) defines at which volumetric increase, flow starts. The k_f value is inserted for each sample individually.

Permeabilities for these relationships were calculated from volumetric deformations measured in triaxial compression tests and compared with permeabilities obtained from those tests. Fig. 3.13 shows the results for different permeability-relationships, compared with laboratory data. With the exception of B4KK3 P2, samples follow a trend that, with increasing confining stress, the onset of gas flux is at higher volumetric strains while initial permeability is lower. This coincides well with the assumption, that

increasing confining stress inhibits evolution of micro cracks and delays gas flow. Only permeability measurements of four samples were considered, as the others were either intruded by oil during measurement and therefore did not allow gas flux, or data showed inconsistencies (cf. Fig. 3.14). As already delineated in /WIE 10/, the Kozeny-type function yields poor results and is not able to describe the development of permeability. This is confirmed by the results of the Kozeny-Carman equation for sample B4KK4 P13.

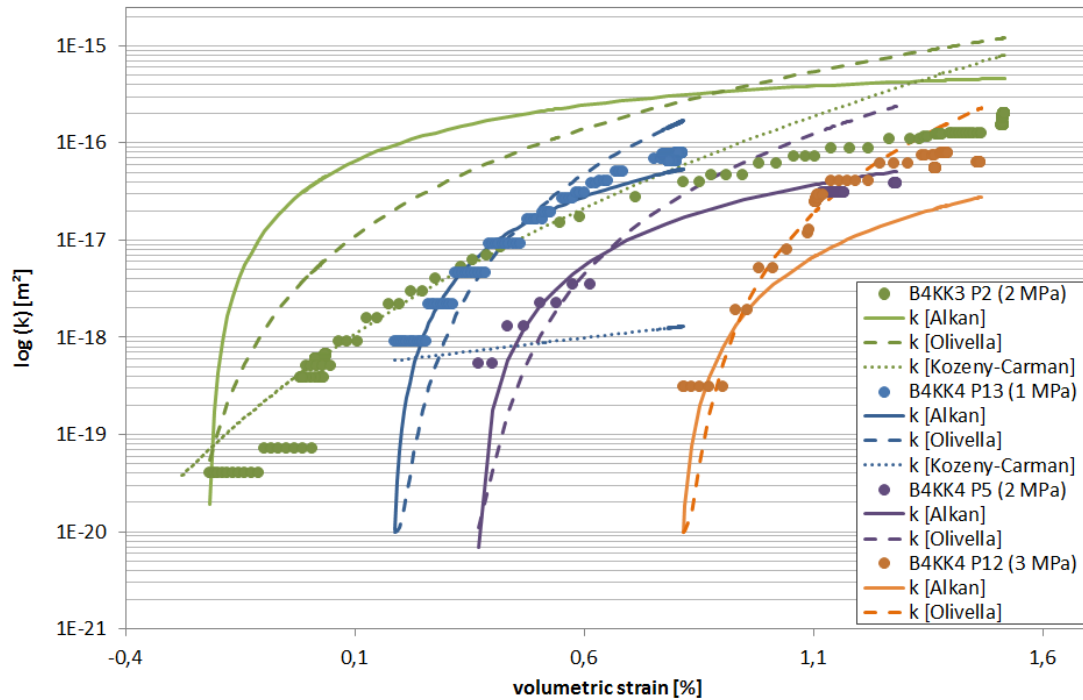


Fig. 3.13 Permeability as a function of volumetric strain. Laboratory data for confining pressures of 1-3 MPa are compared with calculated permeabilities

At first sight, both the percolation model after /ALK 09/ and the micro fracture model after /OLI 08/ appear as a good approximation. However, it was not possible to describe the porosity-permeability relation with one parameter set, using Olivella's model. Instead, parameters for obtaining the curves in Fig. 3.13 have to be varied several orders of magnitude. On the other hand, describing the porosity-permeability relation with the Alkan model is possible without changing the parameters. For samples B4KK4 P13 and B4KK4 P12, Alkan's percolation model underestimates permeability at high volumetric strains. This is due to Alkan's model strongly depending on the maximum measured permeability. If deformation of those samples continued, the maximum measured permeability would be higher and hence, permeability at high volumetric strains would not be underestimated.

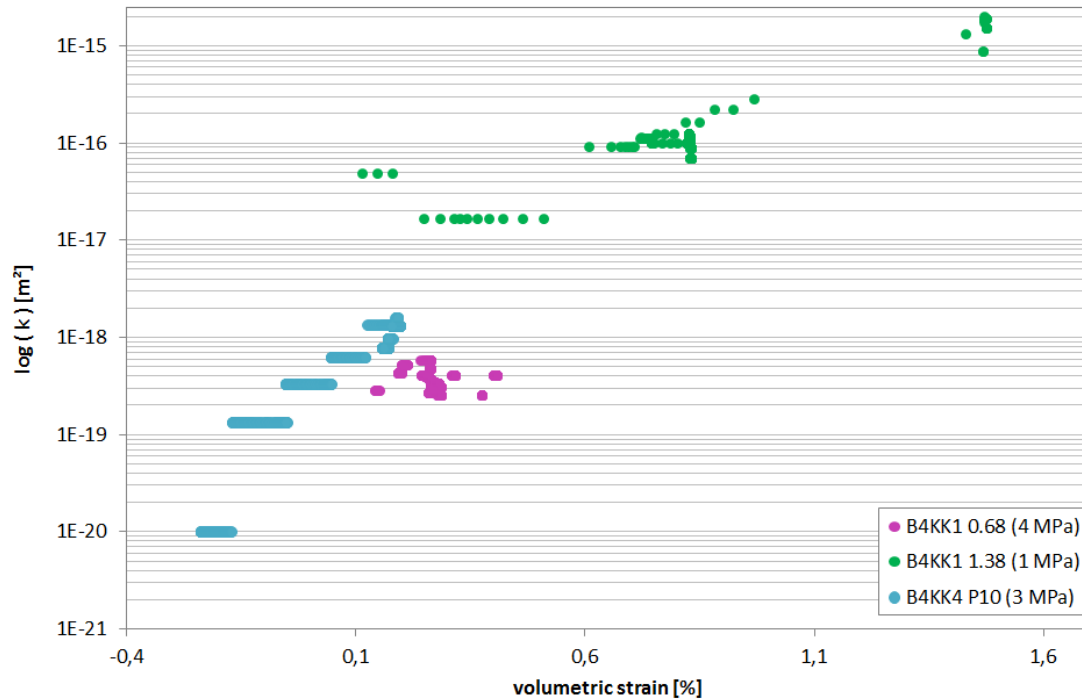


Fig. 3.14 Samples not considered for porosity-permeability relationship. Sample B4KK1 0.68 shows no development at all; ultimate permeability of sample B4KK4 P10 is too low to allow a prediction by the equations; initial permeability of sample B4KK1 1.38 is probably too high and is therefore not able to be modelled by the relations

Fig. 3.15 shows the development of permeability for the multi-stage triaxial test. Parameters for the percolation model after Alkan are unchanged from the previous TC-tests, whereas parameters for fitting the Olivella model had to be significantly changed ($b_0 = 2 \cdot 10^{-6}$, $a = 3 \cdot 10^{-4}$). Inhomogeneity in permeability increase of laboratory data is due to the un- and reloading between each increase in confining pressure. Olivella's model clearly overestimates permeability at high volumetric strain. The percolation model after Alkan slightly overestimates permeability at low volumetric strain but nicely fits with laboratory data at higher volumetric strain. The fact, that Alkan's model was able to predict the evolution of permeability of the multi stage triaxial test from the parameter set obtained on triaxial tests, creates confidence in its applicability. Although Olivella's model is more conservative, the parameter combination has to be calibrated for each test individually, which makes prediction of permeability impossible. Therefore, Alkan's model, which also more accurately describes the relationship between permeability and volumetric extension, is chosen here for further investigation of salt concrete.

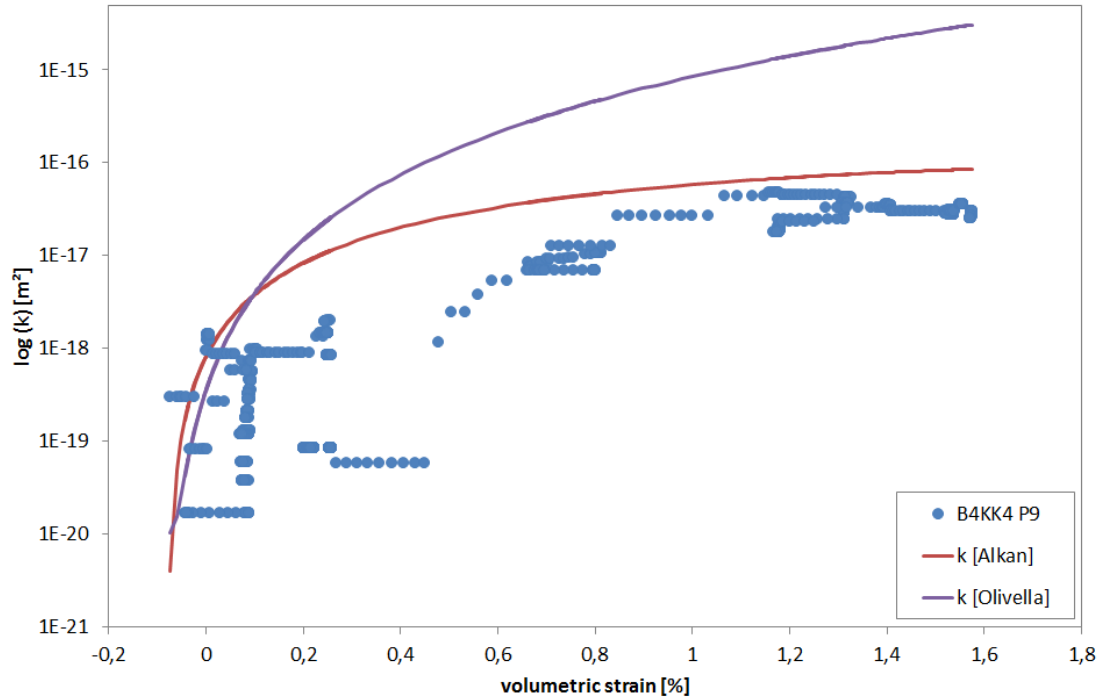


Fig. 3.15 Development of permeability for the multi-stage triaxial test

It has been shown, that Alkan's model fits very well with laboratory data. However the major drawbacks are: (1) that the maximum measured permeability (ultimate connectivity) has to be inserted individually for each sample and (2) that the onset of gas flow has to be defined for each sample individually. In the present study, it was not possible to define a percolation threshold or ultimate conductivity for a specific state of confining stress due to the limited amount of measurements. As a consequence of the heterogeneity of salt concrete, it remains questionable, if a specific percolation threshold can be defined at all.

3.3 Long-term deformation behaviour – uniaxial-testing method

3.3.1 Experimental layout

Uniaxial creep tests were performed in five rigs in air-controlled room. One rig allows five samples being simultaneously tested at the same load up to 500 kN at ambient temperature. Fig. 3.16 shows the rig for uniaxial creep tests on five samples. Axial load was applied equally to the five samples by means of an oil balance with accuracy higher than $\pm 0.5\%$. Axial deformation of each sample was originally measured by displacement transducers (LVDT) with an accuracy of ± 0.1 mm. The strain measurement was then improved by several strain gauges of higher resolution of $1 \cdot 10^{-6}$. They were directly glued on the samples for both axial and radial strain measurements.

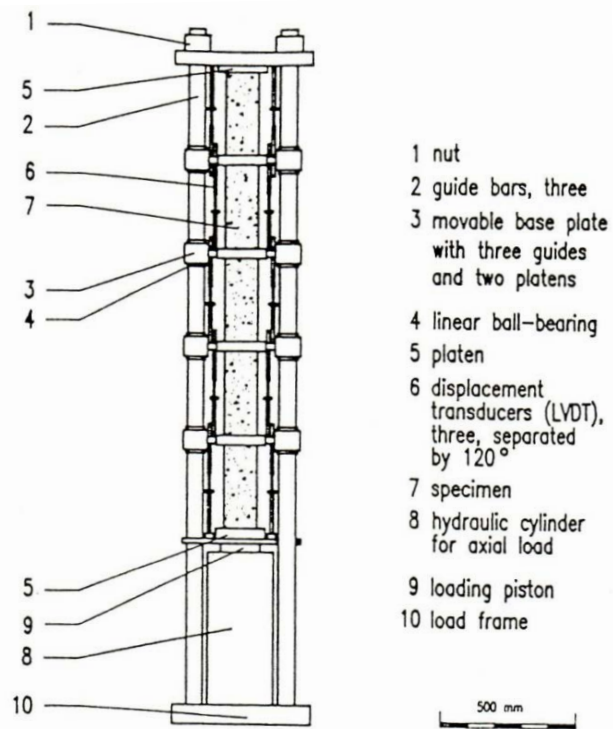


Fig. 3.16 Rig for uniaxial creep tests on five samples one upon another

3.3.2 Testing procedure

The aim of these tests is to determine the deformation of the samples in terms of strains and strain rates in order to describe the time-dependent uniaxial creep behaviour of salt concrete at different stress states.

The uniaxial creep tests (UC-Test) were carried out on five specimens in a uniaxial apparatus at the GRS laboratory. The initial dimension of the specimens was 80 mm in diameter and 160 mm in length. The specimens were tested in one apparatus at the same time, the specimens were arranged above each other. In this way, all specimens were submitted to nearly identical stress conditions, see Fig. 3.18.

The axial and radial deformations were measured for each specimen. The measurements of the axial deformations were carried out using “Linear Differential Variable Transformers” (LDVT) and strain gauges (DMS), the radial deformations by using strain gauges only.

In the following analysis, only the results for axial deformation measured by LDVT are considered. The reason for this approach is that the LDVT measure the change of the whole length of the specimen while the strain gauges measure only a fraction. Thus, the measurement with the LDVT is more representative for the overall sample behaviour. The denotations SC(1048) up to SC(1052) serve as identification for the individual specimens of the uniaxial tests.

The UCc-Tests were executed at three different stress states. First, the axial stress was set to 5 MPa. The following steps were performed at 10 MPa and 20 MPa, respectively. During the tests the temperature was around 25 °C. The axial stress causes a reduction of the length and an increase in diameter of the specimens.

All tests lasted over nearly 300 days with step duration of 76 to 106 days. Uniaxial strain-time curves measured on 5 samples are illustrated in Fig. 3.17, whereas the stress and temperature boundary conditions are shown in Fig. 3.18.

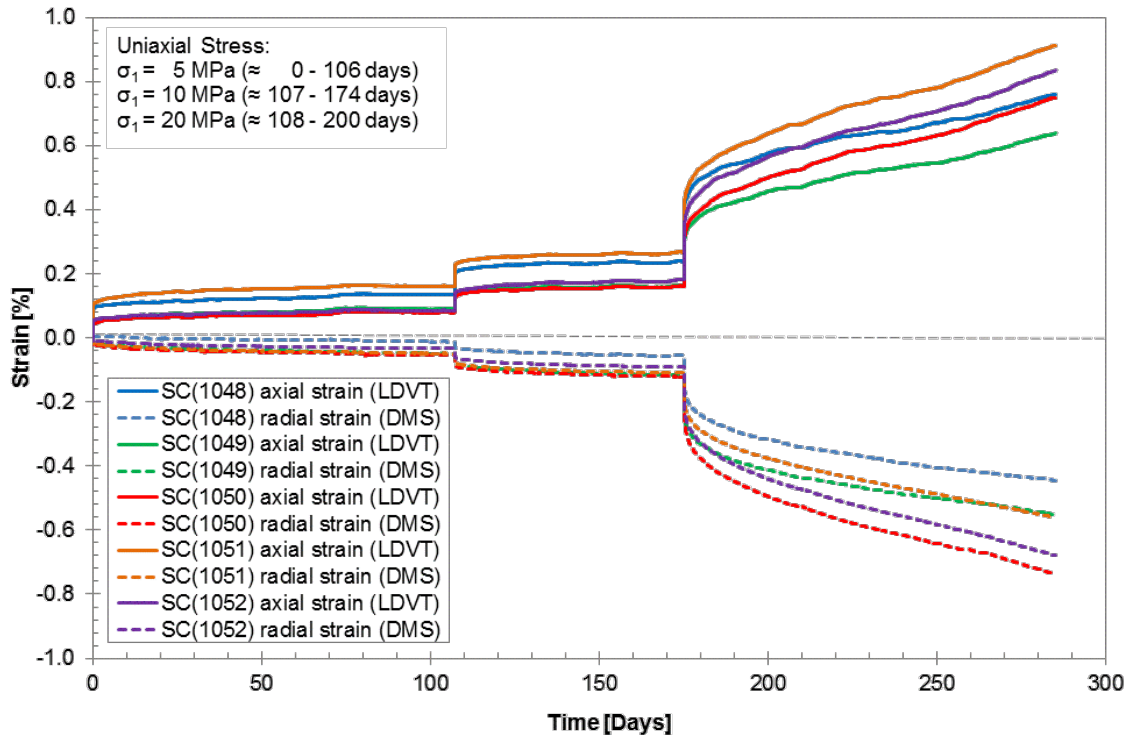


Fig. 3.17 Long-term uniaxial creep behaviour of five salt concrete samples under multi-step loads – axial and radial strains

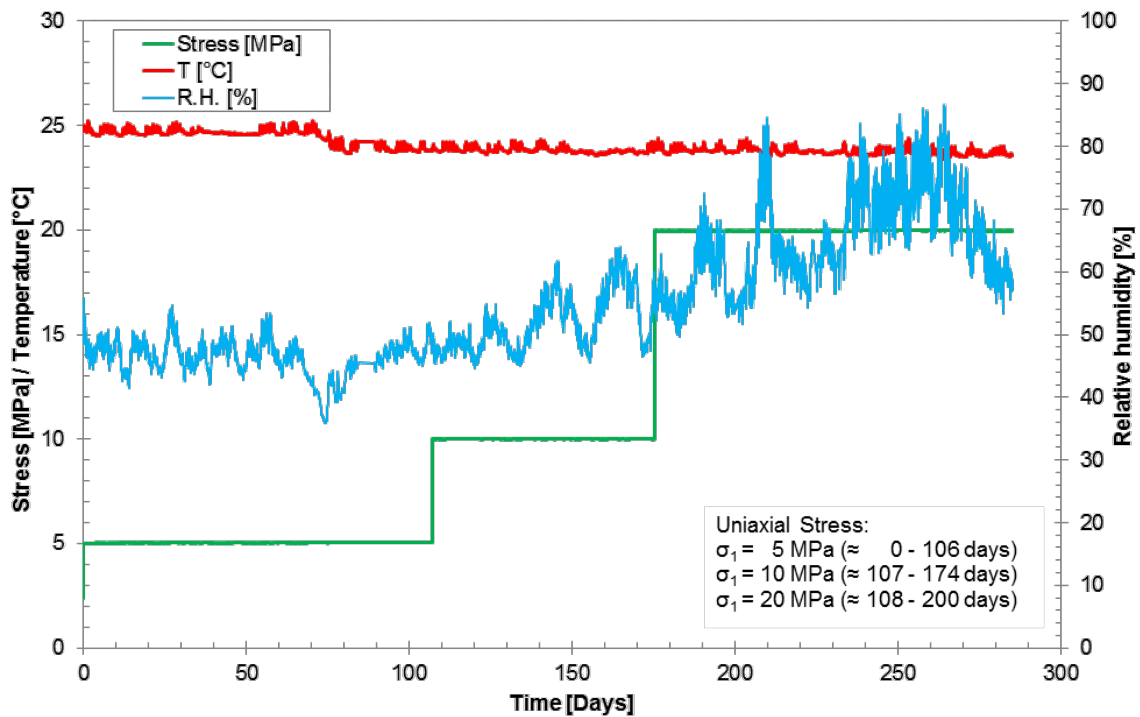


Fig. 3.18 Long-term uniaxial creep behaviour of five salt concrete samples under multi-step loads – stress, temperature and relative humidity evolution

3.3.3 Measurement results and interpretation

The following figures Fig. 3.19 up to Fig. 3.23 show the axial strains and the strain rates as a function of time for the individual specimen. Strain rates are averaged over seven days.

The figures show that at the first two stress levels strains scarcely increase while strain rates quickly decrease. That means that there is no stationary creep. Strains increase at the third stress level, and strain rates seem to stabilize in the range of $1 \cdot 10^{-10} \text{ s}^{-1}$, which could imply a steady state creep at this stress level.

The results of the uniaxial creep test show that material behaviour is different at lower stress levels of 5 MPa and 10 MPa and at a stress level of 20 MPa. While strains are small at lower stresses, a distinct creep deformation occurs at a stress level of 20 MPa.

The reason for the different deformation behaviour at various stress levels might be that the cement structure of the salt concrete bears first uniaxial stresses up to 10 MPa. Cement is expected to have an elastic material behaviour without viscoplastic deformations after the water curing process has finished. Although, there was no significant time dependent deformation at lower stresses, creep rates could be derived.

When the stress level was increased up to 20 MPa, the cement structure of the salt concrete was damaged. Consequently, the salt grit structures of the salt concrete was subjected to the load and because of the viscoplastic material behaviour of salt grit the specimens exhibited explicit creep behaviour, see Fig. 3.24.

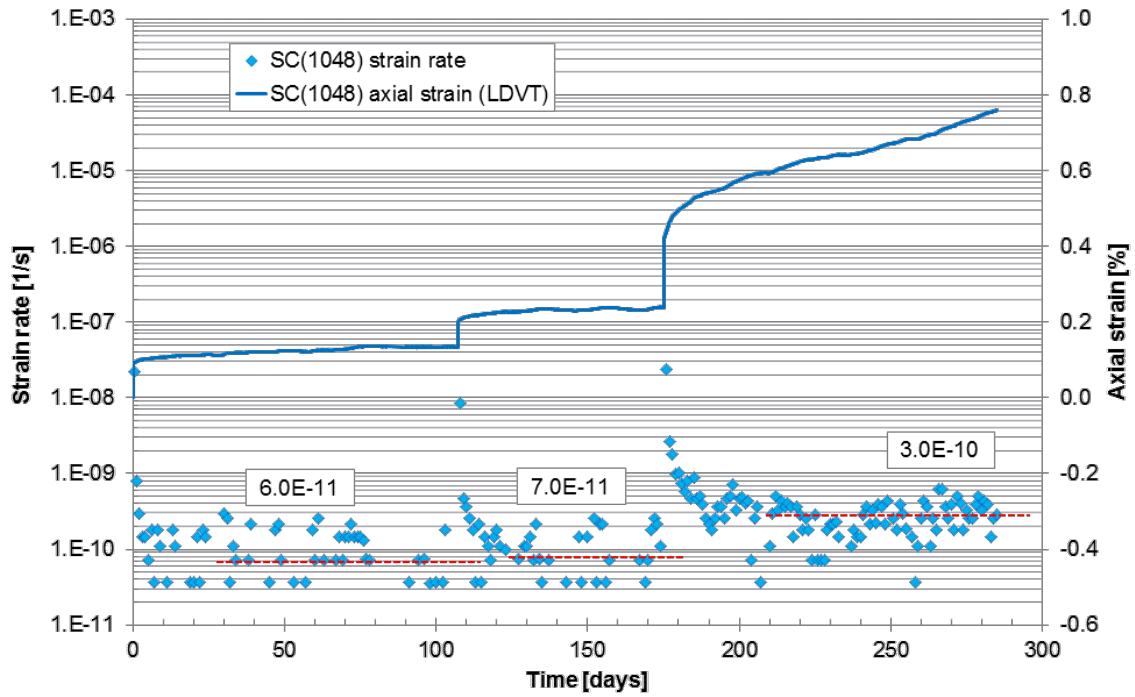


Fig. 3.19 Long-term uniaxial creep behaviour of salt concrete sample no.1048 under multi-step loads – axial strain and derived creep rates

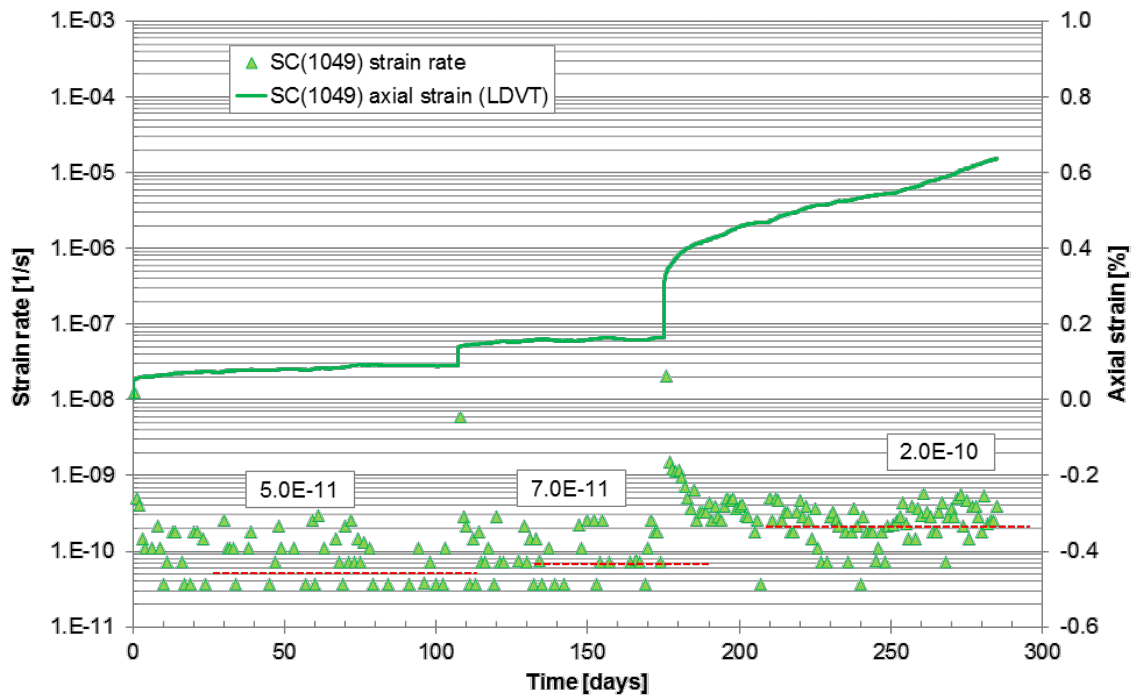


Fig. 3.20 Long-term uniaxial creep behaviour of salt concrete sample no.1049 under multi-step loads – axial strain and derived creep rates

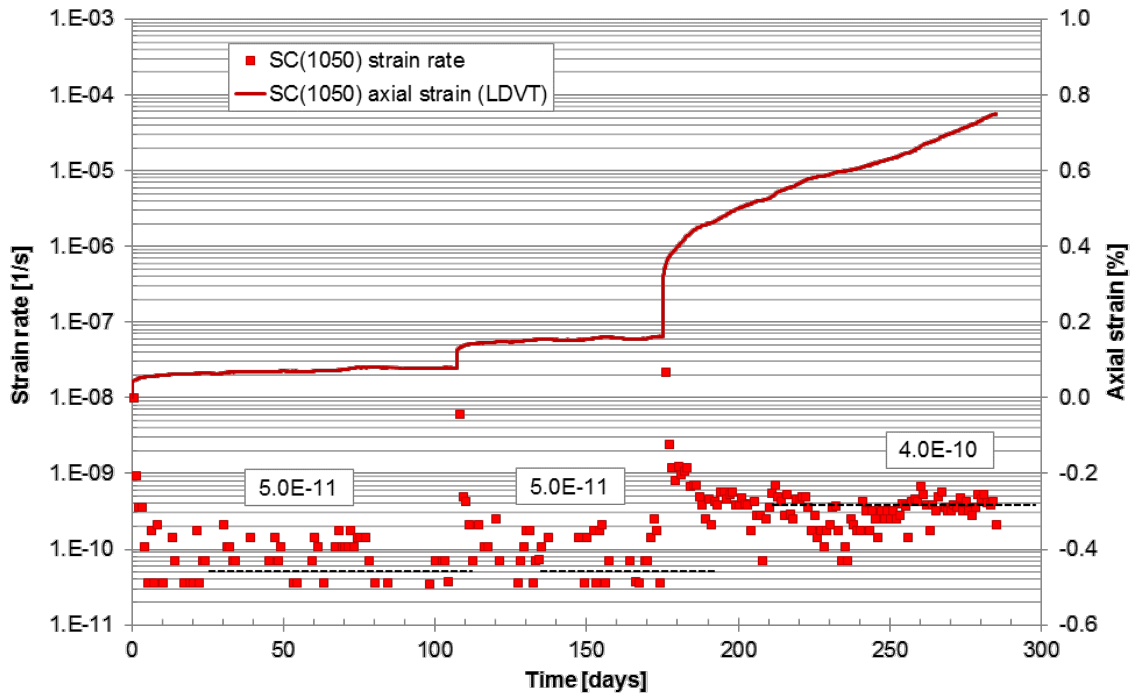


Fig. 3.21 Long-term uniaxial creep behaviour of salt concrete sample no.1050 under multi-step loads – axial strain and derived creep rates

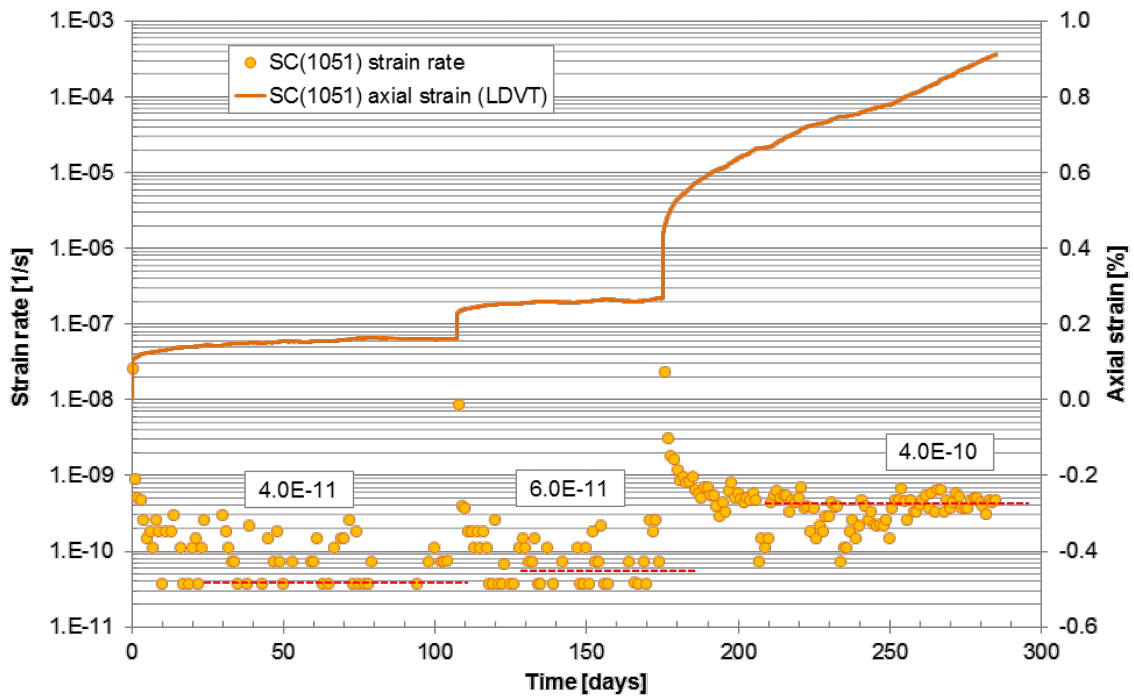


Fig. 3.22 Long-term uniaxial creep behaviour of salt concrete sample no.1051 under multi-step loads – axial strain and derived creep rates

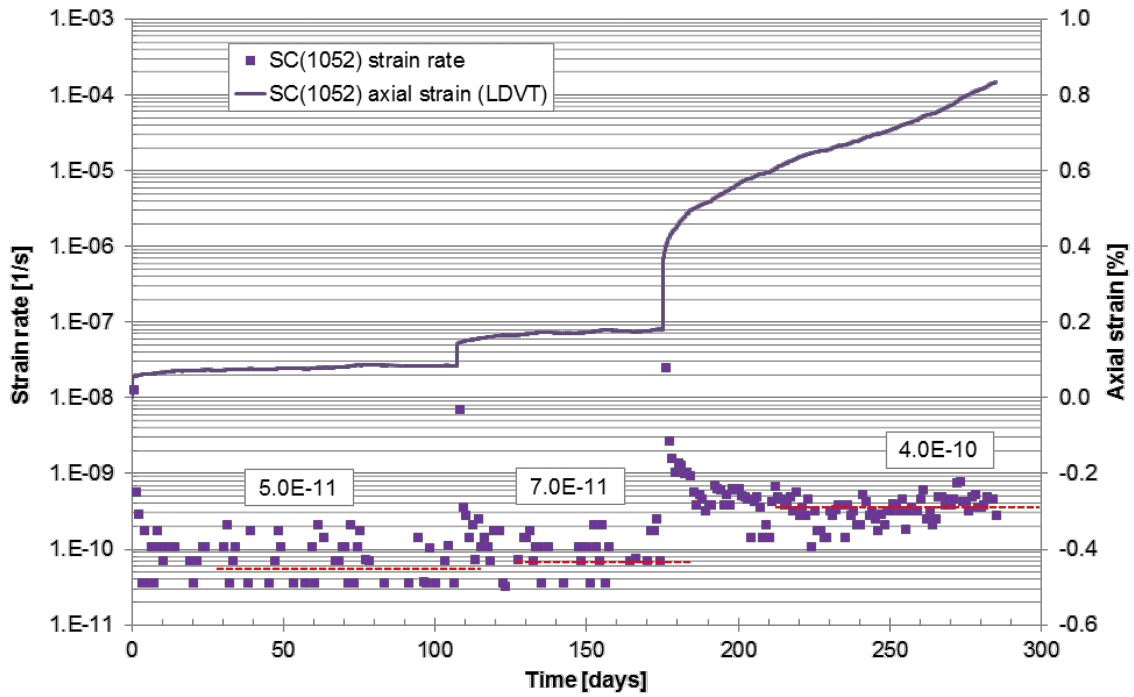


Fig. 3.23 Long-term uniaxial creep behaviour of salt concrete sample no.1052 under multi-step loads – axial strain and derived creep rates

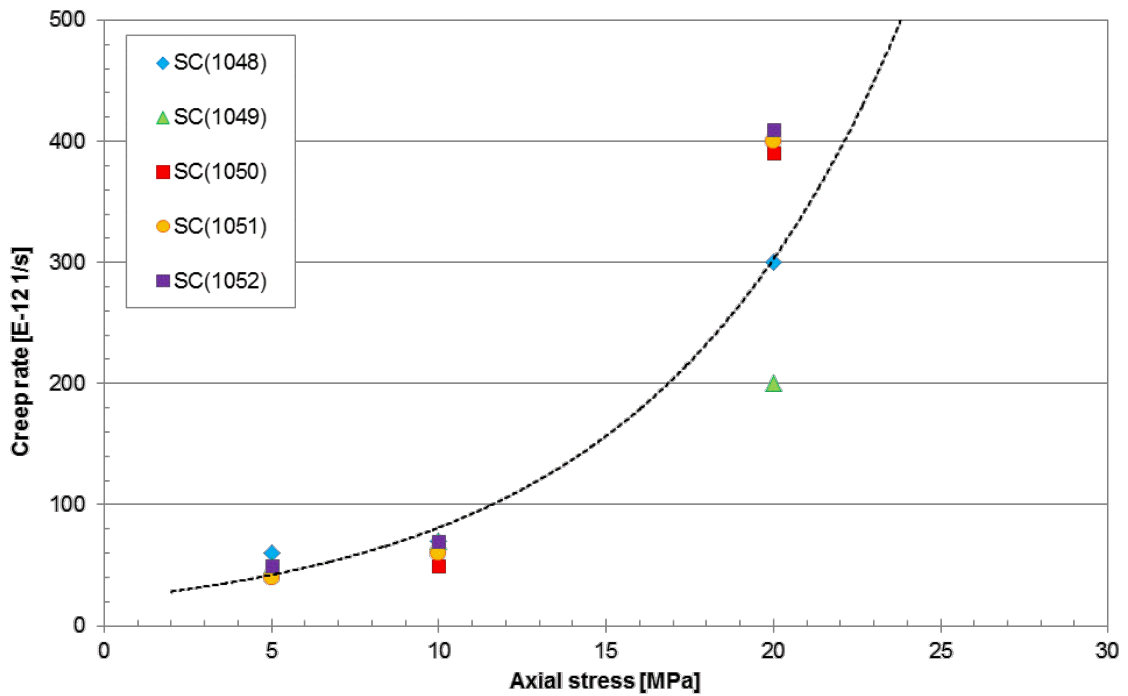


Fig. 3.24 Steady-state creep rates obtained on five salt concrete samples as a function of applied uniaxial loads

3.4 Long-term deformation behaviour – triaxial-testing method

3.4.1 Experimental layout

Triaxial creep tests were carried out on four salt concrete samples in a triaxial apparatus with measurement of deformation and gas permeability under various stress conditions. The average porosity of the samples is about $\phi = 5.8\%$ with a grain density of $2.17 - 2.2 \text{ g/cm}^3$. The average water content is at a level of $w = 2$ weight-%.

The samples were isolated in a jacket and porous discs at top and bottom and placed inside a steel cylinder. The rig for uniaxial creep tests as shown in Fig. 3.16 was used to provide axial stress on all samples, while each cylinder has its own oil reservoir for individual minimum pressure. Fig. 3.25 shows one steel cylinder inside the rig.



Fig. 3.25 Steel cylinder for individual oil pressure built-up on a salt concrete sample

3.4.2 Testing procedure

The aim of these tests is to determine the deformation of the samples in terms of strains and strain rates in order to describe the time-dependent triaxial creep behaviour of salt concrete at different stress states.

The triaxial compressive creep tests (TCc-Test) were carried out on four samples under stress control in a triaxial apparatus at the GRS laboratory. The initial dimension of the samples was 50 mm in diameter and 100 mm in length and had been obtained by core-drilling from a real plug installed in a salt mine. Prior to testing, the samples were already damaged and had exceeded the dilatancy boundary, see chapter 3.1. The samples were tested in one apparatus (chapter 3.3) at the same time and were arranged above each other. In this way, all samples were submitted to nearly identical stress conditions, see Fig. 3.26. The axial deformations were measured for each sample, using "Linear Differential Variable Transformers" (LDVT). During pre-compaction, the samples were subjected for about 14 days to an isotropic stress level of 10 MPa.

Second step of the test was to deform the samples under deviatoric stress. The TCc-Tests were executed at three different stress states. From the isostatic condition at 10 MPa during pre-compaction, radial stress was reduced to 2 MPa. In the following steps, axial stresses were increased to 18 MPa and 38 MPa respectively. During the tests the temperature was around 24 °C. The axial stress causes a reduction of the length and an increase in diameter of the samples.

All tests lasted over nearly 140 days with a step duration of 13 to 56 days. Triaxial strain-time curves measured on four samples are illustrated in Fig. 3.27, whereas the stress and temperature boundary conditions are shown in Fig. 3.26. During the tests gas was injected in axial direction for permeability measurement.

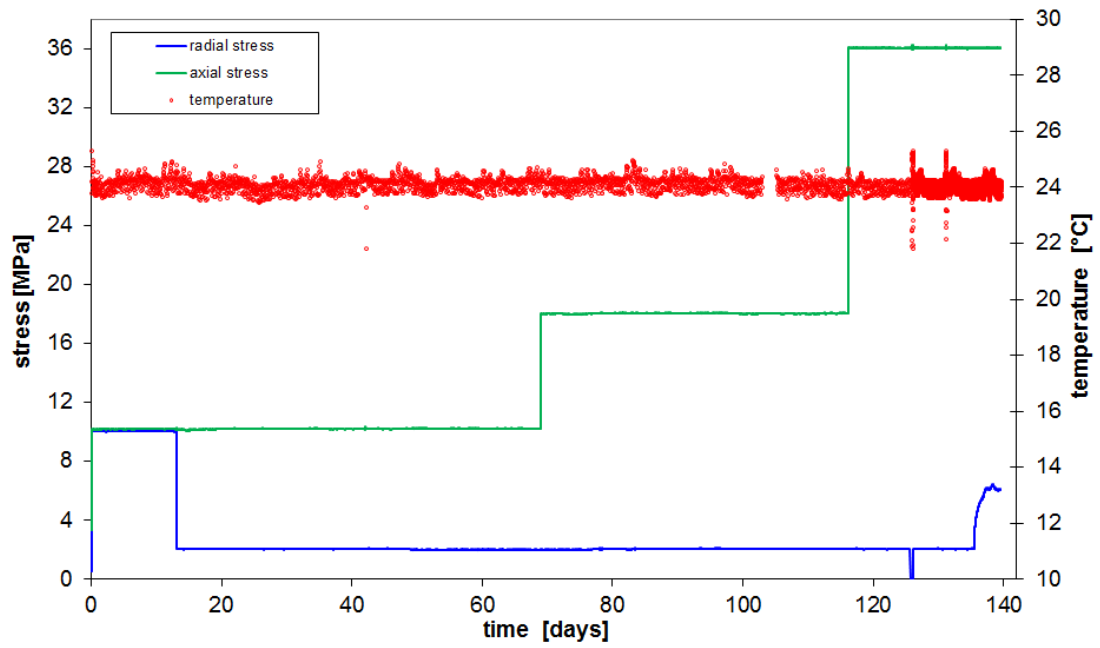


Fig. 3.26 Long-term triaxial creep behaviour of four salt concrete samples under multi-step loads – stress and temperature

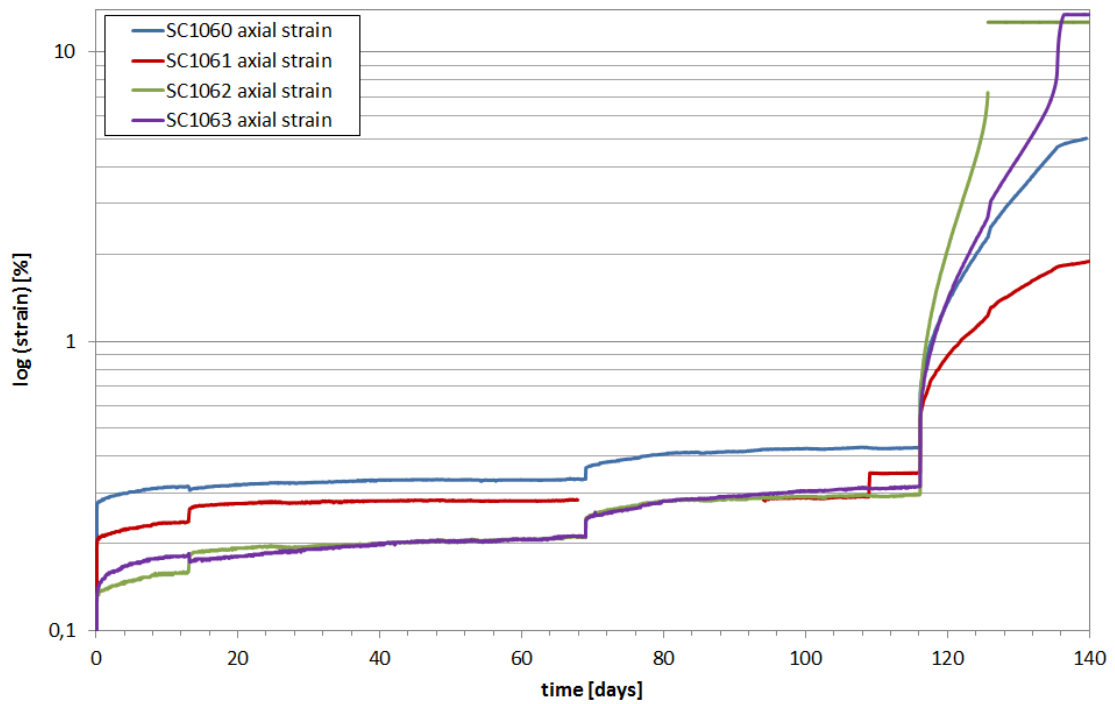


Fig. 3.27 Long-term triaxial creep behavior of four salt concrete samples under multi-step loads – axial strains

3.4.3 Measurement results and interpretation

The following figures Fig. 3.28 up to Fig. 3.31 show the axial strains and the strain rates as a function of time for the individual specimen. Strain rates are averaged over one day.

For sample 1061, there has been a measuring error from 68 to 93 days and therefore only deformations before that error are considered as valid.

The figures show that at the first two stress levels strains slowly increase while strain rates quickly decrease, which gives evidence for transient creep. Strain rates seem to stabilize around $5 \cdot 10^{-11}$ in phase 1 and around $1 \cdot 10^{-10}$ in phase 2, which could imply stationary creep in these phases. However, average strain rates for stationary creep are lower than inferred strain rates for a time span of one day. This is due to the resolution limit of measurements, which results in minimum strain rates of $1 \cdot 10^{-10}$. Therefore, a further decrease in strain rates would not have been able to be detected.

The results of the uniaxial creep test show that material behaviour is different at lower deviatoric stresses of 8 MPa (phase 1) and 18 MPa (phase 2) than at a deviatoric stress of 36 MPa (phase 3). While strains are small at low σ_{dev} , a distinct creep deformation occurs in the third stress level. Furthermore, strain acceleration can be observed in samples 1060, 1062 and 1063 at σ_{dev} of 36 MPa, hence tertiary creep occurs. Creep rupture could be identified for sample 1062 at axial strains of 7.2 % (Fig. 3.30). Steady-state creep does not occur in phase 3.

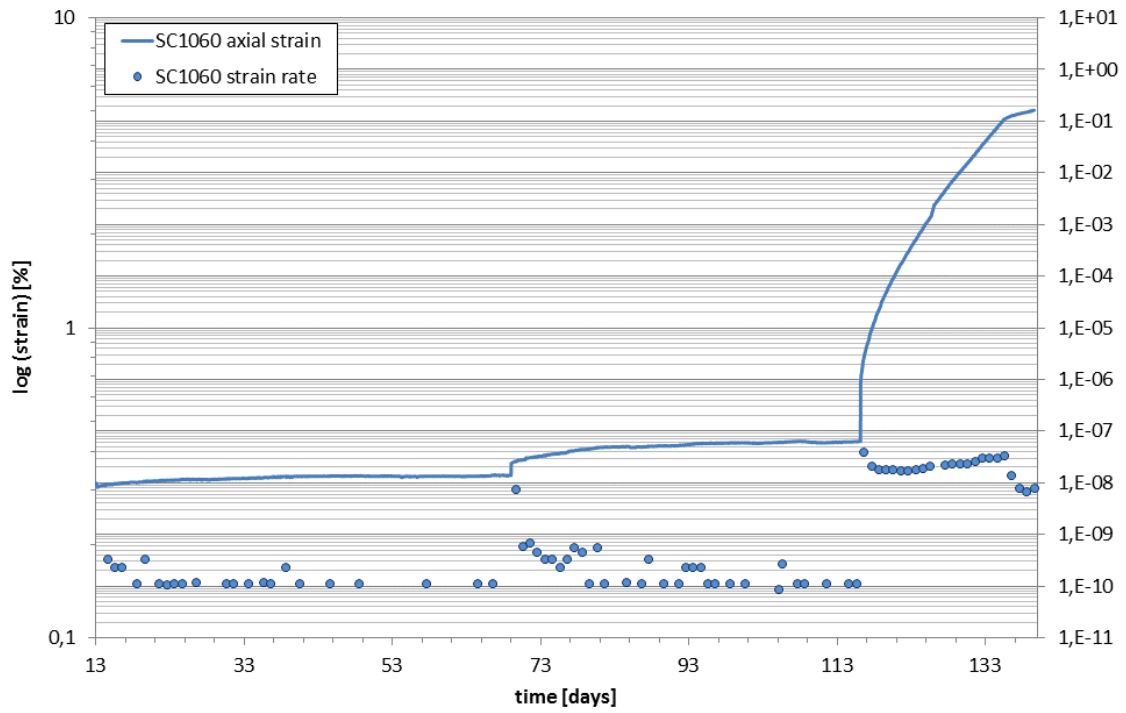


Fig. 3.28 Long-term triaxial creep behaviour of salt concrete sample no.1060 under multi-step loads – axial strain and derived creep rates

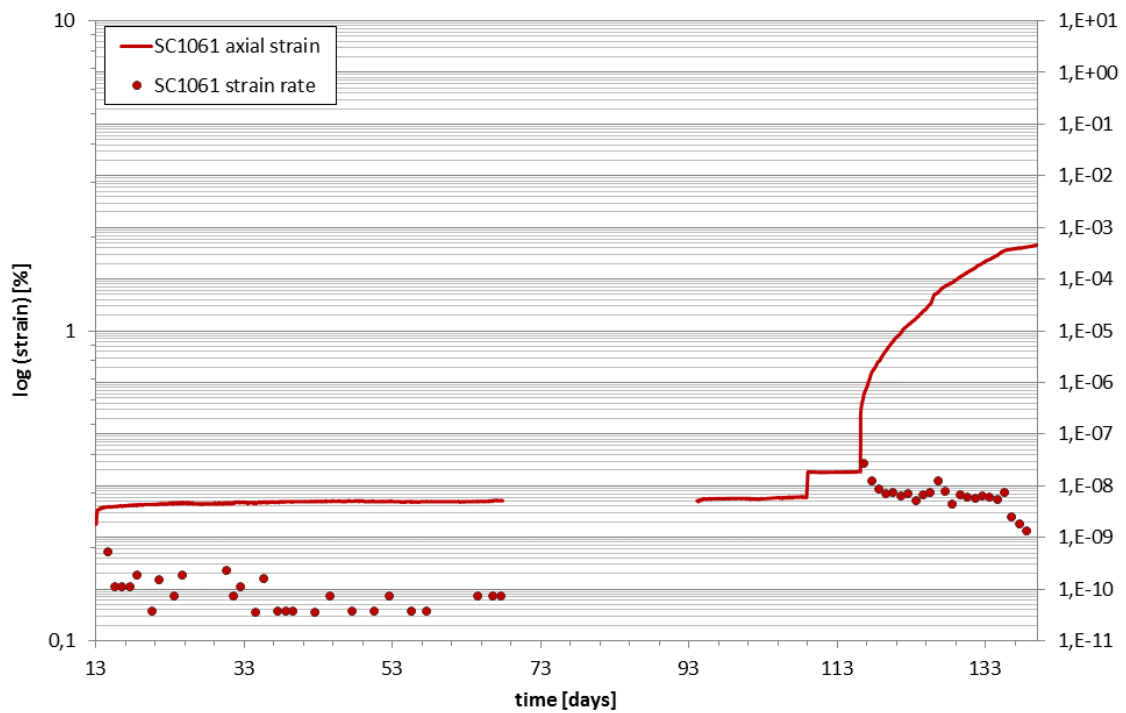


Fig. 3.29 Long-term triaxial creep behaviour of salt concrete sample no.1061 under multi-step loads – axial strain and derived creep rates

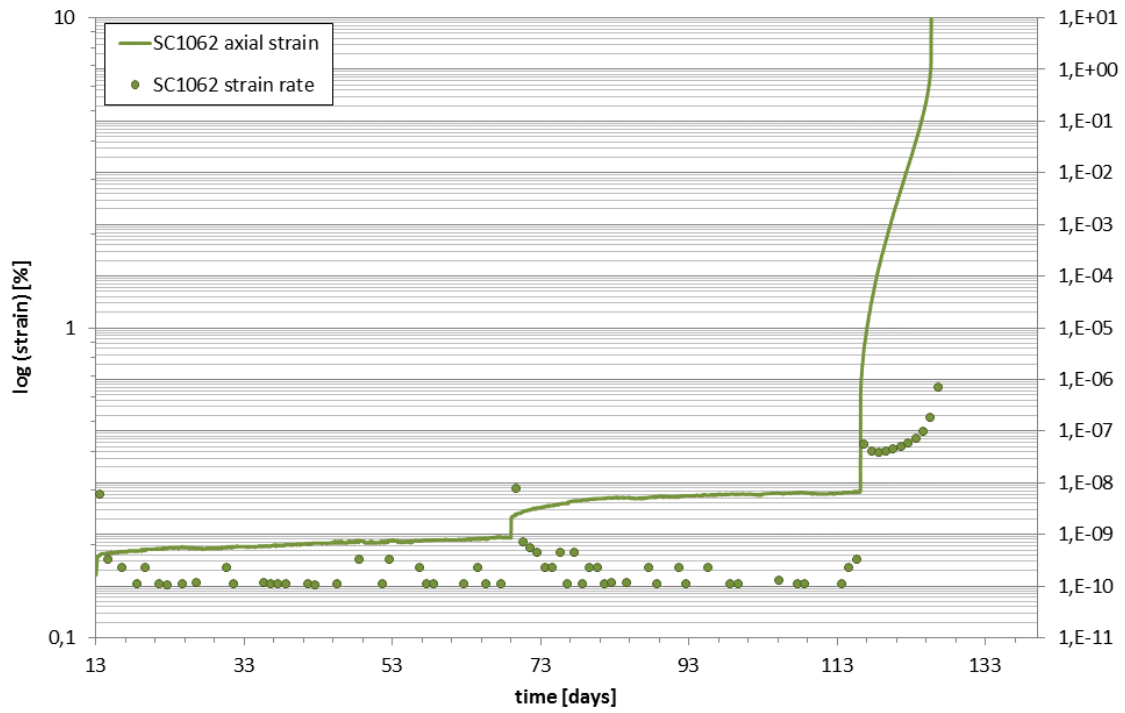


Fig. 3.30 Long-term triaxial creep behaviour of salt concrete sample no.1062 under multi-step loads – axial strain and derived creep rates

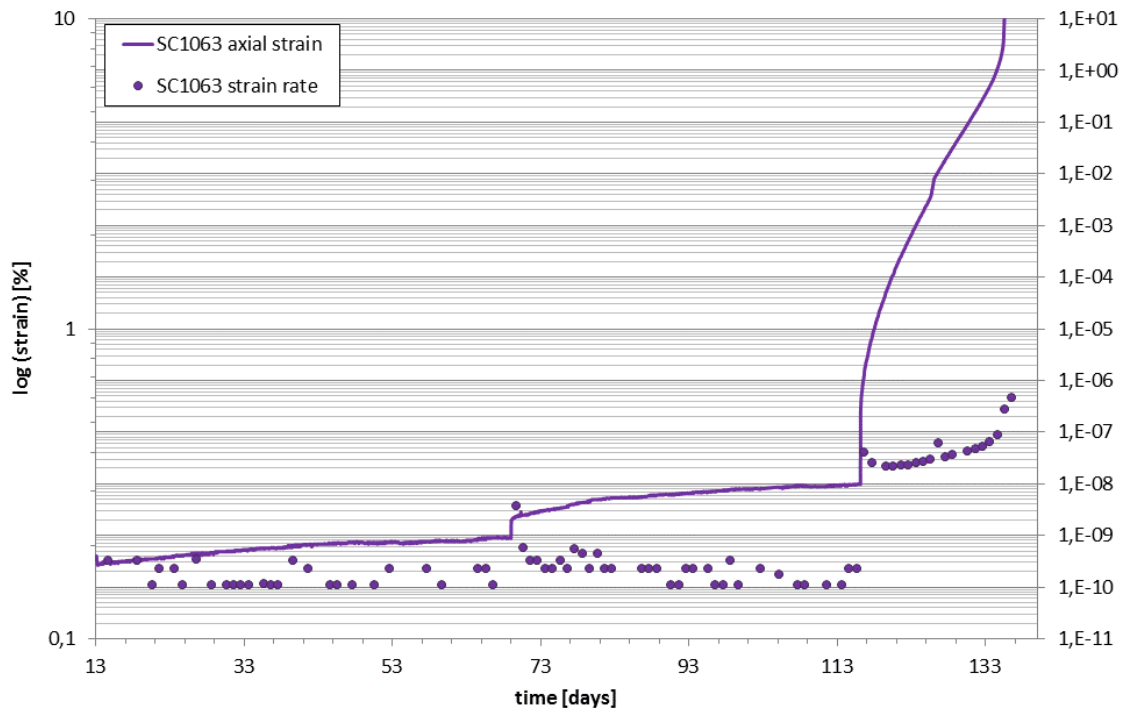


Fig. 3.31 Long-term triaxial creep behaviour of salt concrete sample no.1063 under multi-step loads – axial strain and derived creep rates

3.5 Long-term deformation behaviour – temperature effects

3.5.1 Experimental layout

Triaxial creep tests were carried out on salt concrete samples in a triaxial apparatus with measurement of deformation and gas permeability at ambient and elevated temperatures. Fig. 3.32 shows the rig for triaxial creep tests with temperature control. Axial load was applied by means of an oil balance with accuracy higher than $\pm 0.5\%$. Axial deformation was originally measured by displacement transducers (LVDT) with an accuracy of ± 0.1 mm. The radial strain measurement was then measured by a chain of high resolution.

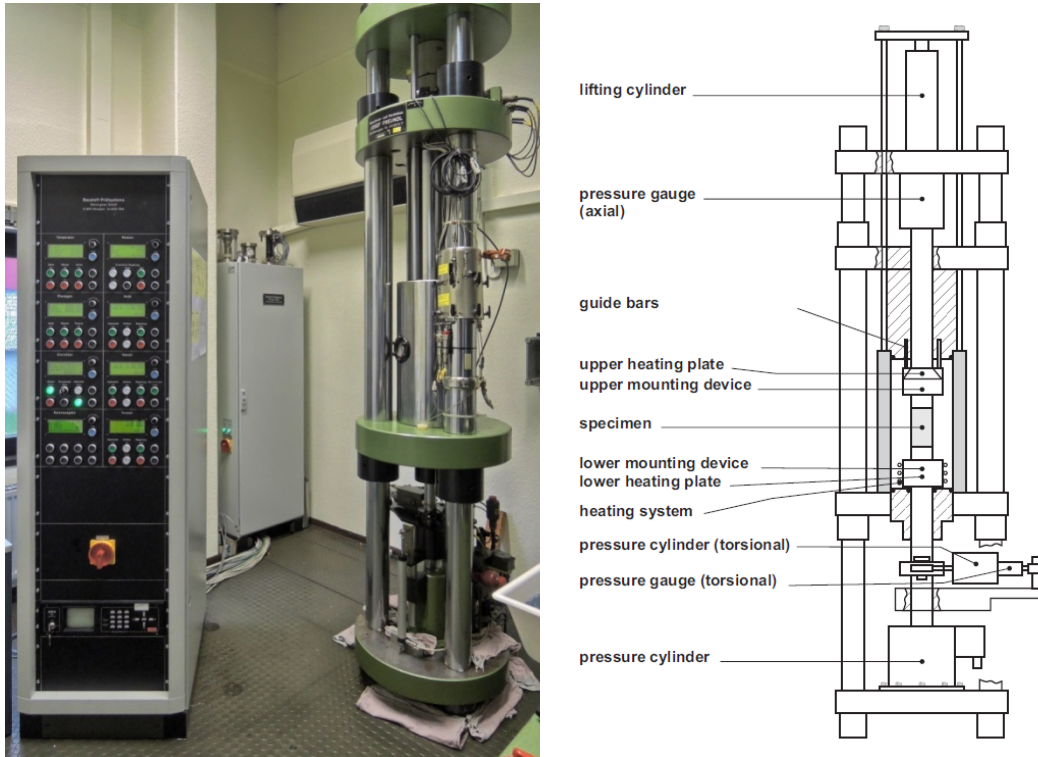


Fig. 3.32 Rig for triaxial creep tests with temperature control

3.5.2 Testing procedure

The aim of these tests is to determine the deformation of the samples in terms of strains and strain rates in order to describe the time-dependent triaxial creep behaviour of salt concrete at elevated temperatures.

The triaxial creep tests were carried out on three samples (1 intact sample and 2 pre-damaged ones) under stress control in a triaxial apparatus at the GRS laboratory. The initial dimension of the samples was 50 mm in diameter and 100 mm in length and had been obtained by core-drilling from a real plug installed in a salt mine. Prior to testing, two samples were already damaged and had exceeded the dilatancy boundary, see chapter 3.1.

During a first phase at ambient temperature of 30 °C, the intact sample was subjected to a deviatoric stress level of 20 MPa for about 13 days, see Fig. 3.33. Second step of the test was to determine the deformation of the sample under deviatoric stress and elevated temperatures of 60 °C. The elevated temperature causes an additional reduction of the length of the sample, though the stress boundary conditions were kept constant.

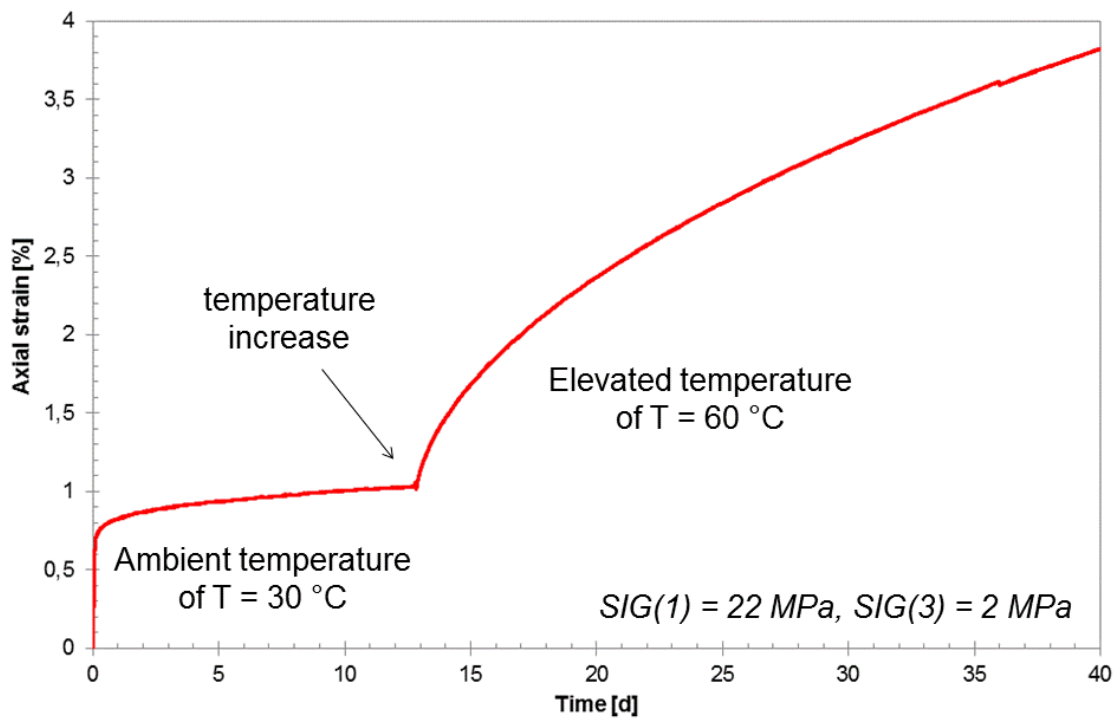


Fig. 3.33 Deformation behaviour of the intact concrete sample at ambient and elevated temperatures

The triaxial tests were also carried out on pre-damaged samples to show the influence of elevated temperatures for salt concrete with damaged cement structure, where the viscoplastic material behaviour of the salt grit structure is of major importance for the overall deformation behaviour of the sample. Therefore, two tests were performed with different temperatures of 40 °C and 60 °C.

Fig. 3.34 shows the axial strains as a function of time for all specimens. The curves are arranged in a way that time “0” corresponds to the point of temperature increase.

Unexpectedly, elevated temperatures lead to failure of the pre-damaged samples.

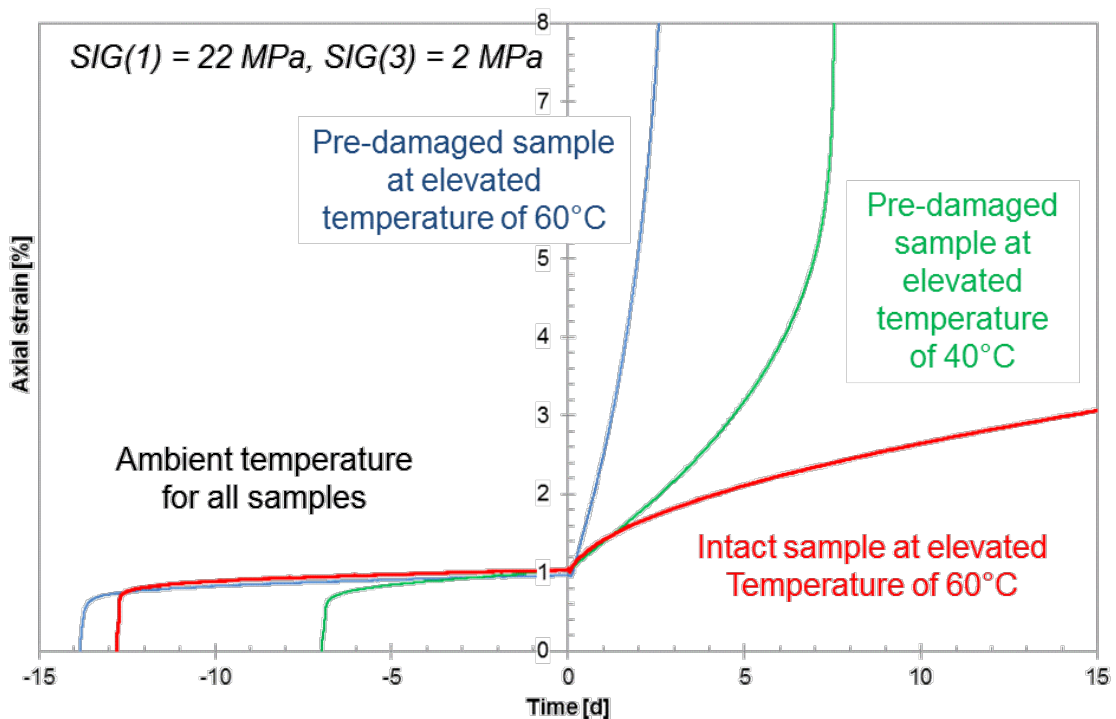


Fig. 3.34 Deformation behaviour of the tested concrete samples at ambient and elevated temperatures - standardized curve illustration

3.5.3 Measurement results and interpretation

The following figures show the derived axial strain rates as a function of time for the individual specimens, Fig. 3.35 for the intact sample only and Fig. 3.36 for all specimens. Strain rates are averaged over 6 hours.

Fig. 3.35 show that at ambient temperature strain rates quickly decrease below a level of $2 \cdot 10^{-9} \text{ s}^{-1}$. The relatively short testing time interval of 13 days precludes a clear statement of stationary creep behaviour.

At increasing temperature, the creep rates increases by 2 orders of magnitude. Then at the elevated temperature of $60 \text{ }^\circ\text{C}$, strain rates seem to stabilize after 40 days in the range of $6 \cdot 10^{-9} \text{ s}^{-1}$, one order of magnitude higher than at ambient temperature.

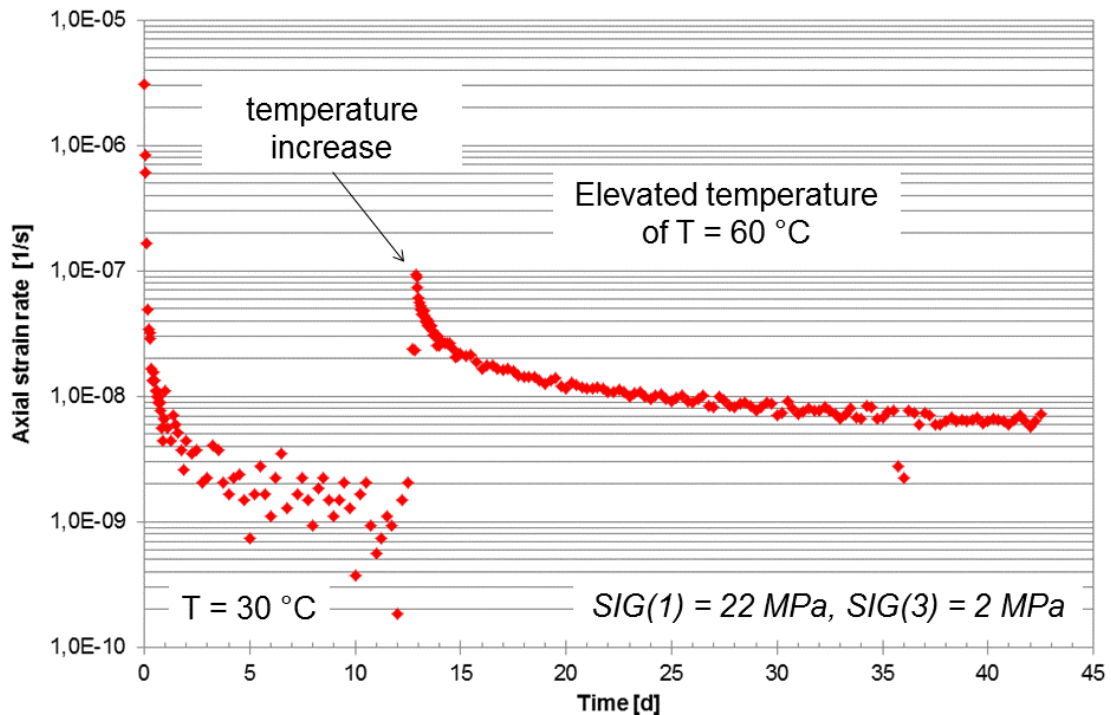


Fig. 3.35 Deformation behaviour of the intact concrete sample at ambient and elevated temperatures— derived strain rates

The pre-damaged samples show a totally different deformation behavior. While the strain rates of the intact sample slowly decrease with time in the testing interval at elevated temperature, the strain rates of the pre-damaged samples increase by one order of magnitude (see Fig. 3.36).

Obviously, the salt grit structure of the pre-damaged samples is not able to compensate the thermal dilatation process at the given deviatoric stress state of 20 MPa. Further experimental investigations and dedicated calculation activities are needed for interpretation of these unexpected experimental results and further prognosis.

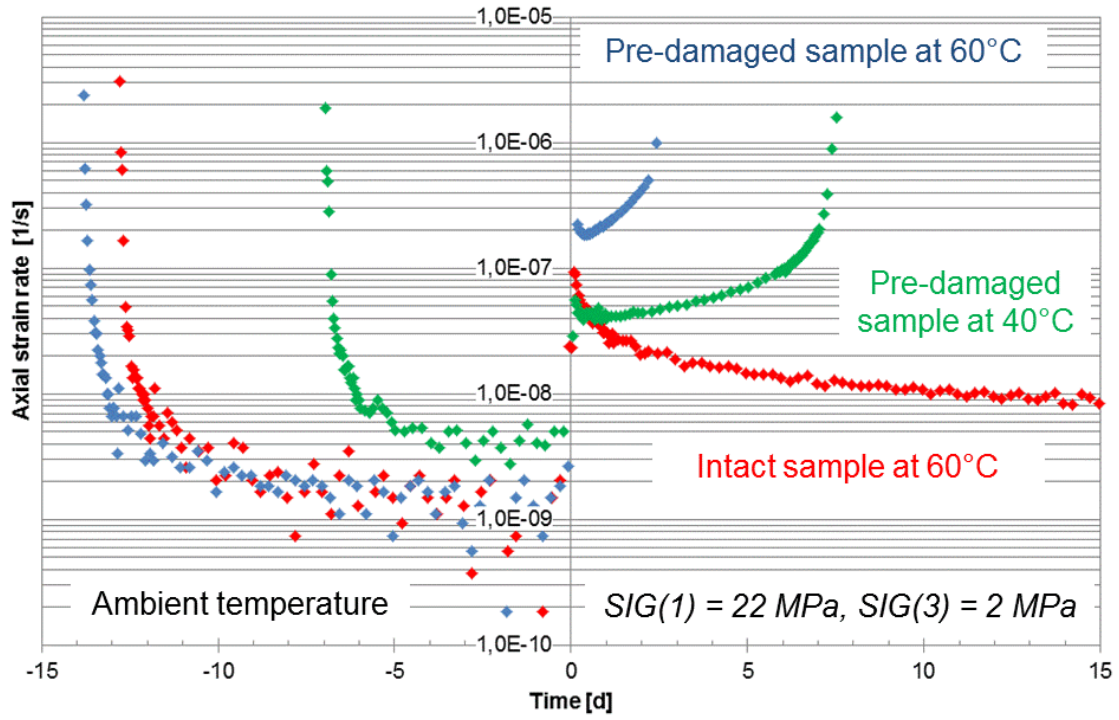


Fig. 3.36 Deformation behaviour of the tested concrete samples at ambient and elevated temperatures - standardized curve illustration showing derived strain rates

3.6 Sealing capacity of rock salt / sealing system

3.6.1 Experimental layout

For performing experiments on the system consisting of a salt concrete seal element and the surrounding dilated rock salt at the laboratory scale, the idea is to use hollow salt cylinders furnished with a central core of salt concrete which are placed in isostatic cells to impose confining stress. Thus, a combined sample represents the system of seal element, contact seam and surrounding rock at a small scale. The salt concrete core (35 mm in diameter) is placed in the hollow cylinder (70 mm in outer diameter and 100 mm in height) with a snug fit. In order to fill up potentially remaining voids, the core is coated with salt slurry and then pushed into the hollow salt cylinder. Excess slurry is removed and the sample is dried in an oven to avoid undefined saturation states. A photo of a salt concrete core, a hollow cylinder and the completed sample is shown in Fig. 3.37.

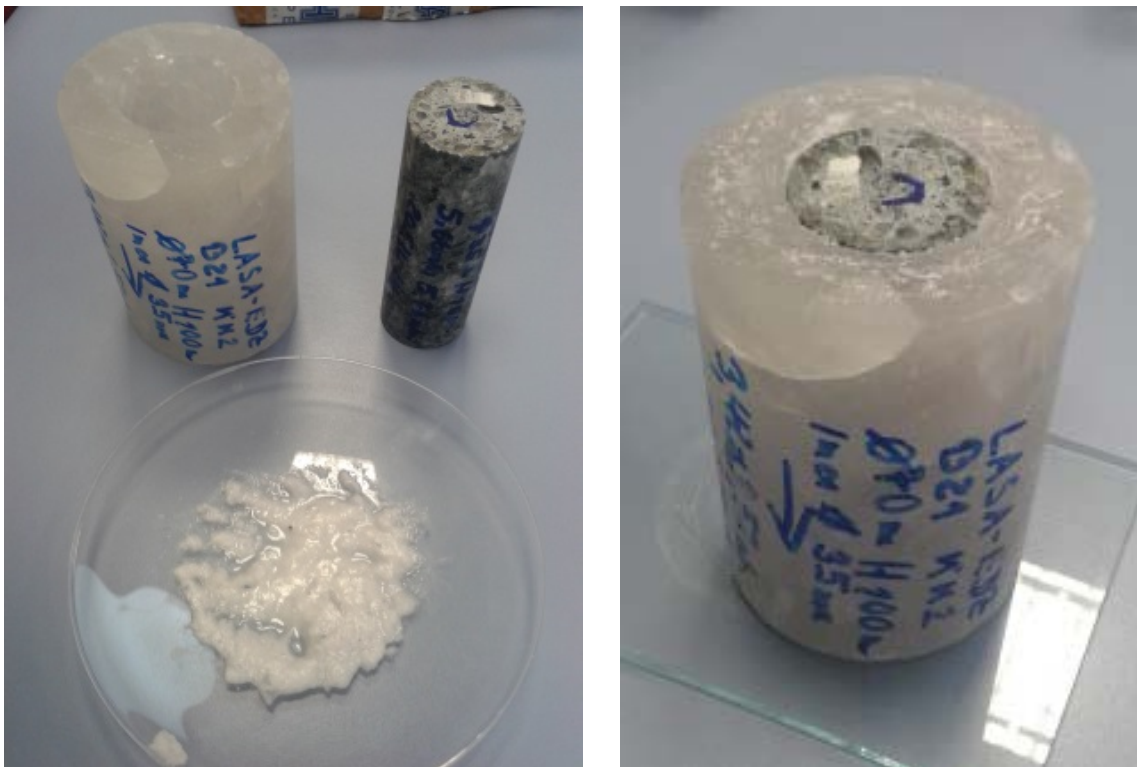


Fig. 3.37 Hollow salt cylinder, salt concrete core and salt slurry (left); complete combined sample (right)

The samples are coated with rubber jackets and placed in isostatic cells equipped with hydraulic lines to allow for axial flow-through of gas or liquid and determination of the

system permeability as shown in Fig. 3.38. A photo of a coated sample and the cell arrangement is shown in Fig. 3.39.

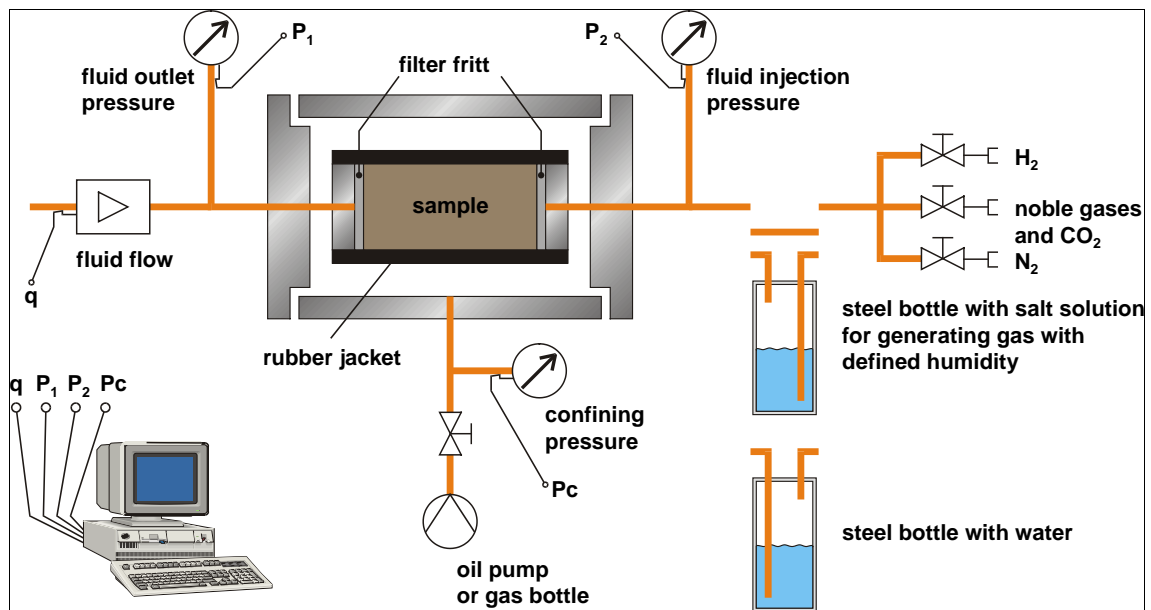


Fig. 3.38 Principal sketch of the modified Hassler cell for determining gas and water permeability



Fig. 3.39 Coated test sample (left); test equipment (right)

The cores were covered with a rubber jacket on the surface and two pistons on both ends. These pistons had a lead through for the fluids (gas or brine) which were used for the permeability measurements. In order to inject and withdraw the fluids homogeneously filter frits of stainless steel were placed at both ends between the pistons and the sample. The confining pressure on the sample was produced by an oil pump or by nitrogen from a gas bottle. This pressure could vary between 0.1 and 15 MPa.

At a special valve panel, the pressure of the test gas (nitrogen) was reduced from the pressure inside the gas tank (up to 20 MPa) to the injection pressure between 0.1 and

0.7 MPa. The injection pressure had to be less than 80% of the confining pressure in order to avoid gas flow along the surface between the sample and the rubber jacket.

For flooding the pore volume of the sample with brine and for brine permeability measurements this steel bottle could be filled with brine. The injection pressure was then generated by nitrogen connected to the bottle. The flow rate through the sample, the gas injection pressure, the gas outlet pressure and the confining pressure were recorded on a PC and additionally displayed for visual inspection.

3.6.2 Testing procedure

The test procedure is first to perform gas permeability tests of the dry sample while gradually increasing the compressive load. After unloading the sample saturated brine is injected and the stepwise loading is repeated, while the permeability of the seal system to brine is recorded. The evolution of the permeability of the composite sample to gas or to brine is the essential variable characterizing the recovery of the EDZ and the closing of the contact seam between salt concrete core and surrounding rock salt.

A pilot test was performed in order to check whether the sample composition and the measurement technique were suitable. After the test, the sample was dismantled and inspected. The pilot test showed that the test method is adequate to investigate evolution of the overall permeability of dry and brine-containing composite samples as a function of compressive load. It also showed that load changes have to be applied cautiously in order to maintain integrity of the testing arrangement.

For the start of detailed testing, two new samples were prepared. In order to increase the bandwidth of results, one sample featured an intact salt concrete core as taken from the in situ seal, while for the other sample a larger salt concrete core was loaded triaxially to the failure point and a smaller core was machined from the damaged core. The rationale of using a damaged salt concrete core as seal element is the fact that shrinkage fractures of a seal during construction cannot be excluded.

3.6.3 Measurement results and interpretation

Both the salt concrete cores and the rock salt cylinders were characterized in terms of permeability to gas before preparing the combined samples. Afterwards, gas and liquid

testing in the isostatic cells was started similarly to the pilot test. For characterization of the salt concrete cores, these were placed in isostatic cells and the load dependent gas permeability was determined under stepwise loading from 1 to 5 MPa. The permeability of the intact salt concrete core, calculated using Darcy's law, amounted to $2.3 \cdot 10^{-20} \text{ m}^2$ at 1 MPa isostatic load and fell below $1.0 \cdot 10^{-22} \text{ m}^2$ already at 2 MPa. This also showed that flow along the jacket interface is not an issue. For the damaged core, a moderate permeability decrease from $4.1 \cdot 10^{-18} \text{ m}^2$ at 1 MPa load to $1.6 \cdot 10^{-18} \text{ m}^2$ at 5 MPa was observed. The salt cylinders were subjected to the same tests before drilling the central holes for reception of the salt concrete cores. They also showed a permeability decrease with load: From $2.6 \cdot 10^{-19} \text{ m}^2$ to $2.5 \cdot 10^{-21} \text{ m}^2$ for the cylinder used with the intact salt concrete core and from $5.2 \cdot 10^{-20} \text{ m}^2$ to below $1.0 \cdot 10^{-22} \text{ m}^2$ for the cylinder used with the damaged one. The results of the load-dependent permeability tests of the individual material samples are summarized in Fig. 3.40.

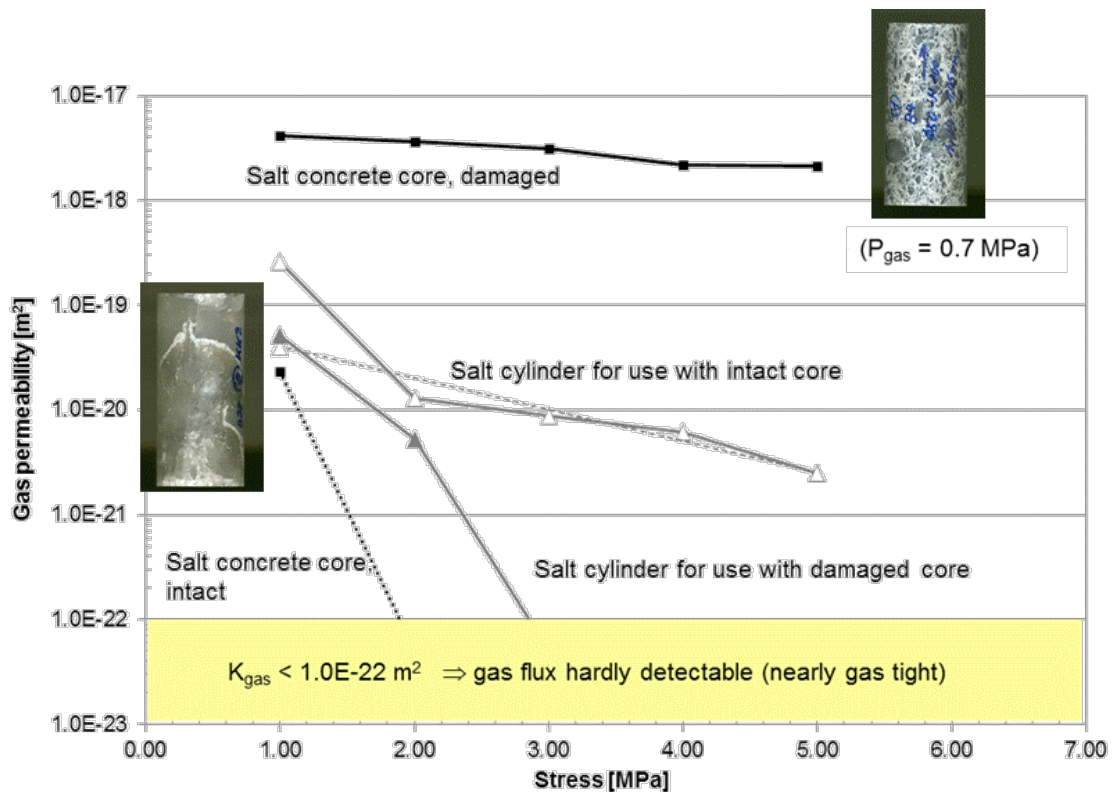


Fig. 3.40 Gas permeability of salt concrete cores and salt cylinders before assembly of combined samples

After characterization of the salt concrete and salt cores, the central holes were drilled into the salt cylinders and the combined samples were prepared as described earlier

(see Fig. 3.37). The potential effect of the sub-coring on the salt core gas permeability could not be quantified.

In the first stage of testing the combined samples, the confining load was increased by 1 MPa steps to 5 MPa over two weeks and gas flowed axially through the samples. For the sample with the intact seal element of salt concrete, the gas permeability decreased slightly from $2.5 \cdot 10^{-14} \text{ m}^2$ to $1.3 \cdot 10^{-14} \text{ m}^2$. When the sample was unloaded, the gas permeability remained at this value. The permeability measured was close to the upper limit of the testing arrangement. In fact, for the sample with damaged seal element gas permeability remained above the upper measurement limit of $5 \cdot 10^{-14} \text{ m}^2$.

The gas tests on dry samples showed the high impact of the contact seam – the overall permeability was much higher than the gas permeabilities of the individual materials. A second result of gas testing was that under dry conditions and moderate confining stress up to 5 MPa, a reconsolidation of the EDZ or a closing of the contact seam is negligible in the short term.

After gas testing, the samples were unloaded and brine was injected. Then, the samples were again loaded in steps of 1 MPa up to 5 MPa, and the permeability to brine was measured. The measurement results are shown in Fig. 3.41. The time until maximum load was three weeks for the two samples. Both samples showed a significant decrease of permeability to liquid with increased loading.

For the sample with the intact seal element, permeability decreased from an initial value of $4.5 \cdot 10^{-15} \text{ m}^2$ to below the detection limit of $1.0 \cdot 10^{-20} \text{ m}^2$ at a load of 5 MPa. Obviously, the salt surrounding the seal element became soft enough to enable very effective sealing of the contact seal and the EDZ in short time. The sample behaved significantly differently from the dry case, where only a slight gas permeability reduction was observed. Afterwards, the sample was gradually unloaded again. Permeability remained below the detection limit, showing that irreversible compaction had occurred. It is envisaged to dismantle the sample and confirm the reconsolidation and associated reduction of pathways by microscopic inspection.

As expected, the sample with the damaged seal element started at a higher permeability of $3.6 \cdot 10^{-13} \text{ m}^2$ (please note that the measurement limits for permeability measurement with liquid are different from those for gas tests). With increasing confining stress

the permeability decreased by two orders of magnitude, but it remained much higher than for the sample with the intact seal element.

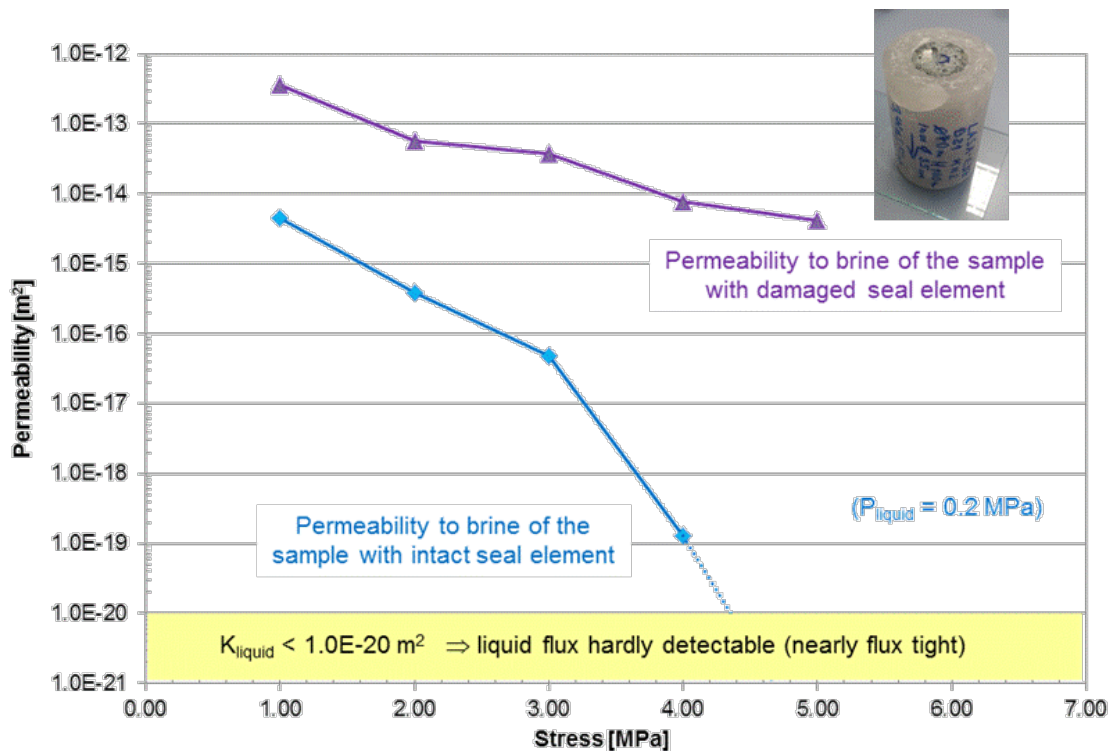


Fig. 3.41 Permeability of combined samples as a function of confining stress

While a compressive load of 5 MPa was sufficient to effectively seal the contact zone and the EDZ in the presence of brine in the experiment with the intact seal element, the same cannot be postulated for the experiment with the damaged seal element. Obviously, reconsolidation of the damaged seal element has not been achieved. The permeability value measured at 5 MPa confining stress, however, seems too high to attribute it to the flow through the seal element alone, as the gas permeability of the damaged salt concrete ranged between $1 \cdot 10^{-18} \text{ m}^2$ and $1 \cdot 10^{-17} \text{ m}^2$ (see Fig. 3.40).

This sample was not unloaded. The confining stress was increased in steps up to 10 MPa and the measurement of permeability to brine continues. Fig. 3.42 shows the permeability to brine as a function of time.

Obviously, the permeability value decreased not only with increasing confining pressure (light grey phase). The measurements showed a decrease of more than two orders of magnitude from $1 \cdot 10^{-15} \text{ m}^2$ down to $1 \cdot 10^{-18} \text{ m}^2$ within the next 100 days (2400 hours).

It is expected, that the permeability value will tend towards the detection limit without further increase of the confining pressure.

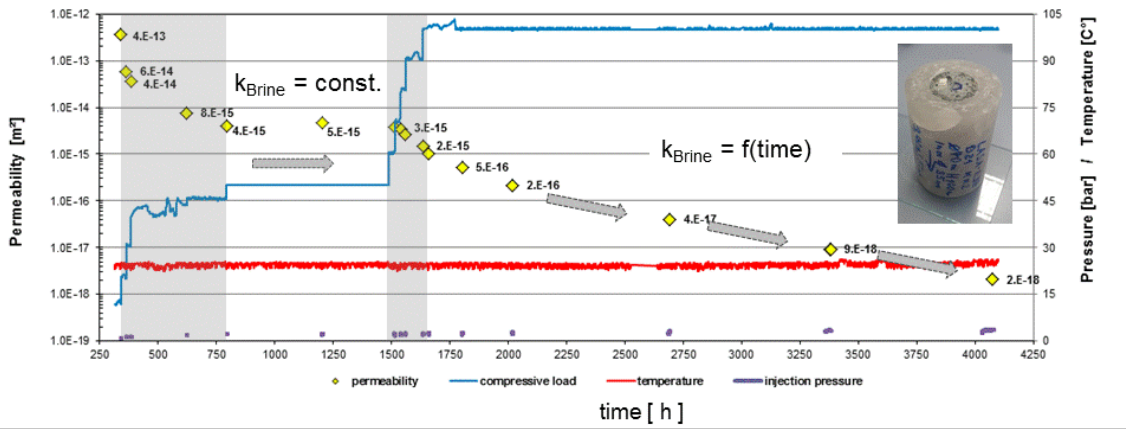


Fig. 3.42 Permeability to brine of the sample with damaged seal element as a function of time

4 Modelling work

4.1 Physical Modelling

The LINEAR ELASTICITY law describes linear elastic material behaviour according to HOOKE`S law. The Young's Modulus E increases with porosity reduction, see eq. (4.1).

$$E = E_0 + (\phi - \phi_0) \frac{dE}{d\phi} \geq E_{min} \quad (4.1)$$

The DISLOCATION CREEP law (DC) describes the creep behaviour of porous materials that include salt grains. Deformations are generated by intracrystalline deformation mechanism. The deformation depends on the deviatoric stresses.

Equation (4.2) describes the viscoplasticity. It is active for any stress level, because there is no yield condition. The parameter η describes the material viscosity, Φ is a scalar function, F is a stress function and G is a flow rule:

$$E \frac{d\varepsilon^{DC}}{dt} = \frac{1}{\eta_{DC}^d} \Phi(F) \frac{\delta G}{\delta \sigma'} \quad (4.2)$$

Parameters F and G are functions of the stress invariants (eq. (4.3)). The parameter n is the power of the rock power law and α_p describes a material parameter, defined in eq. (4.4):

$$G = \sqrt{q^2 + \left(\frac{-p}{\alpha_p}\right)^2} \Phi(F) = F^n \quad (4.3)$$

$$\alpha_p = \left(\frac{\eta_{DC}^v}{\eta_{DC}^d}\right)^{\frac{1}{n+1}} \quad (4.4)$$

The following equations describe the relationship of viscosity, void ratio and the dependence of deformation on temperature:

$$\frac{1}{\eta_{DC}^v} = A(T) g_{DC}^v(e) \quad (4.5)$$

$$\frac{1}{\eta_{DC}^d} = A(T) g_{DC}^d(e) \quad (4.6)$$

$$g_{DC}^v(e) = 3(g - 1)^n f \quad (4.7)$$

$$g_{DC}^d(e) = \left(\sqrt{\frac{1+g+g^2}{3}} \right)^{n-1} \left(\frac{2g+1}{3} \right) f + \frac{1}{\sqrt{g}} \quad (4.8)$$

$$A(T) = A_A \exp\left(\frac{-Q_A}{RT}\right) \quad (4.9)$$

Several parameters are needed for simulation activities using CODE_BRIGHT: A pre-exponential parameter A_A , which describes the ability to creep, the activation energy Q_A , which is equal to 54 000 J/mol and the stress power n , which is 5. The pre-exponential parameter is the varied parameter of this constitutive law during the simulation.

The basic equation for the VISCOPLASTICITY model (VP) is:

$$\frac{d\varepsilon}{dt} = A \langle \Phi(F) \rangle \frac{\delta G}{\delta \sigma} \quad (4.10)$$

Following relationships of the yield function F and the viscoplastic flow rule G are used for describing dilatancy:

$$\begin{aligned} F &= a_1 q - bp \\ G &= a_1 q - abp \\ \Phi(F) &= F^m \text{ for } F \geq 0; \Phi(F) = 0 \text{ for } F < 0 \end{aligned} \quad (4.11)$$

$$\begin{aligned} b &= a_3 + a_2(W_d)^{0.25} - a_4(W_d - W_{d0})^{0.25} \\ a &= a_5 + a_6 W_d + a_7(W_d - W_{d0})^2 \\ dW_d &= q d\varepsilon_d \end{aligned} \quad (4.12)$$

Parameters a_1 to a_7 were needed for calculation as well as the stress power m , the viscosity A and the activation energy Q . All parameters are listed in Tab. 4.1. Additionally, it is marked, which parameters were kept constant and which parameters were varied during the exercises. The influence of each parameter to the calculation process is explained shortly.

Tab. 4.1 Parameters for VP. Constant and varied parameters are marked and their influence on the process of calculation is described so far as known. Values, marked with *, were only varied by calculation of the tri-axial compression test: here the values were set to zero

Parameter	Value		Influence
	constant	varied	
Stress power m	8	-	Elastic step
Viscosity A	-	yes	Transient creep deformation
Activation energy Q	54 000 J/mol	-	
W_d	3.5	-	Work by plastic deformations
a_1	-	yes	Limit the volume increase and influence the breaking point
a_2	-	yes	Limit the volume increase
a_3	2.5	-	
a_4	0.7 (0)	*	Stable calculation process by $a_2 > 0$
a_5	0.02	-	
a_6	0.02 (0)	*	Stable calculation process by $a_2 > 0$
a_7	$a_7 = a_6$	-	

4.2 Numerical simulation of the triaxial compression test

4.2.1 Model geometry

To simulate the triaxial compression test, a model was designed similar to the laboratory TC-Test. This model consists of the salt concrete specimen with a length of 140 mm and the steel piston of the uniaxial apparatus with a length of 280 mm as shown in Fig. 4.1.

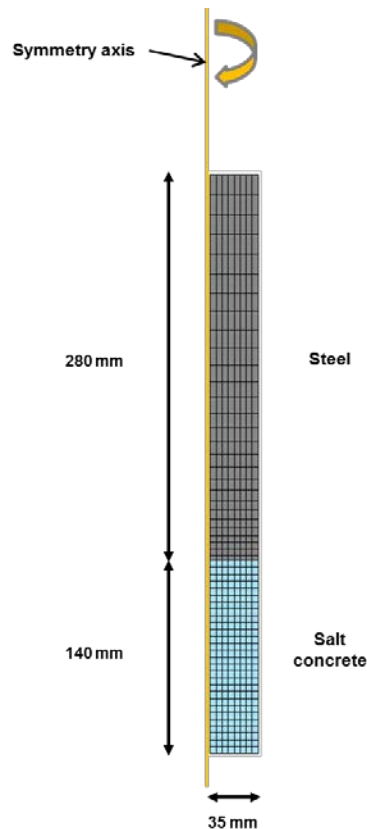


Fig. 4.1 Model of the salt concrete specimens for TC-Test for the numerical calculation using CODE_BRIGHT

The model was generated in GiD as an axial symmetric 2-D-model because of the symmetry of the salt concrete specimen. Consequently, the width of the model is 35 mm.

The mesh for simulation of the triaxial compression test was carried out with rectangular elements. The salt concrete was meshed with 224 elements. These elements are nearly quadratic and have the same dimension over the whole length of salt concrete

specimen. The steel piston consists of the same number of elements as the salt concrete. These elements are nearly of the same dimension near the boundary layer as the elements of salt concrete and they have an increasing ratio in y direction. In this way, the discretization near to the boundary layer became finer, because it was expected, that the deformation and stresses are sensitive in this zone. The number of nodes for the used mesh is 513. The mesh is shown in Fig. 4.2.

4.2.2 Boundary conditions and material properties

For constraining displacements in horizontal and vertical direction at the bottom of the salt concrete and in horizontal direction at the steel piston, nodal forces were generated at these parts of the model. The fixed boundary condition at the bottom does not accord with the real situation of the test specimen. But these boundary conditions were necessary for numerical calculation of the model. Axial and radial stresses were modeled as boundary stresses, see Fig. 4.2.

In calculations, only the deviatoric stress phase of TC-Test were modelled, because this phase is interesting for understanding the deformation behaviour of salt concrete and the dilatancy evolution. Following calculations were only done for a radial stress of 3 MPa.

Initial temperature, stress and porosity were generated on the surfaces of salt concrete and steel piston. The initial temperature corresponded to real temperature of 25 °C during the laboratory test and the initial stress correlated to atmospheric pressure of 0.1 MPa. Initial porosity of salt concrete was in accordance with average porosity of the specimens.

The used initial values are shown in Tab. 4.2.

Tab. 4.2 Values of initial conditions for TC-Test

	Salt concrete	Steel
Initial temperature [°C]	25	25
Initial stress [MPa]	-0.1	-0.1
Initial porosity [-]	0.06	0.001

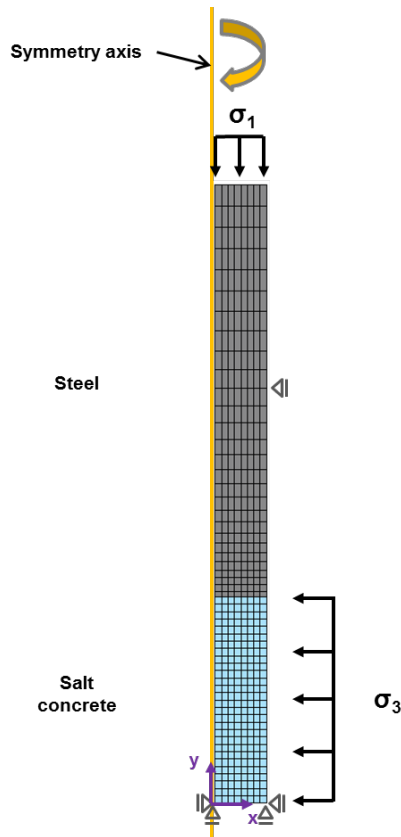


Fig. 4.2 Specimen for the TC-Test: Boundary conditions for numerical calculation using CODE_BRIGHT.

Different constitutive laws were used in order to describe the mechanical behaviour of the specimens. For the steel piston linear elastic material behaviour is expected, so HOOKE was used. The following calculation parameters are assigned, see Tab. 4.3:

Tab. 4.3 Material properties for LINEAR ELASTICITY law

	E-Modulus E [MPa]	Poisson ratio ν [-]	Reference porosity Φ₀ [-]
Salt concrete	10 000	0.18	0.06
Steel	210 000	0.27	0.001

According to the results of the laboratory tests salt concrete is supposed to have a linear elastic part and a viscoplastic part of deformation behaviour. Therefore, HOOKE and VP were used for first calculations. Secondly, the influence of stationary creep to TC-Test was investigated by DC.

Parameters for DC for salt concrete were taken from rock salt. This constitutive law for DC is able to simulate stationary creep. The used parameters are shown in Tab. 4.4.

Tab. 4.4 Material properties for DISLOCATION CREEP law

	Pre-exponential parameter $A_A [1/1 \cdot \text{MPa}^n]$	Activation energy $Q_A [\text{J/mol}]$	Stress power $n [-]$
Salt concrete	$0.26 \cdot 10^{-6}$	54 000	5

To describe transient creep and dilatancy of salt concrete, the constitutive model for VP was used. The parameters, which were used in the first calculation, derive from rock salt.

Tab. 4.5 Parameter for VISCOPLASTICITY model for description of transient creep and dilatancy of rock salt

Stress power $m [-]$	Viscosity $A [\text{MPa}^{-1} \cdot \text{s}]$	Activation energy $Q [\text{J/mol}]$	$a_6 [-]$	$W_{d0} [-]$
8	$5 \cdot 10^{-9}$	54.000	0.02	3.5
$a_1 [-]$	$a_2 [-]$	$a_3 [-]$	$a_4 [-]$	$a_5 [-]$
2.5	1.8	2.5	0.7	0.02

Additional to the parameters used for HOOKE, DC and VP parameters were needed for the description of solid phase properties. These selected parameters of salt concrete are similar to the parameters for rock salt, see Tab. 4.6. The density is the measured average density of the specimens from UCc-Tests.

Tab. 4.6 Solid phase properties for calculation using CODE_BRIGHT

	Specific heat $C_s [\text{J}/(\text{kg} \cdot \text{K})]$	Density $\rho_s [\text{kg}/\text{m}^3]$	Expansion coefficient $\alpha_s [1/^\circ\text{C}]$	Reference temperature $T_0 [^\circ\text{C}]$
Salt concrete	855	2 070	$4.2 \cdot 10^{-5}$	35
Steel	500	7 850	$1,0 \cdot 10^{-5}$	35

During the ongoing calculation activities selected parameters for viscoplasticity behaviour were varied. In this way, calculation results were able to fit to the laboratory results.

4.2.3 Modelling results versus experimental data

This modelling exercise was used for a better understanding of damage behaviour of salt concrete. Hence, only the compression phase of the laboratory tests was considered for simulation.

Exercise TC 1: HOOKE was used for describing material behaviour of the steel piston and HOOKE and VP were used for describing the salt concrete in the first modelling exercise. Because it was not possible to simulate the failure process of the sample, parameter a_1 was varied. In this way, the level of breaking point could be influenced.

Exercise TC 2: In the next step, failure parameters for the VP were varied, because it was not possible to describe the deformations behaviour analogue to laboratory tests by only varying a_1 . VP was chosen, because only this constitutive model is able to describe the nonlinear deformation behaviour of salt concrete as seen in the results of the laboratory tests. Parameter a_2 limits the extension of volume strain, if it is bigger than zero, a_4 and a_6 influence the stability of calculation process for $a_2 > 0$. For describing the triaxial tests, it is necessary, that the specimens deform volumetrically. So, all these parameters were set to zero in order to allow volumetric deformations. The parameter a_1 was used again for varying the failure point at once.

Exercise TC 3: In the third exercise, best fitting parameters from previous calculations were used, but with using DC additionally. It was tested, whether stationary creep is triggered in this kind of calculations or not. In the laboratory tests stationary creep was not expected due to the fact that the execution of the tests was very short. It is important to know for further calculations, if the DC considers this circumstance.

Verification: The calculation exercises, described before, were executed for the conditions of the triaxial test with a radial stress of 3 MPa. Then, the laboratory test with a radial stress of 1 MPa and 2 MPa was simulated using the parameters of Exercise TC 3 from the triaxial test with a radial stress of 3 MPa. In this way it was shown, whether the parameters are applicable to all TC-Tests.

The following Tab. 4.7 shows the calculation time steps for different radial stresses.

Tab. 4.7 Calculation time steps of calculation for the compaction phase of TC-Test with different radial stresses

Interval	Time [hours]	Simulation
Radial pressure of 1 MPa		
1	0.0 – 0.1	Axial and radial stress of 1 MPa
2	0.1 – 6.3	Axial stress increases to 38 MPa by a loading of 0.1 MPa per minute. Constant radial stress of 1 MPa.
Radial pressure of 2 MPa		
1	0.0 – 0.1	Axial and radial stress of 2 MPa
2	0.1 – 6.4	Axial stress increases to 40 MPa by a loading of 0.1 MPa per minute. Constant radial stress of 2 MPa.
Radial pressure of 3 MPa		
1	0.0 – 0.1	Axial and radial stress of 3 MPa
2	0.1 – 7.4	Axial stress increases to 44 MPa by a loading of 0.1 MPa per minute. Constant radial stress of 3 MPa.

In Exercise TC 1 HOOKE was used for describing the material behaviour of the steel piston and HOOKE and VP were used for describing the material behaviour of salt concrete. VP should describe shear thickening material behaviour of salt concrete analogue to the TC-Test. The used constitutive laws, their parameters and the varied ones are summarized in Tab. 4.8.

Tab. 4.8 Used constitutive laws for modelling salt concrete TC behaviour (varied parameters are marked in red)

LINEAR ELASTICITY	E [MPa]	ν [-]	ϕ_0 [-]		
	10 000	0.18	0.06		
DISLOCATION CREEP	A_A [1/1*MPaⁿ]	Q_A [J/mol]	n [-]		
	-	-	-		
VISCOPLASTICITY	m [-]	A [MPa⁻¹*s]	Q [J/mol]	a_6 [-]	W_d [-]
	8	$5 \cdot 10^{-9}$	54 000	0.02	3.5
	a_1 [-]	a_2 [-]	a_3 [-]	a_4 [-]	a_5 [-]
	varied	1.8	2.5	0.7	0.02

The first calculation was executed using all parameters corresponding to Tab. 4.5. Parameter a_1 was equal to 2.5. The nodes, at which stresses and displacements were detected for further evaluation of the results, are shown in Fig. 4.3.

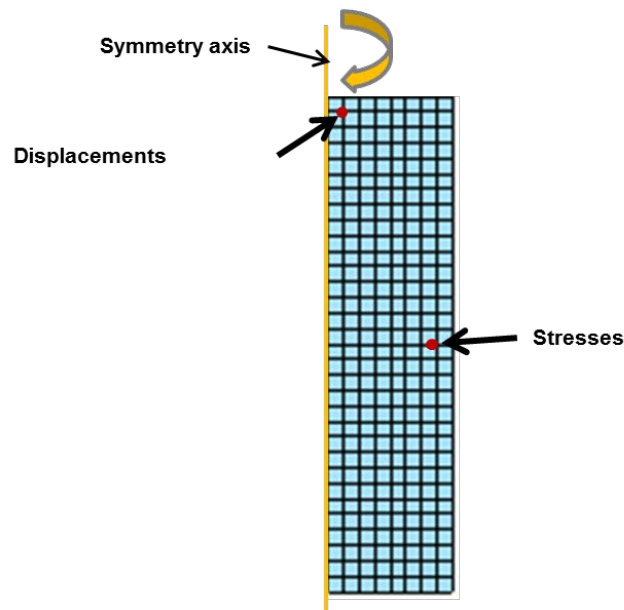


Fig. 4.3 Nodes on the specimen, at which stresses and displacements were detected.

The purple curve in Fig. 4.4 shows the results received with parameter a_1 equal to 2.5. Here the deviatoric stress respectively the volumetric strain is shown versus the axial strain. The laboratory results are shown in grey. The calculation process stopped before the final axial stress of 44 MPa was reached according to the lab test results, because the calculation failed at a deviatoric stress of 23 MPa. There was no dilatancy foreseen so that the specimen failed directly. This is used to see the development of volumetric strain. In laboratory tests dilatancy occurs, if the curve deviates from the linear slope. In the mode, calculations stopped directly, if the curve started to deviate from the linear slope. So no increase of porosity and consequently no dilatancy were modelled.

Now the stability of salt concrete was improved in order to load the specimen with the whole axial stress corresponding to the laboratory test. Therefore, the parameter a_1 was decreased. In this way, the stability of salt concrete increased. This proceeding aims to find the value of a_1 , at which the specimen carries the whole deviatoric stress of 44 MPa. The results are shown in Fig. 4.4. If a_1 decreased, the specimen was able to carry higher deviatoric stresses. Calculation process stopped later by using a decreased a_1 and consequently increased the material stability. A full calculation was executed successfully by a_1 equal to 1.93. The aim, that an execution of the whole calculation process is possible, was finally reached. The specimen could carry the whole de-

viatoric stress. But the simulation curve shows a linear gradient and an adaptation to the curve of laboratory test does not occur.

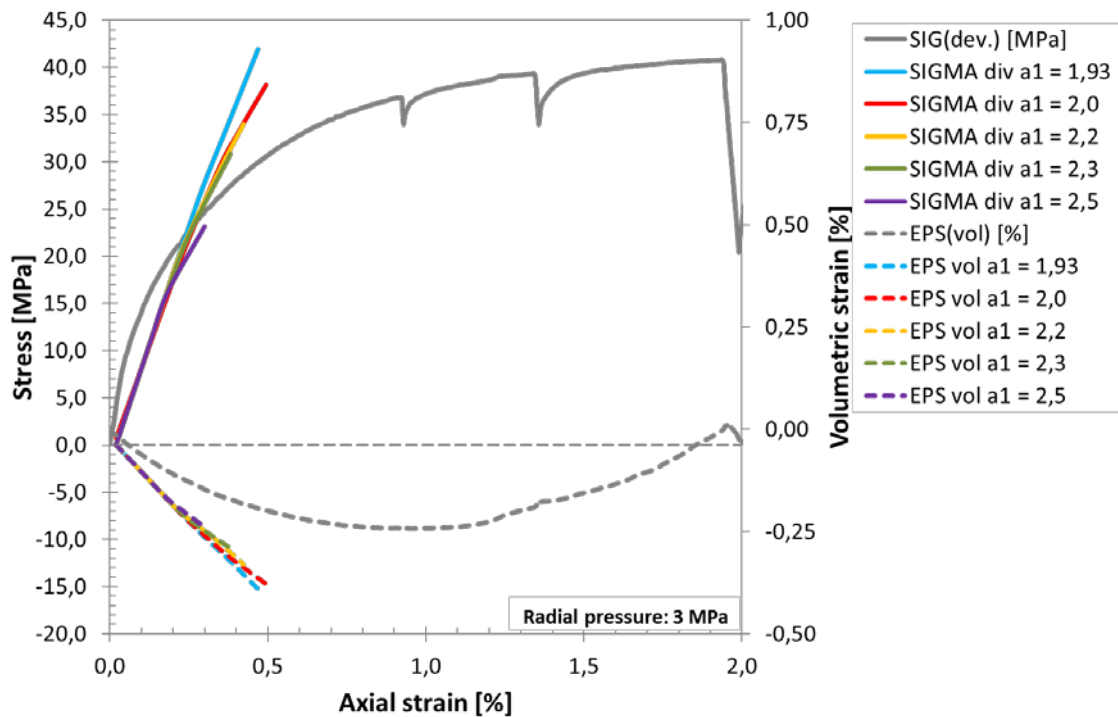


Fig. 4.4 Results of Exercise TC 1. Here LINEAR ELASTICITY law and VISCOPLASTICITY model are used. Axial load is 44 MPa

In Exercise TC 2 also HOOKE and VP were used. All parameters are summarized in Tab. 4.9. This exercise aimed to find a combination of parameters, which allows an increase of porosity and consequently a volume increase and onset of dilatancy for a better adaptation of calculation to laboratory results.

Tab. 4.9 Used constitutive laws for modelling salt concrete TC behaviour (varied parameters are marked in red)

LINEAR ELASTICITY	E [MPa]	ν [-]	ϕ_0 [-]		
	10 000	0.18	0.06		
DISLOCATION CREEP	A_A [1/1*MPa ⁿ]	Q_A [J/mol]	n [-]		
	-	-	-		
VISCOPLASTICITY	m [-]	A [MPa ⁻¹ *s]	Q [J/mol]	a_6 [-]	W_d [-]
	8	$5 \cdot 10^{-9}$	54 000	0	3.5
	a_1 [-]	a_2 [-]	a_3 [-]	a_4 [-]	a_5 [-]
	varied	0	2.5	0	0.02

Initial point of Exercise TC 2 should be a calculation, which is comparable to the result of Exercise TC 1: A linear slope, which describes the stress load without failure of the specimen and without onset of dilatancy. This is necessary for a better interpretation of further calculation results. But the material stability corresponding to Exercise TC 1 was not sufficient anymore, because a_2 , a_4 and a_6 were set to zero now and allow maximal extension of volume (If a_2 , a_4 and a_6 are zero, W_d drops out). Consequently, the material stability decreased. Hence, a_1 was decreased to 1.33 for reaching a higher failure point and reaching the requirements corresponding to the exercise before (compare Fig. 4.5).

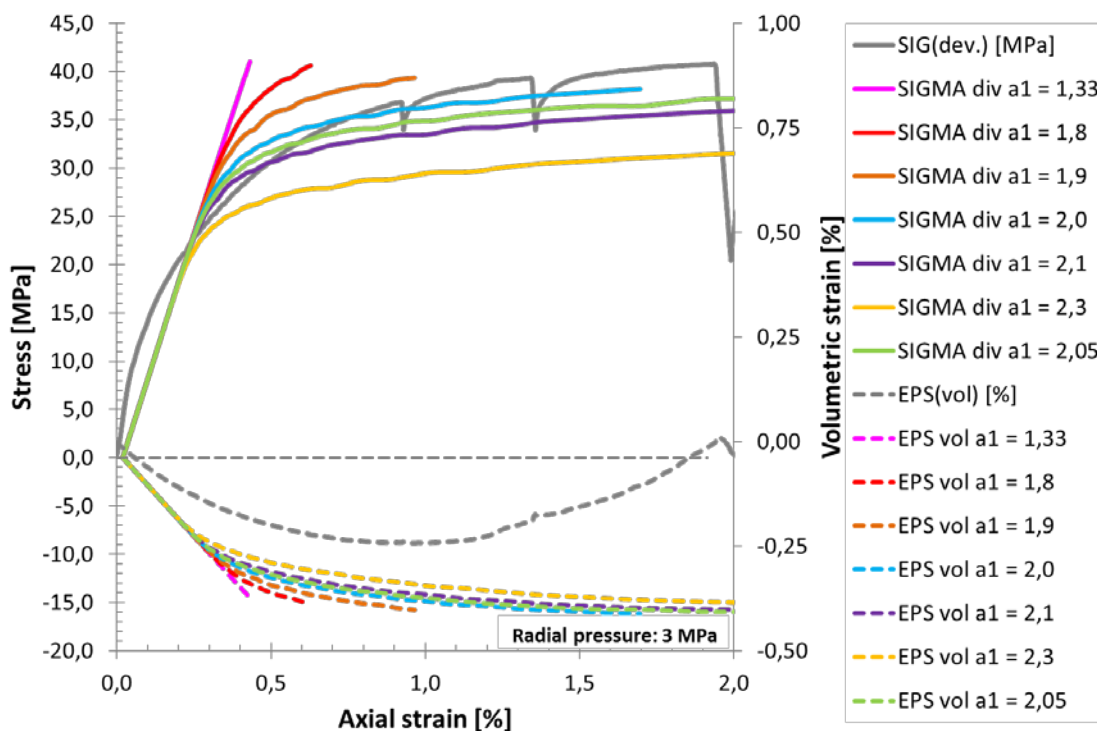


Fig. 4.5 Results of Exercise TC 2. Here LINEAR ELASTICITY law and VISCOPLASTICITY model are used. Parameters a_2 , a_4 and a_6 are set to zero. a_1 is varied. For further calculations $a_1 = 2.05$ is chosen (green curve)

Below, a_1 was increased step by step. Fig. 4.5 shows a representative assortment of the results of executed calculations. All curves show a linear gradient at first, the gradient of all curves decreases dependent to the value of a_1 . The calculations of Exercise TC 2 were executed completely. Maximal reached axial strains were determined by the stiffness of the material. The stiffness respectively stability of the material depends on the value of a_1 . If a_1 was small, the material had a higher stiffness and less deformation.

If a_1 was increased, the material stiffness became smaller and axial strains were higher. Additionally, the maximal acceptable deviatoric stress is smaller by a salt concrete with smaller stiffness. So the gradient of the curves approximates to the horizontal line after the stress limit was reached (as can be seen at the curves by a_1 equal to 2.05 / 2.1 and 2.3): Axial strains further increase but deviatoric stress stays nearly constant.

In consideration of the development of volumetric strain is to see, that the curves differ clearly to the linear slope. So an increase of porosity and consequently an onset of dilatancy were simulated by using parameters after Tab. 4.10.

For further calculations a value of a_1 equal to 2.05 was chosen, because this curve describes the laboratory test in the best manner in maximal deviatoric stresses and in reached axial strain.

In Exercise TC 3 the influence of DC to the TC-Test by numerical calculations was checked. Normally stationary creep, which was simulated by DC, should have no influence on the deformations, if the test period is only a few hours as in this TC-Test. For further calculation it is important to know, whether CODE_BRIGHT considers this circumstance. Below the calculations results from Exercise TC 2 are opposed to the results from Exercise TC 3, which considers HOOKE, DC and VP.

Tab. 4.10 Used constitutive laws for modelling salt concrete TC behaviour (varied parameters are marked in red)

LINEAR ELASTICITY	E [MPa]	ν [-]	ϕ_0 [-]		
	10 000	0.18	0.06		
DISLOCATION CREEP	A_A [1/1*MPaⁿ]	Q_A [J/mol]	n [-]		
	0.26·10 ⁻⁶	54 000	5		
VISCOPLASTICITY	m [-]	A [MPa⁻¹*s]	Q [J/mol]	a_6 [-]	W_d [-]
	8	5·10 ⁻⁹	54 000	0.0	3.5
	a_1 [-]	a_2 [-]	a_3 [-]	a_4 [-]	a_5 [-]
	2.05	0.0	2.5	0.0	0.02

The results in Fig. 4.6 show, that DC has no influence on the deviatoric stress and the volumetric strain. The curves of both parts of calculation are nearly identical. The small deviations could also derive from the individual steps of iteration during calculation.

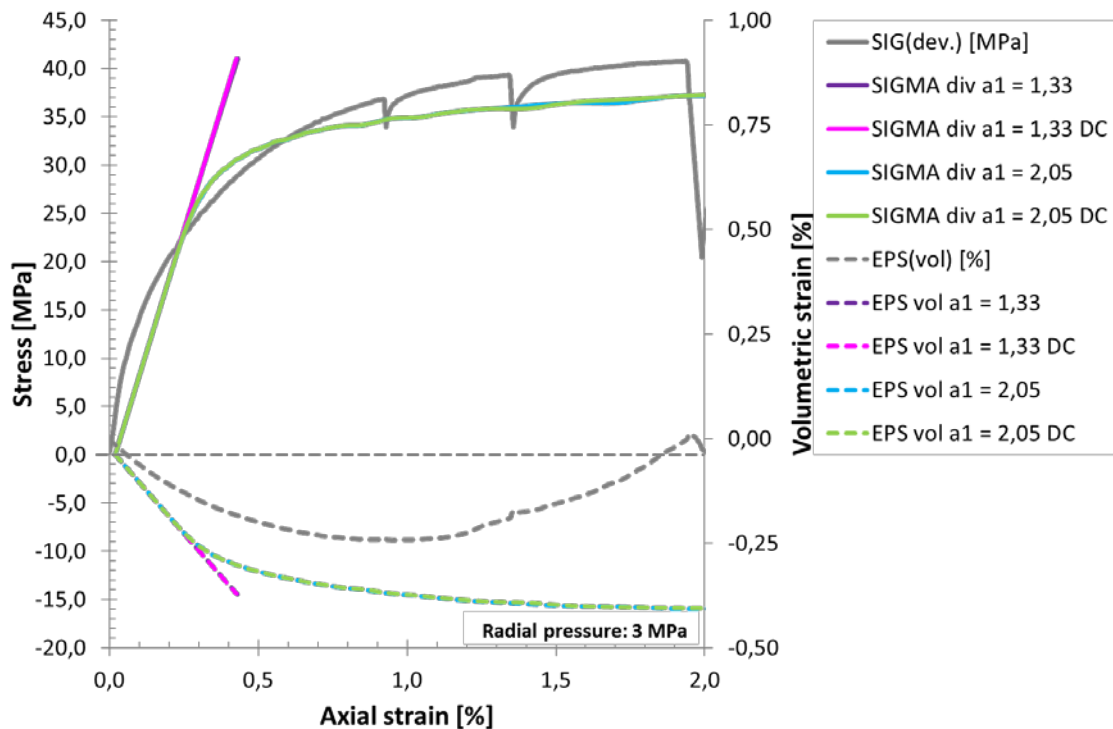


Fig. 4.6 Comparison of calculation results of Exercise TC 2 and TC 3 with and without DISLOCATION CREEP law. The results confirm that DISLOCATION CREEP law is only considered by longer time periods. Calculations, which were executed with DISLOCATION CREEP law are marked with “DC”

Consecutively, the onset of dilatancy was considered on the basis of calculation results. For this the results from Exercise TC 2 were used with values of a_1 equal to 1.33 and 2.05. The results are shown in Fig. 4.7. The onset of dilatancy is described by the deviation of the curve of volumetric strain from the linear slope by a_1 equal to 1.33. The criterion for the onset of dilatancy was chosen differently than the criterion used for the laboratory test analysis. In the calculation results no increase of volumetric strain was reached, which was the used criterion in the laboratory tests. So the criterion of the laboratory tests was not applicable here. If dilatancy insert in Exercise TC 2, the axial strain was around 0.22 % and the deviatoric stress was 21 MPa. Generally, the reached deviatoric stress is circa 3 MPa smaller than in the laboratory test. It was around 37 MPa. The volumetric strains are circa 50 % higher than the maximum volumetric strain of laboratory tests by an axial strain of 0.9 %. But basically, the calculations results characterize the general trend of the laboratory test.

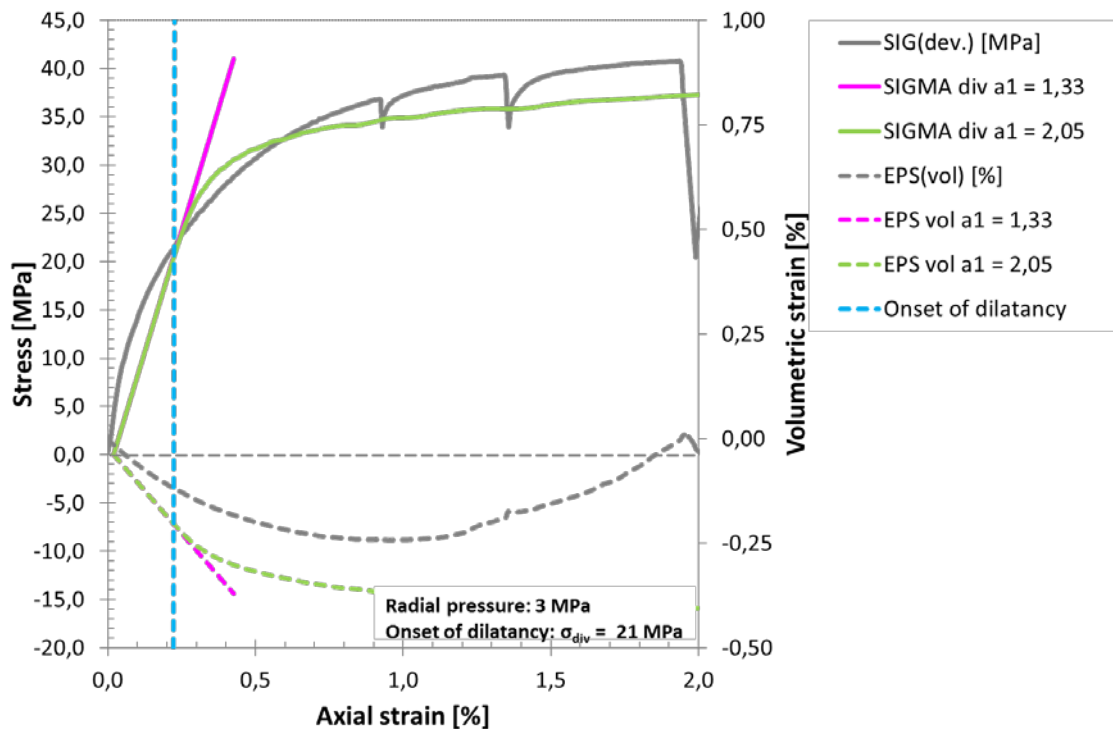


Fig. 4.7 Calculation results of Exercise TC 2 and a radial stress of 3 MPa. The pink curve shows the results without dilatancy, the green one with dilatancy. The onset of dilatancy is defined as the start of deviation of the curve with dilatancy to the linear curve without dilatancy

All calculations in this chapter correspond to the conditions of the TC-Test by a radial stress of 3 MPa until now. Currently, the chosen parameters were verified by calculations of the TC-Test with radial stresses of 1 and 2 MPa. HOOKE and VP were used corresponding to Exercise TC 2.

Fig. 4.8 shows the calculation results with a radial stress of 2 MPa. The onset of dilatancy was nearly at the same point by a radial stress of 2 MPa as by a radial stress of 3 MPa. If the dilatancy inserts, a deviatoric stress of 21 MPa and an axial strain of 0.23 % were reached. The deviatoric stress during calculation was 3 MPa smaller than in the laboratory tests. These values correspond to the results of Exercise TC 2 with a radial stress of 3 MPa. The development of the calculated volumetric strains accords here very well with the volumetric strains of laboratory test. The curve progression is nearly the same until the volume of the laboratory specimen increases. This increase of volume could not be described by the VP and the used parameters of Exercise TC 2.

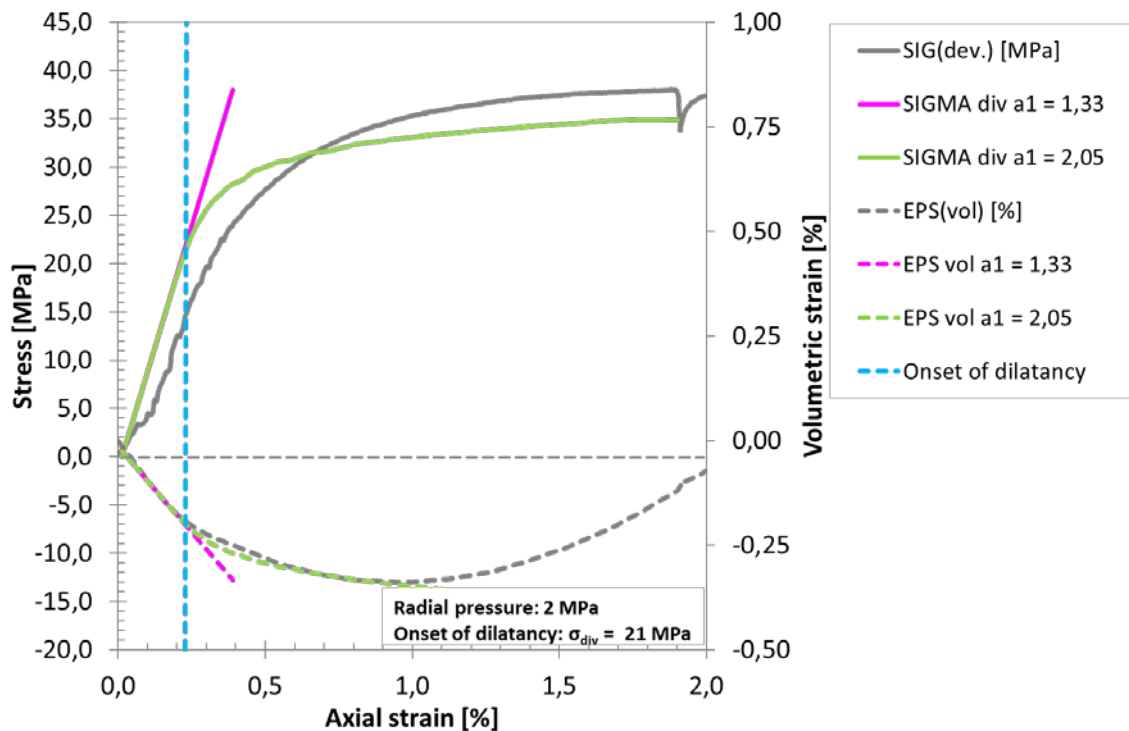


Fig. 4.8 Calculation results of Exercise TC 2 and a radial stress of 2 MPa. The pink curve shows the results without dilatancy, the green one with dilatancy. The onset of dilatancy is defined as the start of deviation of the curve with dilatancy to the linear curve without dilatancy

The conditions for the onset of dilatancy by a radial stress of 1 MPa are different to the calculations before, see Fig. 4.9. Here the onset of dilatancy was reached at an axial strain of 0.18 % and a deviatoric stress of 17 MPa. The stability of the specimen decreases, because of the lower radial stress. This corresponds to the results of the laboratory test. The maximal deviatoric stress in the laboratory test was 36 MPa, in the calculation 33 MPa. The difference between these values of deviatoric stress of laboratory and calculations results is the same as in the calculations results before. Certainly, there is again a difference of volumetric strains between laboratory and calculations results. Both volumetric strains are smaller than in tests before. A reason for the decrease of both volumetric strains could be the smaller radial stress and the resulting loss of stability. So the specimen cannot compact in the same range as before, because it was damaged earlier. The smaller deviatoric stress level by the onset of dilatancy supports this thesis.

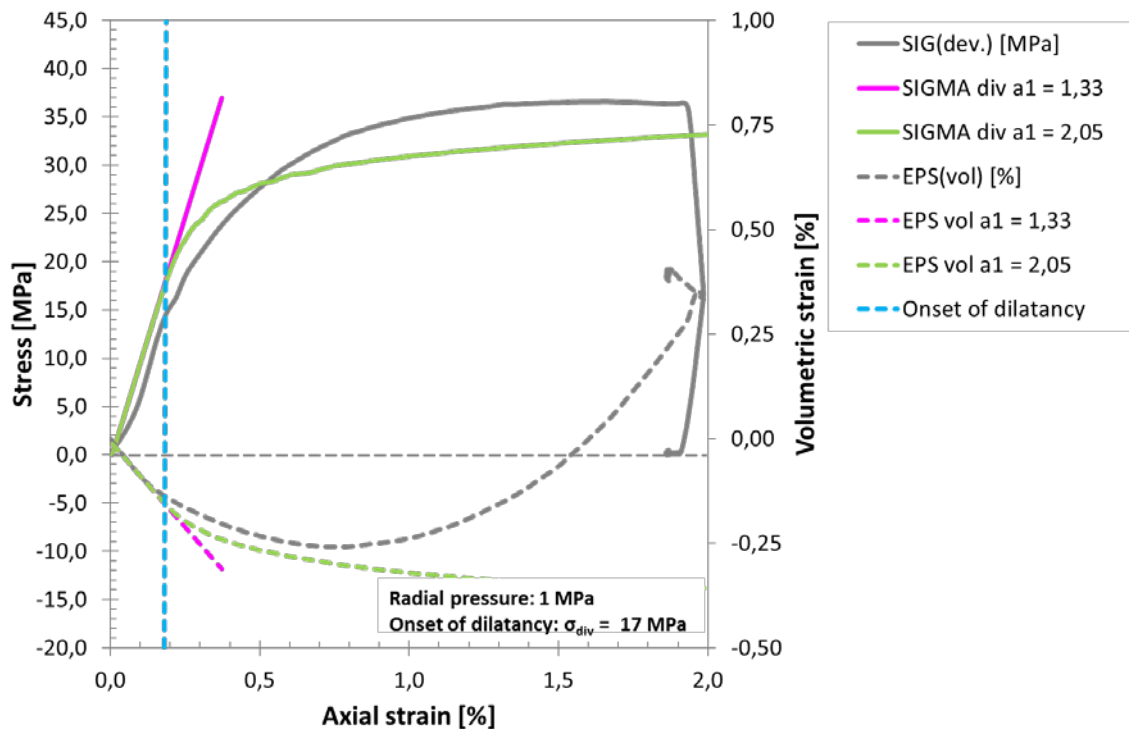


Fig. 4.9 Calculation results of Exercise TC 2 and a radial stress of 1 MPa. The pink curve shows the results without dilatancy, the green one with dilatancy. The onset of dilatancy is defined as the start of deviation of the curve with dilatancy to the linear curve without dilatancy

4.2.4 Discussion

The comparison between laboratory and calculation results shows, that simulation of the TC-Test on salt concrete is possible by using HOOKE and VP. Therefore, VP has been varied with respect to rock salt. The final parameters used for TC-Test are summarized in Tab. 4.11.

Deficits of the TC-Test simulation are that volume increase as a reaction to the damage of the specimen cannot be considered as well as the respective reduction of stresses, if the failure level was reached. Equivalent to the calculation results of TC-Test it can be expected that the onset of dilatancy in the UCc-Test starts during the increase of axial stresses from 10 MPa to 20 MPa.

The results of this chapter are considered by the simulation of the UCc-Test using the VP parameter set in Tab. 4.11.

Tab. 4.11 Final parameters used for the Linear Elasticity law and VISCOPLASTICITY model in TC-Test

LINEAR ELASTICITY	E [MPa]	ν [-]	ϕ_0 [-]		
	10 000	0.18	0.06		
VISCOPLASTICITY	m [-]	A [MPa⁻¹*s]	Q [J/mol]	a₆ [-]	W_d [-]
	8	5·10 ⁻⁹	54 000	0	3.5
	a₁ [-]	a₂ [-]	a₃ [-]	a₄ [-]	a₅ [-]
	2.05	0	2.5	0	0.02

4.3 Simulation of the uniaxial creep test

4.3.1 Model geometry

For simulation of the uniaxial creep test, a model was designed similarly to the model of the TC-Test in GiD. The length of the salt concrete specimen is 160 mm and the length of the steel piston is 320 mm as shown in Fig. 4.10. The width of this model is 40 mm. Due to the symmetry of the salt concrete specimen this model was generated in terms of an axial symmetric 2-D-model.

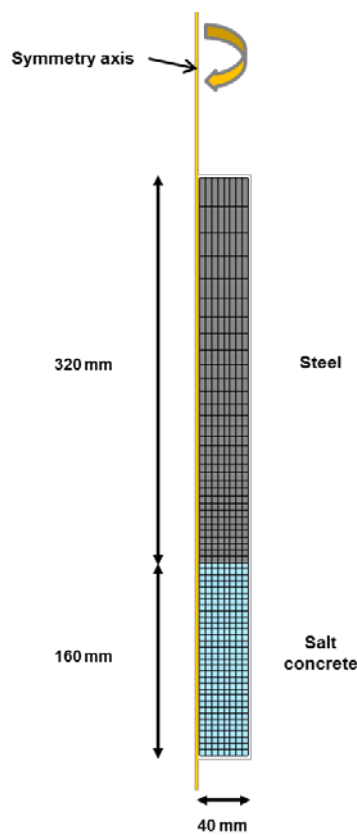


Fig. 4.10 Model of the salt concrete specimens for UCc-Test for the numerical calculation using CODE_BRIGHT, showing geometry and meshing details

The mesh of this model was carried out with rectangular elements. The salt concrete was meshed with 256 quadratic elements using the same dimension. The feed size averages 0.5 mm in each case. The steel piston consists of 256 elements. These elements are nearly quadratic at the boundary layer to the salt concrete and become rectangular in y direction. The reason was the same as at the TC-Test calculation exercises: to get a finer discretization near the boundary layer. The number of nodes for the

whole model was 585. The mesh is shown in Fig. 4.10. Due to the layout of the mesh, displacements at the contact zone between the salt concrete specimen and the steel piston were not possible.

4.3.2 Boundary conditions and material properties

Boundary conditions were generated as nodal forces at the bottom of the salt concrete specimen and as collateral ones at the steel piston. They constrain displacements in horizontal and vertical direction at the bottom of the salt concrete and horizontal displacements at the steel piston. The fixed boundary condition at the bottom does not represent the situation in the laboratory, but was necessary for numerical calculations. Axial stress was modelled as boundary stress at the top of the steel piston. The axial stresses (σ_1) reached from 5 MPa to 20 MPa. An atmospheric pressure (p_{atm}) of 0.1 MPa was applied radially to the salt concrete specimen (compare Fig. 4.11).

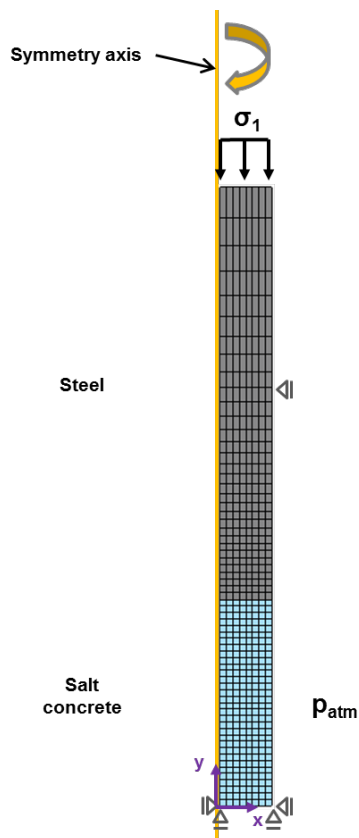


Fig. 4.11 Specimen for the UCc-Test: Depiction of conditions for numerical calculation using CODE_BRIGHT

Initial temperature, stress and porosity were generated on the surfaces of salt concrete and steel piston similarly to the TC-Test. The parameters were the same as in the calculation exercise before (compare Tab. 4.1).

Different constitutive laws were used in order to describe the mechanical behaviour of the specimens. For the steel piston HOOKE was used as in TC-Test. According to the results of the UCc-Test, salt concrete is supposed to have a linear elastic part and a viscoplastic part of deformation behaviour. Therefore HOOKE, DC and VP were used for calculation. Parameters for HOOKE are shown in Tab. 4.12.

Tab. 4.12 Finally used parameters for the Linear Elasticity law

	E-Modulus E [MPa]	Poisson ratio ν [-]	Reference porosity Φ₀ [-]
Salt concrete	10 000	0.18	0.06
Steel	210 000	0.27	0.001

Parameters for the calculation of DC for salt concrete were taken from rock salt in the first calculation because salt concrete includes around 70 % crushed salt and there are no creep parameters for salt concrete until now. This constitutive law for DC is only able to describe stationary creep. The parameters are shown in Tab. 4.13.

Tab. 4.13 Material properties for DISLOCATION CREEP law of saline materials

	Pre-exponential parameter A_A [1/1*MPaⁿ]	Activation energy Q_A [J/mol]	Stress power n [-]
Salt concrete	$2.08 \cdot 10^{-6}$	54 000	5

To describe transient creep and dilatancy of salt concrete, the VP was used. The parameters are shown in Tab. 4.14.

Tab. 4.14 Parameter for VISCOPLASTICITY model for description of transient creep and dilatancy of salt concrete

Stress power m [-]	Viscosity A [MPa⁻¹*s]	Activation energy Q [J/mol]	a₆ [-]	W_{d0} [-]
8	$5 \cdot 10^{-9}$	54 000	0.02	3.5
a₁ [-]	a₂ [-]	a₃ [-]	a₄ [-]	a₅ [-]
2.5	1.8	2.5	0.7	0.02

Additional to the parameters used for HOOKE, DC and VP, some parameters were needed for description of solid phase properties (Tab. 4.6).

4.3.3 Modelling results versus experimental data

Different types of exercises were executed for finding the best approximation of calculation results to the laboratory test findings.

Exercise UCc 1: HOOKE and DC were used. First, a calculation was executed using parameters corresponding to rock salt, because salt concrete consists of about 70 % crushed salt. So potentially a time dependent deformation behaviour similar to rock salt by stationary creep is expected. Further calculations were executed using varied pre-exponential parameters. In this way, a creep class should be found, which describes real strains and strain rates of salt concrete related to stationary creep. Calculated creep classes and appropriate pre-exponential parameter are shown in Tab. 4.15.

Tab. 4.15 Variation of creep classes and appropriate pre-exponential parameters for first calculations /BGR03/

Creep class	0	1	2	3	4	5	6
Pre-exponential parameter	$0.065 \cdot 10^{-6}$	$0.13 \cdot 10^{-6}$	$0.26 \cdot 10^{-6}$	$0.52 \cdot 10^{-6}$	$1.04 \cdot 10^{-6}$	$2.08 \cdot 10^{-6}$	$4.16 \cdot 10^{-6}$

Exercise UCc 2: Now the pre-exponential parameter for each stress level was varied. For each stress level the pre-exponential parameter was considered individually. The pre-exponential parameter was used independently to the creep classes, because it was expected, that a better adaptation to the laboratory results could be reached. Here HOOKE and DC were used.

Exercise UCc 3: This exercise considered only the third stress level of 20 MPa (marked as phase 2), because laboratory tests and calculations before showed, that there is a difference between the deformation behaviour in the first and second stress level and the third stress level. Exercise UCc 3 aimed to describe the combination of linear elastic, transient and stationary creep and shear thickening deformations. Exercise UCc 3 was subdivided in parts a) to d). In part a) calculation was executed on the basis of the results from TC-Test using HOOKE and VP with parameters from Exercise TC 2. Part b) described the deformation behaviour including HOOKE and VP, but here volumetric extensions were limited again and the material stability was increased. In part c) calculations were executed using HOOKE, VP and additional DC. The pre-exponential parameter was adapted. Finally, the shear thickening deformations were

adapted again in part d), because the interaction of HOOKE, VP and DC had to be considered.

Exercise UCc 4: Now the VP was adapted to stress levels of 5 MPa and 10 MPa (marked as phase 1). HOOKE, DC and VP should simulate linear elastic and transient creep deformations. DC was used because it was expected, that the influence of stationary creep is very small in phase1 corresponding to laboratory results. This assumption was checked. Furthermore, the influence of stationary creep in phase 2 will be considered in the end of Exercise UCc 4 again.

Exercise UCc 4 was subdivided in three parts. Part a) investigated the influence of viscosity to transient creep. In part b) the stiffness of the salt concrete was adapted by parameter a_1 . Finally, the volumetric extension was adapted by parameter a_2 in part c).

In **Exercise UCc 5** the results of phase 1 (Exercise UCc 4) and phase 2 (Exercise UCc 3) were brought together.

The level of axial stress is the changing condition between the different intervals in each calculation exercise. The increase of axial stress was simulated in smaller intermediate steps analogue to the progression of pressure in UCc-Test. The calculation was executed in six intervals as constituted in Tab. 4.16. These time steps apply for all calculations.

Tab. 4.16 Time steps of calculation at UCc-Test

Interval	Time [days]	Simulation
1	0.00 – 0.01	Axial stress increases from 0.1 MPa to 5 MPa
2	0.01 – 106.00	Axial stress of 5 MPa
3	106.00 – 106.01	Axial stress increases from 5 MPa to 10 MPa
4	106.01 – 174.00	Axial stress of 10 MPa
5	174.00 – 174.01	Axial stress increases from 10 MPa to 20 MPa
6	174.01 – 341.00	Axial stress of 20 MPa

In Exercise UCc 1 HOOKE was used for description of the material behaviour of the steel piston by simulation of the UCc-Test as in TC-Test before. In Exercise UCc 1 HOOKE and DC were used for description of the material behaviour of the salt concrete. The used constitutive laws and its parameters are shown in Tab. 4.17. This exercise aimed to check, if DC could describe the time dependent deformation behaviour of salt concrete and which pre-exponential parameters suit best. So the pre-exponential parameter was the varied value in this exercise.

Tab. 4.17 Exercise UCc 1 - Active constitutive laws for salt concrete are colored. Changed respectively varied parameters are marked red

LINEAR ELASTICITY	E [MPa]	ν [-]	ϕ_0 [-]		
		10 000	0.18	0.06	
DISLOCATION CREEP	A_A [$1/1 \cdot \text{MPa}^n$]	Q_A [J/mol]	n [-]		
	varied	54 000	5		
VISCOPLASTICITY	m [-]	A [$\text{MPa}^{-1} \cdot \text{s}$]	Q [J/mol]	a_6 [-]	W_d [-]
	-	-	-	-	-
	a_1 [-]	a_2 [-]	a_3 [-]	a_4 [-]	a_5 [-]
	-	-	-	-	-

A first calculation was executed with a pre-exponential parameter of $2.08 \cdot 10^{-6}$. This value corresponds to the creep behaviour of rock salt. Displacements were determined corresponding to Fig. 4.3 and displacements [in m] were converted in strains [in %].

In Fig. 4.12 the results of the laboratory UCc-Test are compared to the calculation results (showed in grey).

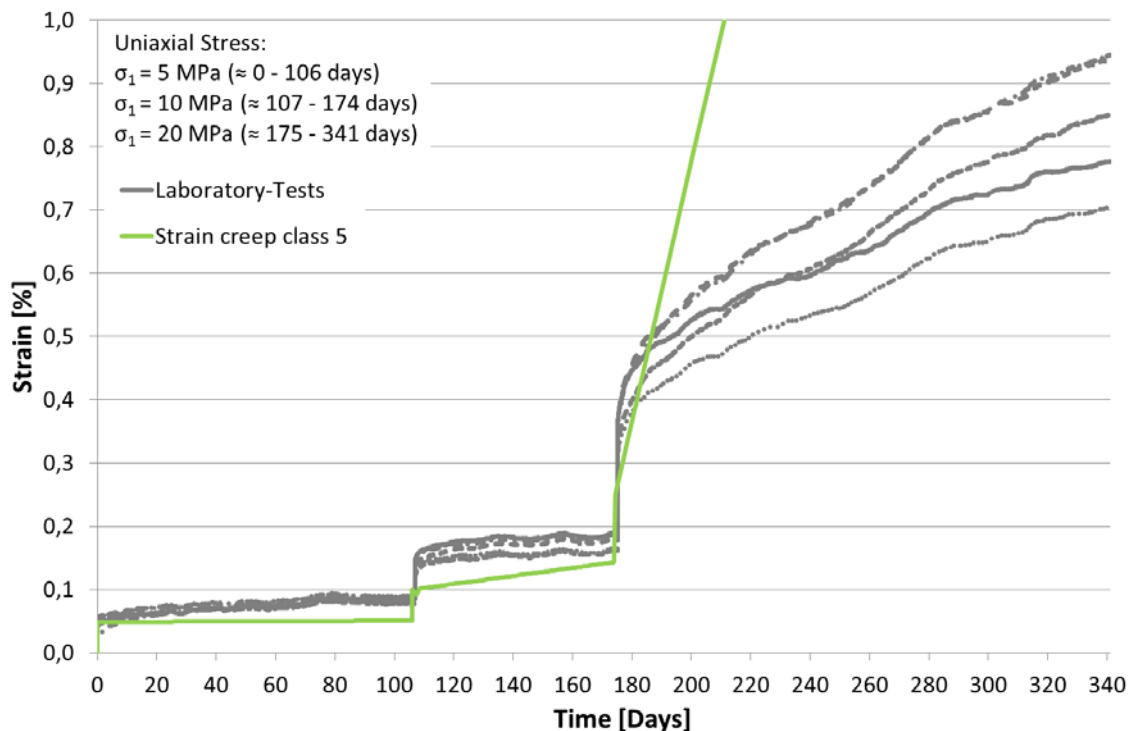


Fig. 4.12 Comparison between the results of the laboratory UCc-Test and the calculation of UCc-Test using LINEAR ELASTICITY law and DISLOCATION CREEP law by a pre-exponential parameter of $2.08 \cdot 10^{-6}$ (creep class 5)

The calculation results clearly show the different axial stress levels. Elastic deformations could be identified by sudden increase of the curve, that increased by each step. Stationary creep could be identified by the linear gradient of the curve. Certainly elastic deformations were very small in all stress levels and the deformations of stationary creep were very small in first stress level and very high for second and third stress level.

In the following, the pre-exponential parameters were varied. So the time dependent deformation behaviour corresponding to creep classes 0 to 6 was considered. The results are shown in Fig. 4.13.

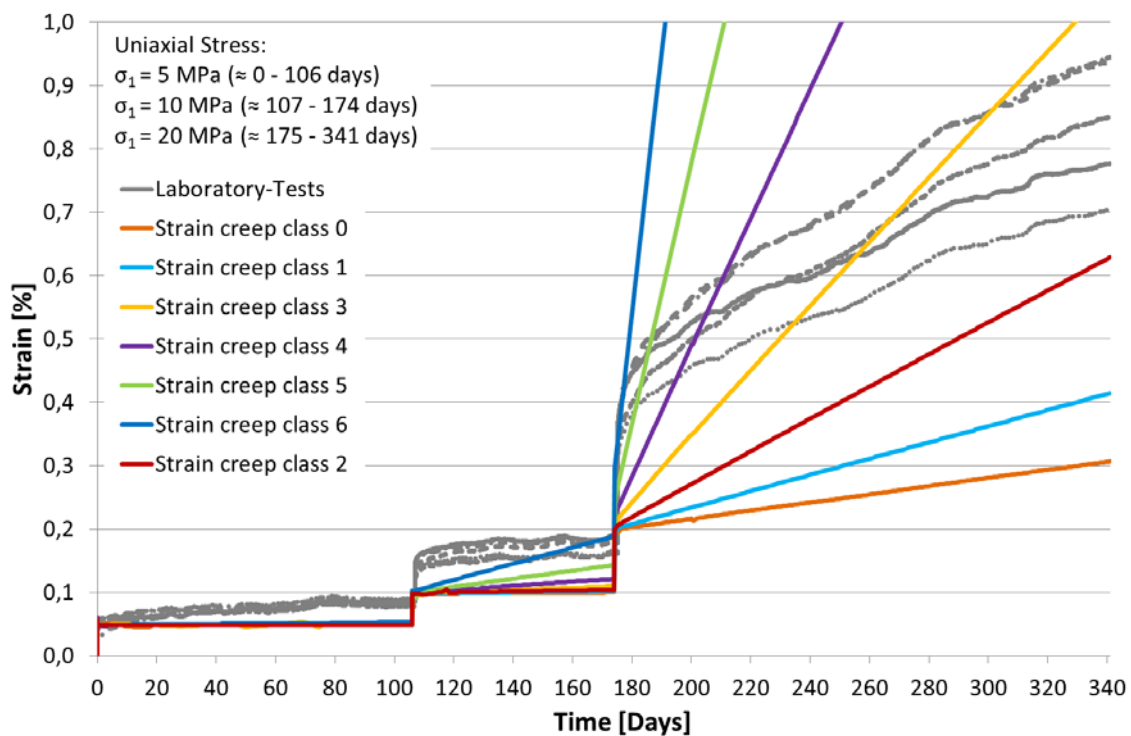


Fig. 4.13 Comparison between the results of the laboratory UCC-Test and the modelling using LINEAR ELASTICITY law and DISLOCATION CREEP with various pre-exponential parameters corresponding to creep classes 0 to 6

At the first stress level of 5 MPa all curves show nearly the same deformation behaviour. Elastic deformations could be simulated, but there were no creep deformations. Development of strains became different at the stress level of 10 MPa. Strains modelled with creep class 6 were clearly too high. Strains modelled with other creep classes could be in the right range. In order to evaluate this, a different presentation of the results is necessary (follows in Fig. 4.14 and in Fig. 4.15). When the stress level in-

creased to 20 MPa strains of each creep class became clearly different. Generally, high creep classes have higher strains than lower ones. The curve of creep class 2 with a pre-exponential parameter of $0.26 \cdot 10^{-6}$ shows the best suiting gradient compared to the gradients of the UCc-Test at first sight. Consequently, the curve of creep class 2 (brown curve) was considered more exactly.

In the following, strain rates derived from laboratory tests and from calculation will be compared. Therefore, an average value of all stationary creep levels of each specimen was constituted as shown in Fig. 4.14 (only for sample SC1048). The same was done for the calculation results. In this manner, one specific strain rate could be determined for each stress level and each specimen. The summarized results are shown in Fig. 4.15.

This simplified depiction of strain rates shows that all strain rates of the laboratory tests are in the same range for the individual stress level. The strain rates of first and second stress level are very similar while strain rates increase at third stress level. This notice supports the perception that deformation behaviour changes, if the axial stress is increased up to 20 MPa. Fig. 4.15 shows the average values of strain rates from each specimen versus the axial stress which allows a better interpretation of the results. Calculated strain rates are explicitly too small by a stress level of 5 MPa. They are around two orders of magnitude smaller than in the laboratory test. The difference is smaller at a stress level of 10 MPa, but still around one order of magnitude. Strain rates of laboratory tests accord well with the calculated strain rates in the third stress level of 20 MPa.

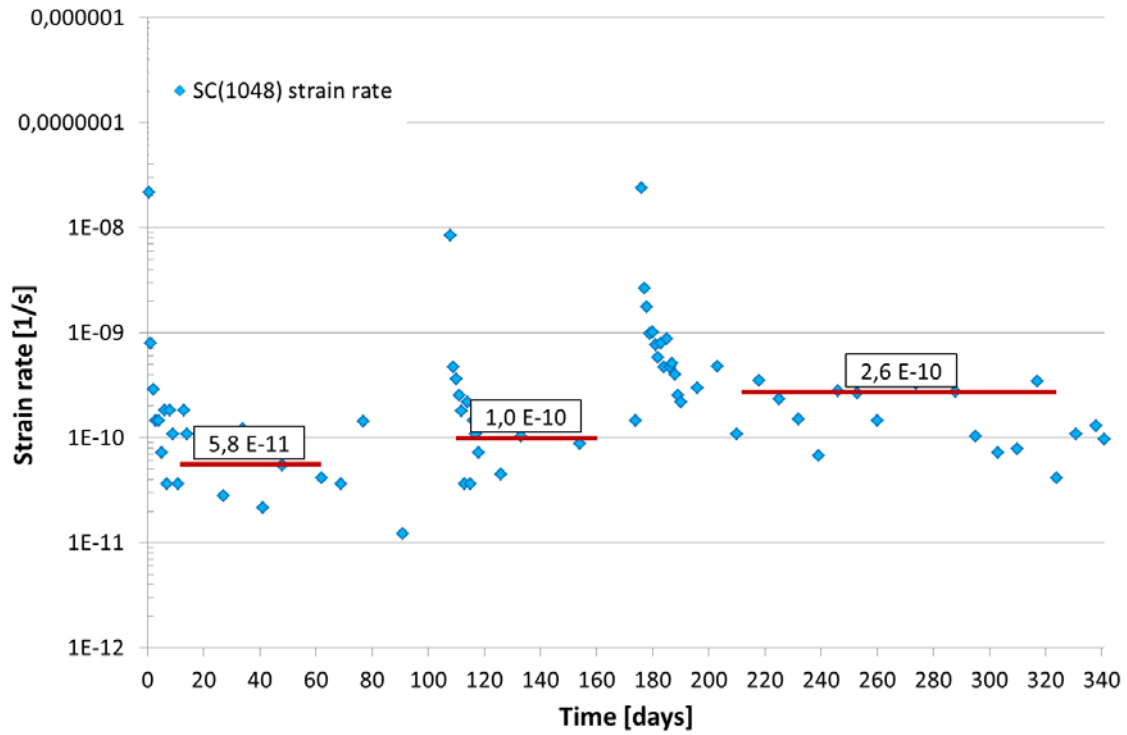


Fig. 4.14 Average determination of strain rates for specimen SC(1048)

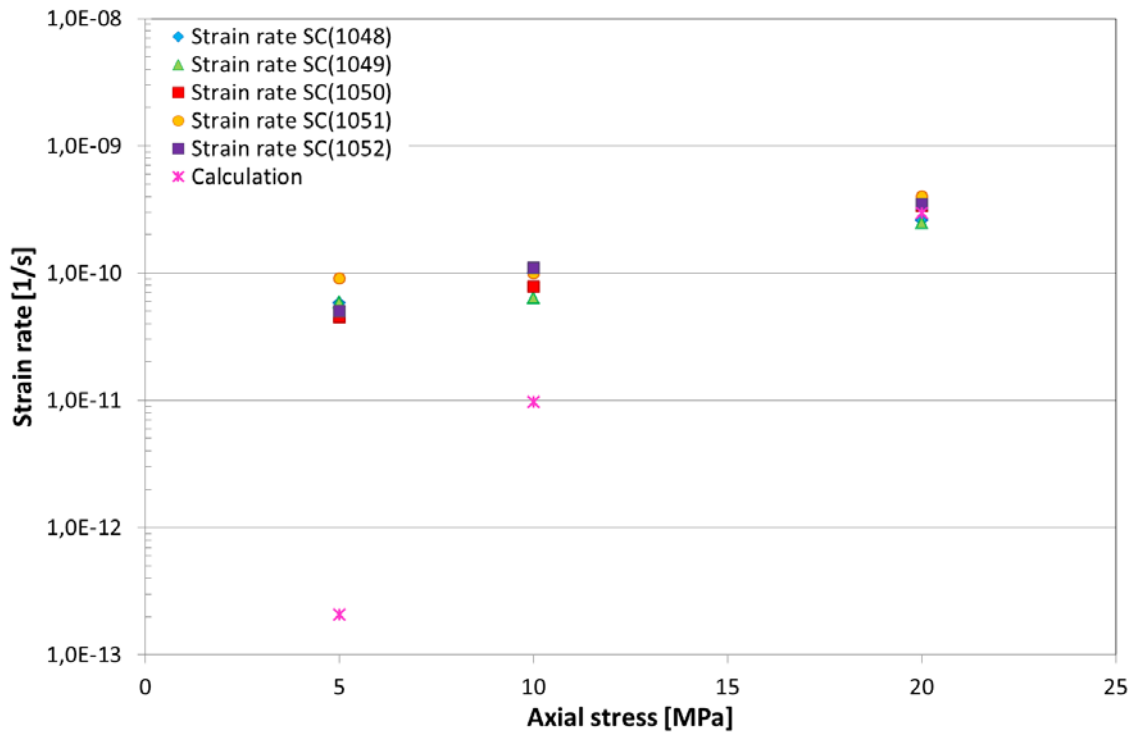


Fig. 4.15 Average strain rates of the various specimen of the laboratory UCc-Test and calculated strain rate using LINEAR ELASTICITY law and DISLOCATION CREEP with a pre-exponential parameter of $0.26e-6$ (creep class 2)

So Exercise UCc 1 shows that a calculation of the deformation behaviour of salt concrete analogue to the laboratory tests using HOOKE and DC with one pre-exponential parameter is not possible. The salt concrete shows differences in its deformation behaviour dependent on the axial stress, especially, if the axial stress increases up to 20 MPa. Additional elastic deformations were not in the right range and deformations from transient creep were not able to reproduce using HOOKE and DC.

In Exercise UCc 2 the same constitutive laws were used similarly to the exercise before. But now each stress level was considered for itself so that for each stress level an individual pre-exponential parameter was occupied. In this way, a better agreement of strain rates in the first and second stress level should be found.

Tab. 4.18 Exercise UCc 2 - Active constitutive laws for salt concrete are colored. Changed respectively varied parameters are marked red

LINEAR ELASTICITY	E [MPa]	ν [-]	ϕ_0 [-]		
	10.000	0.18	0.06		
DISLOCATION CREEP	A_A [1/1*MPaⁿ]	Q_A [J/mol]	n [-]		
	varied	54.000	5		
VISCOPLASTICITY	m [-]	A [MPa⁻¹*s]	Q [J/mol]	a_6 [-]	W_d [-]
	-	-	-	-	-
	a_1 [-]	a_2 [-]	a_3 [-]	a_4 [-]	a_5 [-]
	-	-	-	-	-

Fig. 4.16 shows the calculation results of several pre-exponential parameters from $2.08 \cdot 10^{-6}$ (corresponds to creep class 2) up to $66.56 \cdot 10^{-6}$ for the stress level of 5 MPa only. The selection of the pre-exponential parameter was geared to the end value of strain, which was reached after 106 days, if development of strains from laboratory results and calculations are compared. The pink and green curves show a good agreement to laboratory results. Because of the discontinuities in the green curve, the pink curve with a pre-exponential parameter of $40 \cdot 10^{-6}$ was chosen. The discontinuities in the beginning of the curves results probably from the process of iteration. If the iteration process starts, a balance has to be found.

In the second stress level of 10 MPa the deformations of the specimens of laboratory tests were higher, so lower pre-exponential parameters for calculation were needed in contrast to the stress level of 5 MPa (Fig. 4.17). The gradient is too small for pre-exponential parameters of $0.26 \cdot 10^{-6}$ and $0.52 \cdot 10^{-6}$ and the gradient is too big, if pre-

exponential parameters greater than $1.6 \cdot 10^{-6}$ were used. So a pre-exponential parameter of $1.04 \cdot 10^{-6}$ was chosen for stress level two.

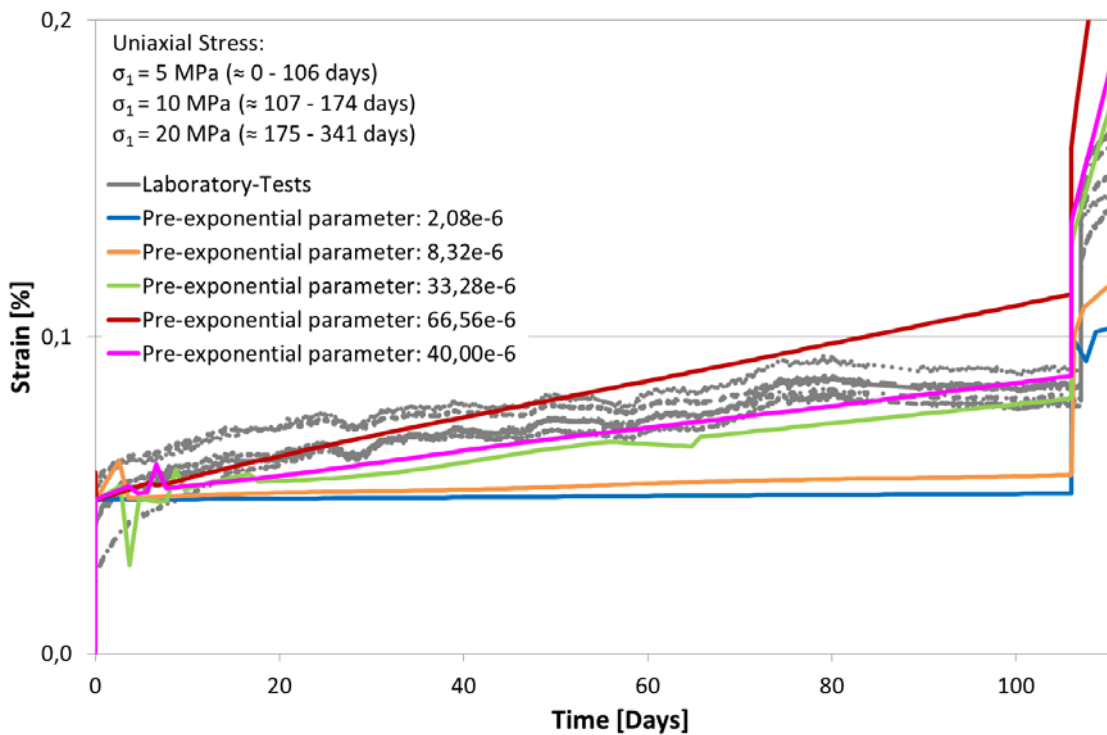


Fig. 4.16 Variation of pre-exponential parameter in first stress level of 5 MPa

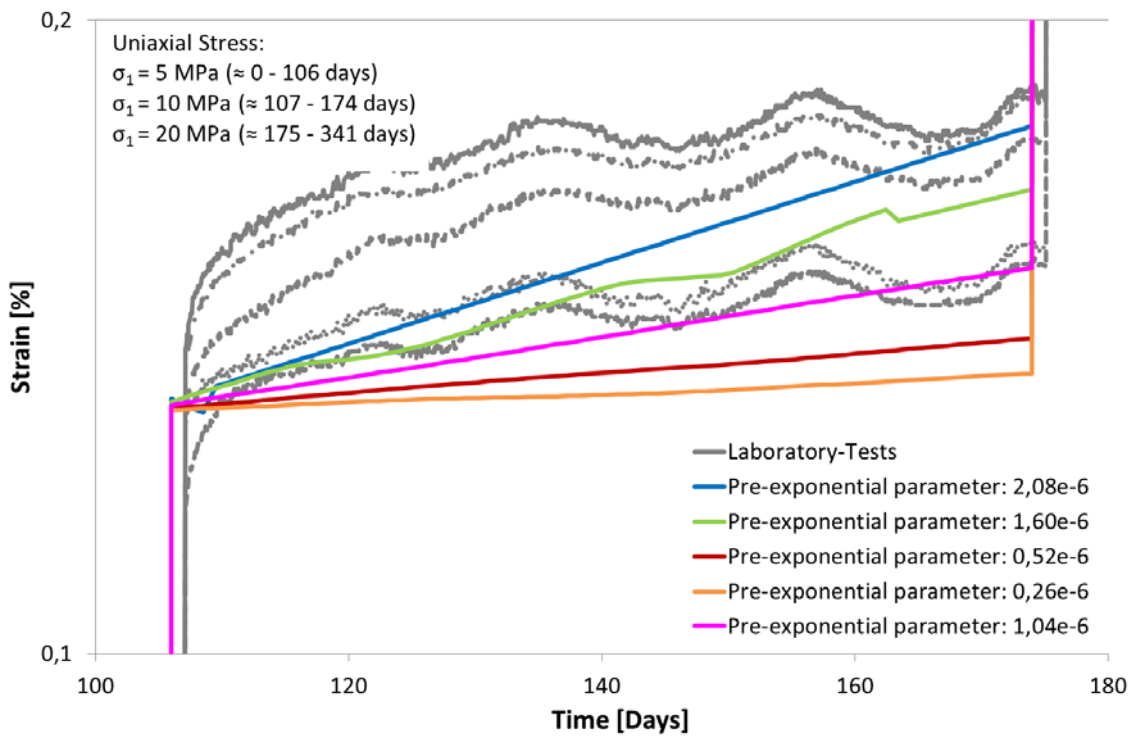


Fig. 4.17 Variation of pre-exponential parameter in second stress level of 10 MPa

The deformations increased significantly, if the axial stress reached a value of 20 MPa. Consequently, the pre-exponential parameter had to decrease. For this stress level a pre-exponential parameter of $0.2 \cdot 10^{-6}$ was chosen (Fig. 4.17), because the associated curve approximates well to the gradient of laboratory results.

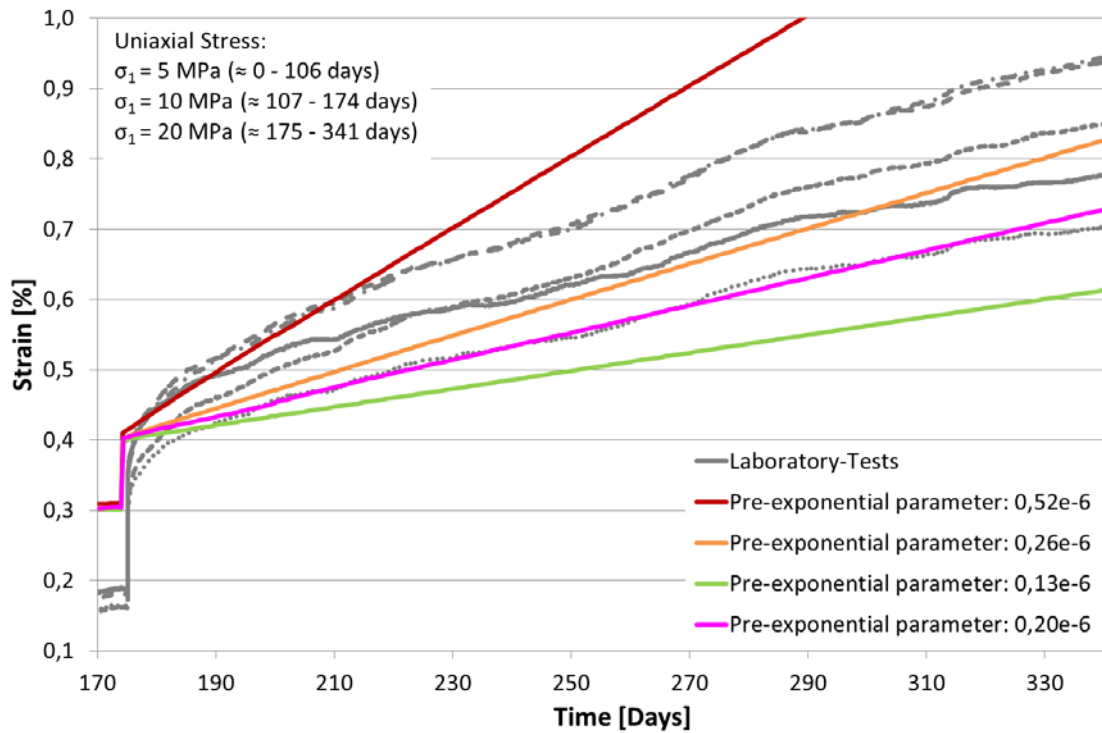


Fig. 4.18 Variation of pre-exponential parameter in third stress level of 20 MPa

After an individual pre-exponential parameter for each stress level has been found, all pre-exponential parameters were summarized in one calculation. The development of strains is shown in Fig. 4.19. Here the gradients of the curves of laboratory tests and of calculation are similar. Elastic deformations from calculation accord with laboratory test results in the first and second stress level, but are too small in the third stress level.

Strain rates are compared in Fig. 4.20. They are in the same range in each stress level for laboratory and calculation results. But in the first and second stress level, no constant strain rate was reached.

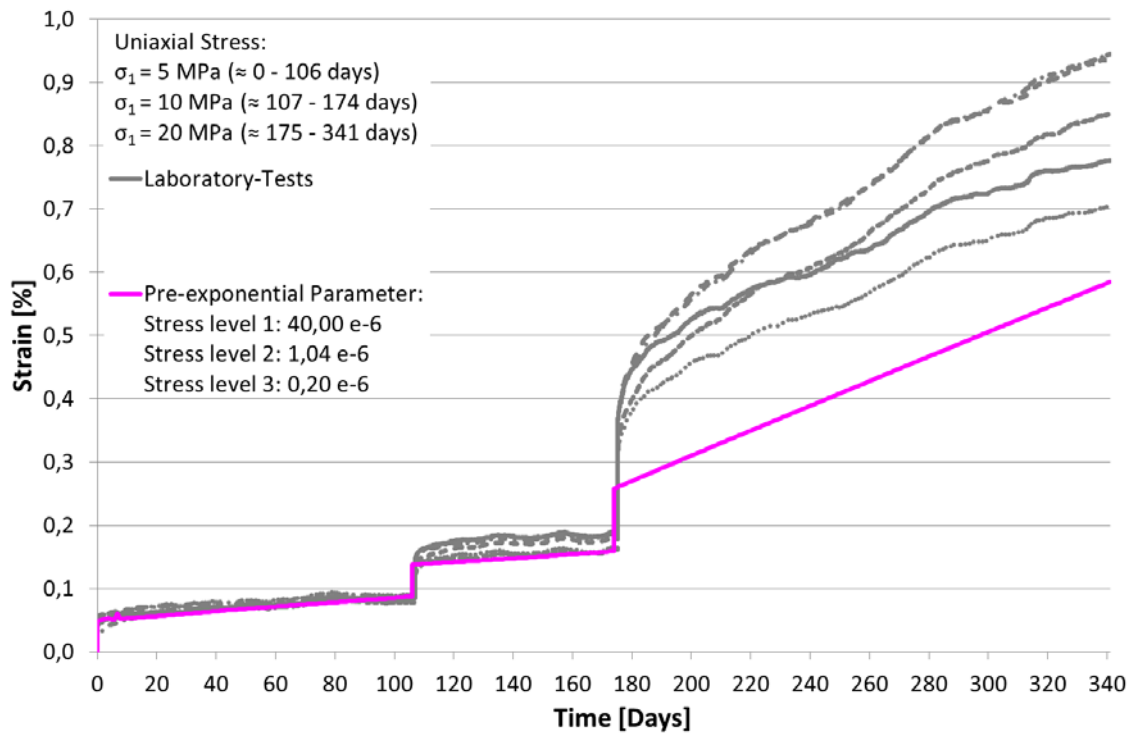


Fig. 4.19 Calculation using an individual pre-exponential parameter for each stress level

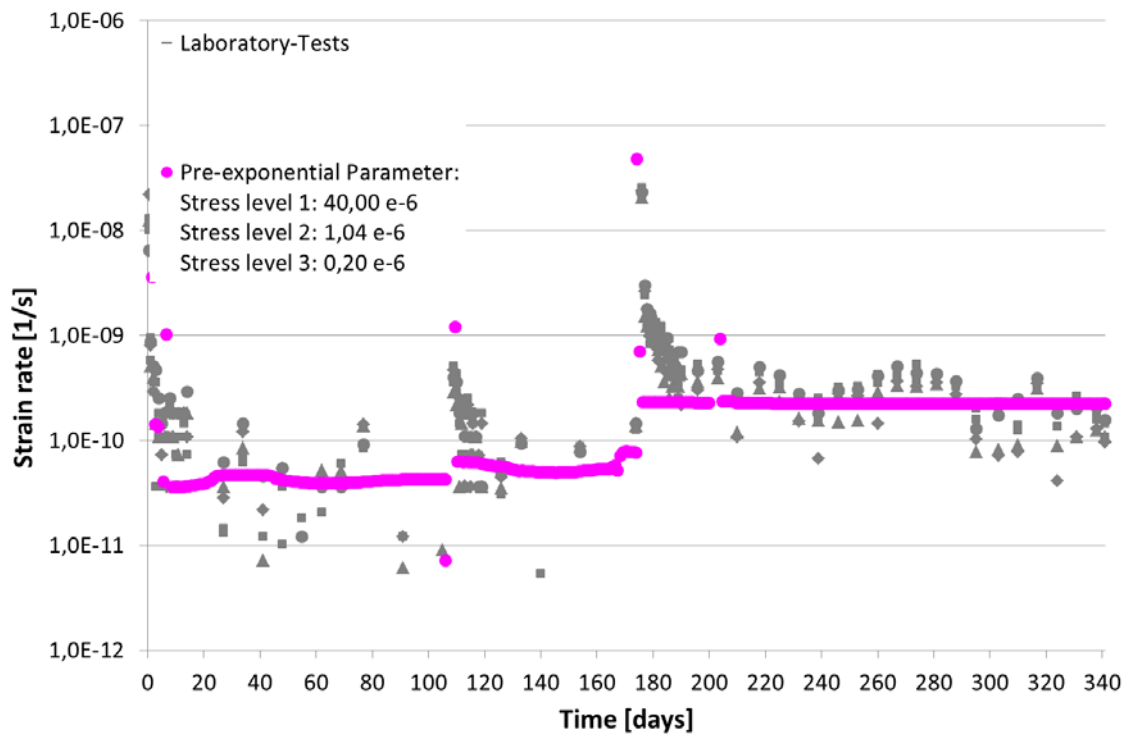


Fig. 4.20 Strain rates for calculation using different pre-exponential parameters in each stress level

Additional calculation results show, that the process of iteration was not stable for all pre-exponential parameters, when the value was between two creep classes. The green curve in Fig. 4.17 clearly shows the respective behaviour and the development of strain rates in Fig. 4.20.

Further deficit of Exercise UCc 1 and 2 is that the used constitutive laws were not able to describe transient creep and dilatancy. Therefore, no further application for approach using only HOOKE and DC by different pre-exponential parameters follows.

Finally, the comparison between laboratory and calculation results using HOOKE and DC supports the thesis from simulation of the TC-Test, that a different deformation behaviour of the salt concrete is expected, if the stress increases from 10 to 20 MPa. This perception was used for next calculations. Hence, further calculations were graduated in two phases:

- Phase 1 describes the deformation behaviour for stress levels of 5 MPa and 10 MPa and
- Phase 2 describes deformation behaviour at a stress level of 20 MPa.

The description starts with phase 2, due to the connection to the TC-Test calculation results.

Until now only HOOKE and DC were used for describing the UCc-Test. But it was not possible to describe transient creep or shear thickening deformations by using only these constitutive laws. Hence, the VP will be adapted to phase 2 in the following steps.

The VP, which was used for calculation of the TC-Test, was used in Exercise UCc 3a. The parameters were used for the first calculation, which were defined for the calculation of TC-Test. Additionally, only HOOKE was used corresponding to the Exercise TC 2. Used constitutive laws and its parameters are summarized in Tab. 4.19.

The elastic deformation at the first stress level is in the right range, but there are no viscoplastic deformations. In the second stress level elastic deformations are too small and viscoplastic deformations too high (Fig. 4.23). In the third stress level strains are clearly too high and reach values higher than 25 % (Fig. 4.21). The development of po-

rosity is able to differ between transient creep deformations and the dilatancy induced deformations.

Tab. 4.19 Exercise UCc 3a - Active constitutive laws for salt concrete are colored. Changed respectively varied parameters are marked red

LINEAR ELASTICITY	E [MPa]	ν [-]	ϕ_0 [-]		
	10 000	0.18	0.06		
DISLOCATION CREEP	A_A [1/1*MPaⁿ]	Q_A [J/mol]	n [-]		
	-	-	-		
VISCOPLASTICITY	m [-]	A [MPa⁻¹*s]	Q [J/mol]	a_6 [-]	W_d [-]
	8	$5 \cdot 10^{-9}$	54 000	0.0	3.5
	a_1 [-]	a_2 [-]	a_3 [-]	a_4 [-]	a_5 [-]
	2.05	0.0	2.5	0.0	0.02

Fig. 4.22 shows that porosity slightly decreases in the second stress level and clearly increases in the third stress level. Transient creep generated deformations in the second stress level because the decreasing porosity indicates, that the specimen was compacted.

Deformations in third stress level were generated by dilatancy, because the volume of the specimen increased. This supports the assumption of a different deformation behaviour in phase 1 and phase 2. So in further calculations only the third stress level (correspond to phase 2) was considered. Phase 1 will then be considered in the next section.

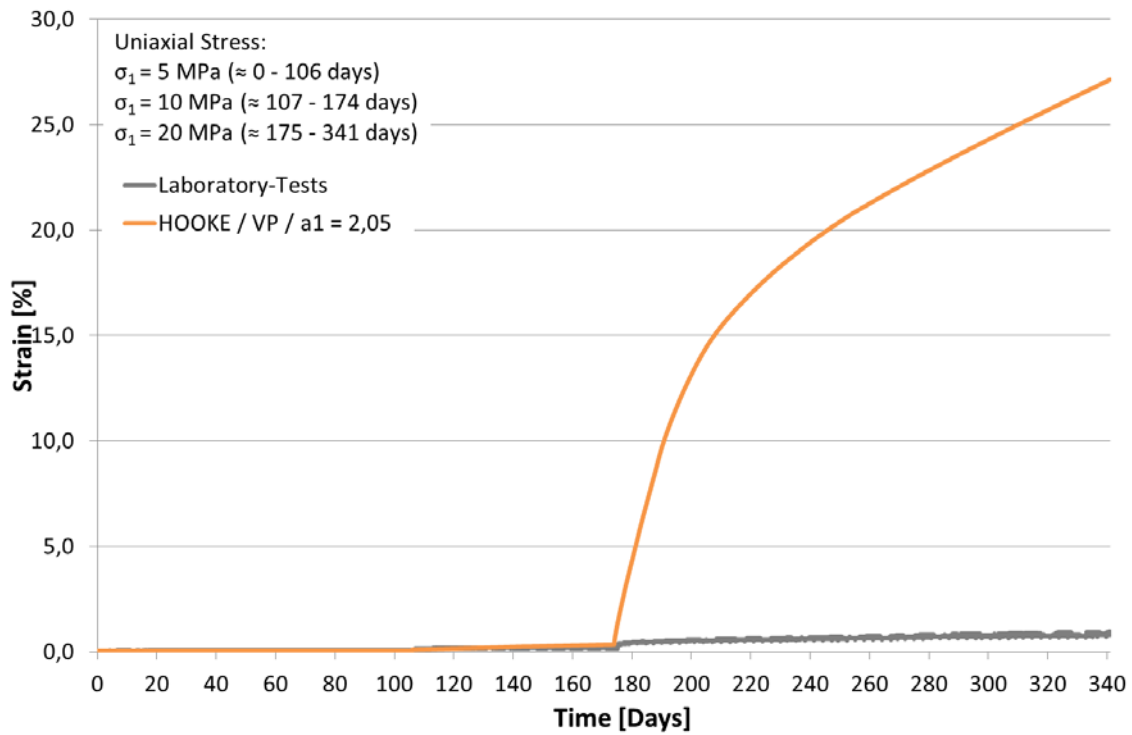


Fig. 4.21 Calculation of the UCc-Test using the LINEAR ELASTICITY law and VISCOPLASTICITY model with parameters of Exercise TC 2

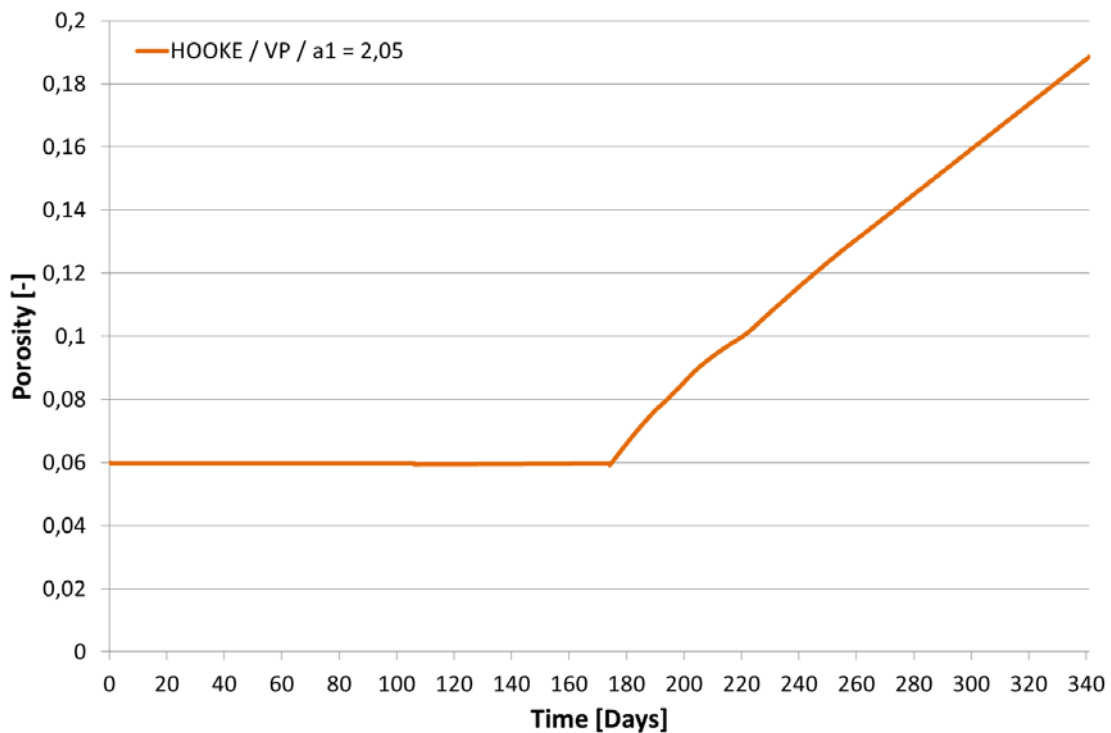


Fig. 4.22 Development of porosity using the LINEAR ELASTICITY law and VISCOPLASTICITY model with parameters of Exercise TC 2

As the parameters analogue to TC-Test were not suitable for simulating the UCc-Test, the parameter a_1 for the stability of the material and a_2 , a_4 and a_6 for the limiting of volumetric strain were varied in Exercise UCc 3b.

Tab. 4.20 Exercise UCc 3b - Active constitutive laws for salt concrete are colored. Changed respectively varied parameters are marked red

LINEAR ELASTICITY	E [MPa]	ν [-]	ϕ_0 [-]		
		10 000	0.18	0.06	
DISLOCATION CREEP	A_A [1/1*MPa ⁿ]	Q_A [J/mol]	n [-]		
	-	-	-		
VISCOPLASTICITY	m [-]	A [MPa ⁻¹ *s]	Q [J/mol]	a_6 [-]	W_d [-]
	8	$5 \cdot 10^{-9}$	54 000	0.02	3.5
	a_1 [-]	a_2 [-]	a_3 [-]	a_4 [-]	a_5 [-]
	varied	1.8	2.5	0.7	0.02

At first volumetric deformations were limited again. Values of parameter a_2 , a_4 and a_6 were used corresponding to Tab. 4.13. Deformations became smaller in this way, but especially in the third stress level they were still too big (Fig. 4.23, purple curve). The porosity increased around 1 % in the third stress level (Fig. 4.24).

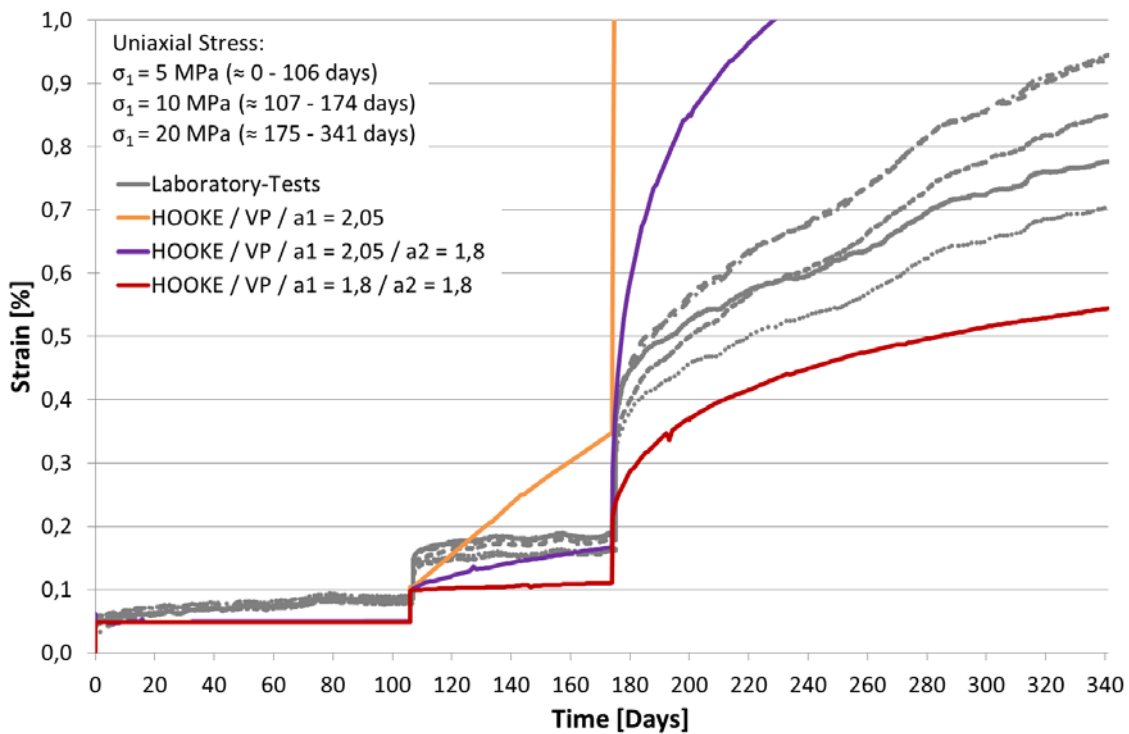


Fig. 4.23 Exercise UCc 3a-b - Variation of parameter a_1 and a_2 plus variation of the pre-exponential parameter (PP)

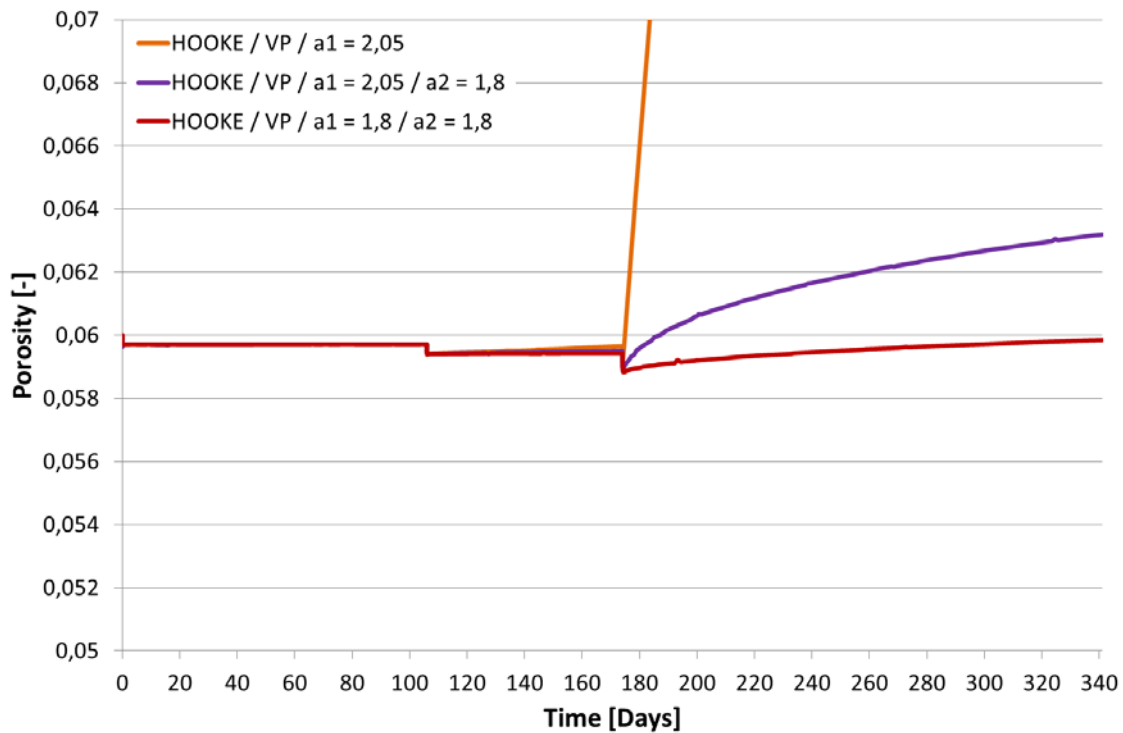


Fig. 4.24 Exercises UCc 3a-b - Development of porosity for calculations in phase 2

It was expected, that during calculation dilatancy was still too high by an axial stress of 20 MPa with respect to the laboratory results. Hence, dilatancy was limited using a_1 equal to 1.8. Now deformations in third stress level became smaller (red curve in Fig. 4.25) and were located below the deformations of the laboratory test. The increase of porosity was clearly smaller now, see Fig. 4.26. Corresponding to laboratory results a combination of viscoplastic deformations and stationary creep is expected by an axial stress level of 20 MPa. Hence, in Exercise UCc 3c stationary creep was considered by DC using the pre-exponential parameter of $0.2 \cdot 10^{-6}$ analogue to the individual adaptation in third stress level in Exercise UCc 2.

Tab. 4.21 Exercise UCc 3c - Active constitutive laws for salt concrete are colored. Changed respectively varied parameters are marked red

LINEAR ELASTICITY	E [MPa]	ν [-]	ϕ_0 [-]		
	10 000	0.18	0.06		
DISLOCATION CREEP	A_A [1/1*MPa ⁿ]	Q_A [J/mol]	n [-]		
	varied	54 000	5		
VISCOPLASTICITY	m [-]	A [MPa ⁻¹ *s]	Q [J/mol]	a_6 [-]	W_d [-]
	8	$5 \cdot 10^{-9}$	54 000	0.02	3.5
	a_1 [-]	a_2 [-]	a_3 [-]	a_4 [-]	a_5 [-]
	1.8	1.8	2.5	0.7	0.02

Now the gradient of the curve was too steep (Fig. 4.25, blue curve). The difference of the gradient between this calculation and Exercise UCc 2 could result from the additional viscoplastic deformations here. This means, that by using DC and VP for calculation a smaller pre-exponential parameter has to be used. Below a pre-exponential parameter equal to $0.065 \cdot 10^{-6}$ was used.

The green curve shows a good agreement to laboratory test in curvature and gradient in the lower sector of laboratory tests (Fig. 4.25). Additionally, the porosity increased in the third stress level (Fig. 4.26), which supports, that the onset of dilatancy occurred first by an axial stress of 20 MPa.

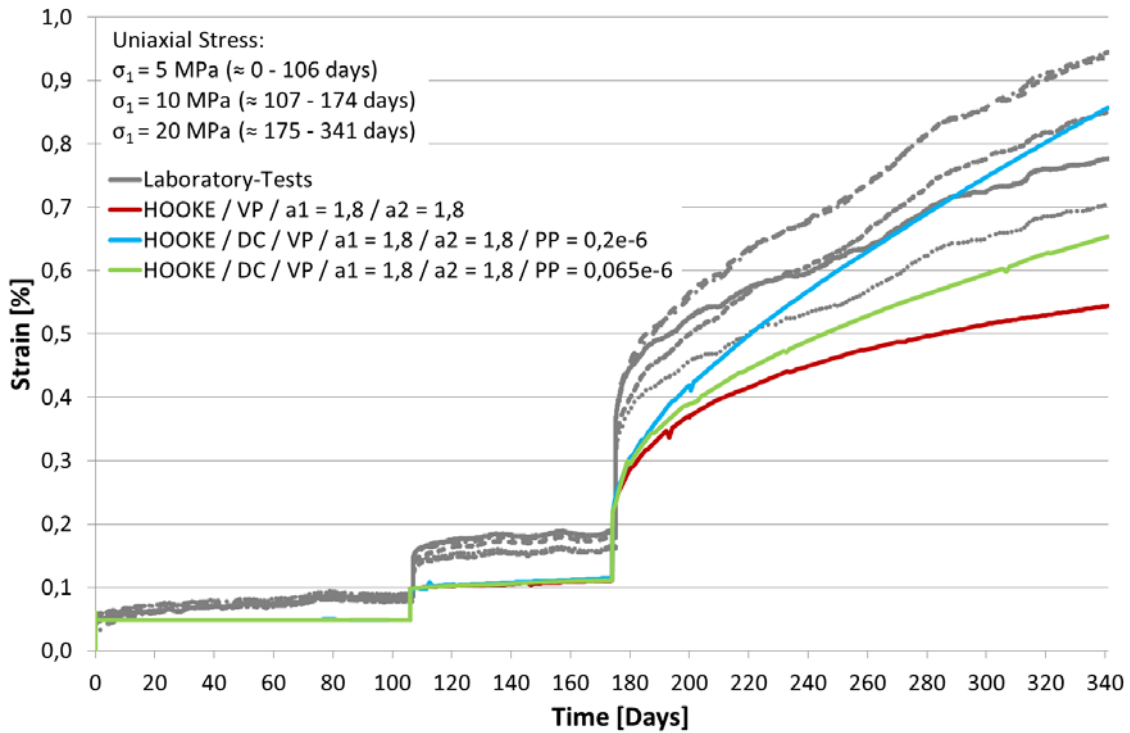


Fig. 4.25 Exercise UCc 3c - Variation of parameter a_1 and a_2 plus variation of the pre-exponential parameter (PP) by using LINEAR ELASTIC LAW, DISLOCATION CREEP law and VISCOPLASTICITY model

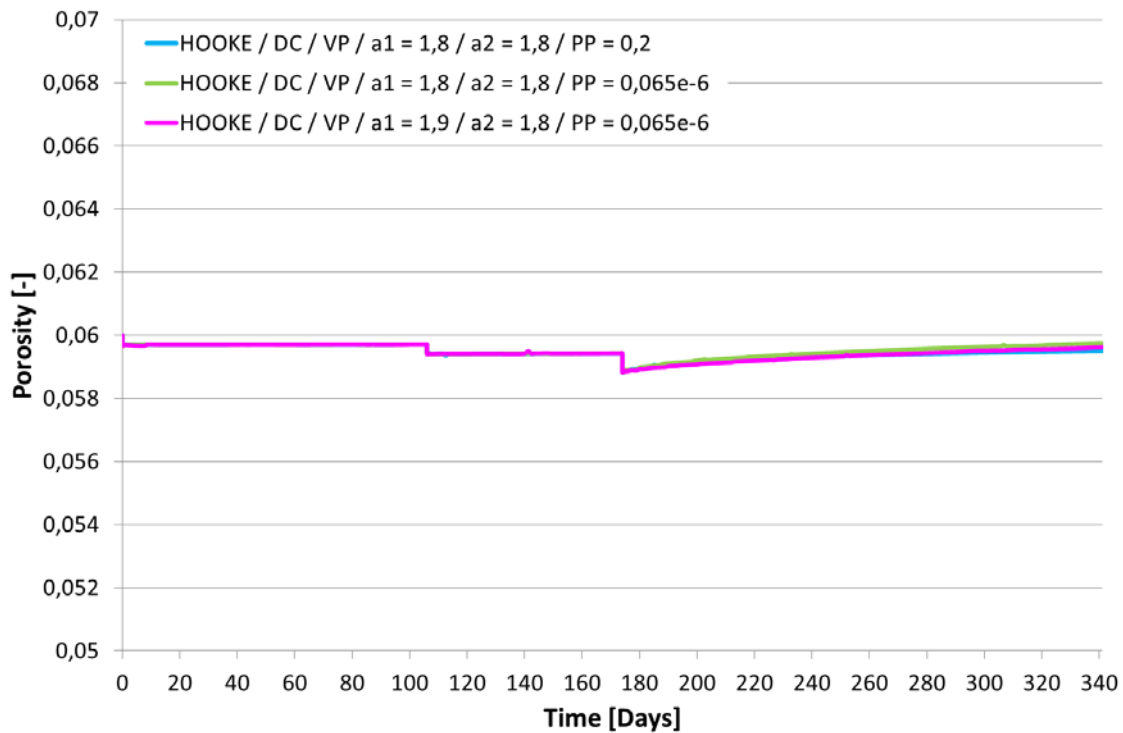


Fig. 4.26 Exercises UCc 3c-d - Development of porosity for calculations in phase 2

Probably, volumetric deformation could be higher against the result of the parameter combination from Exercise UCc 3c (green curve). Hence, parameter a_1 was increased to 1.85 and 1.9 in the following Exercise UCc 3d.

Tab. 4.22 Exercise UCc 3d - Active constitutive laws for salt concrete are colored. Changed respectively varied parameters are marked red

LINEAR ELASTICITY	E [MPa]	ν [-]	ϕ_0 [-]		
	10 000	0.18	0.06		
DISLOCATION CREEP	A_A [1/1*MPaⁿ]	Q_A [J/mol]	n [-]		
	0.065e ⁻⁶	54 000	5		
VISCOPLASTICITY	m [-]	A [MPa⁻¹*s]	Q [J/mol]	a_6 [-]	W_d [-]
	8	5*10 ⁻⁹	54 .000	0.02	3.5
	a_1 [-]	a_2 [-]	a_3 [-]	a_4 [-]	a_5 [-]
	varied	1.8	2.5	0.7	0.02

Calculation results show that deformations increase using higher values of a_1 . The sector of laboratory results is well covered by using a_1 from 1.8 up to 1.9. The curve for a_1 equal to 1.8 is located in the lower sector and for a_1 equal to 1.9 in the upper sector. The results are showed in Fig. 4.27.

Additionally, strain rates reached a similar range than in the laboratory tests (Fig. 4.28). The nomenclature of the strain rates results from the discontinuities, which are shown in the development of strains in Fig. 4.27. For an exponential smoothing of the curves an adaptation of the iteration steps is necessary. This adaptation will follow in the end of UCc-Test simulation, because the development of strain and strains rates was only considered quantitatively here (not shown in the figures).

The development of porosity shows for all calculations that the porosity increases in third stress level. So there is an interaction of elastic deformations, transient and stationary creep and dilatancy. This correlates to assumptions from laboratory tests.

The finally used parameters for calculation of UCc-Test in the third stress level are summarized in Tab. 4.26 at the end of the chapter.

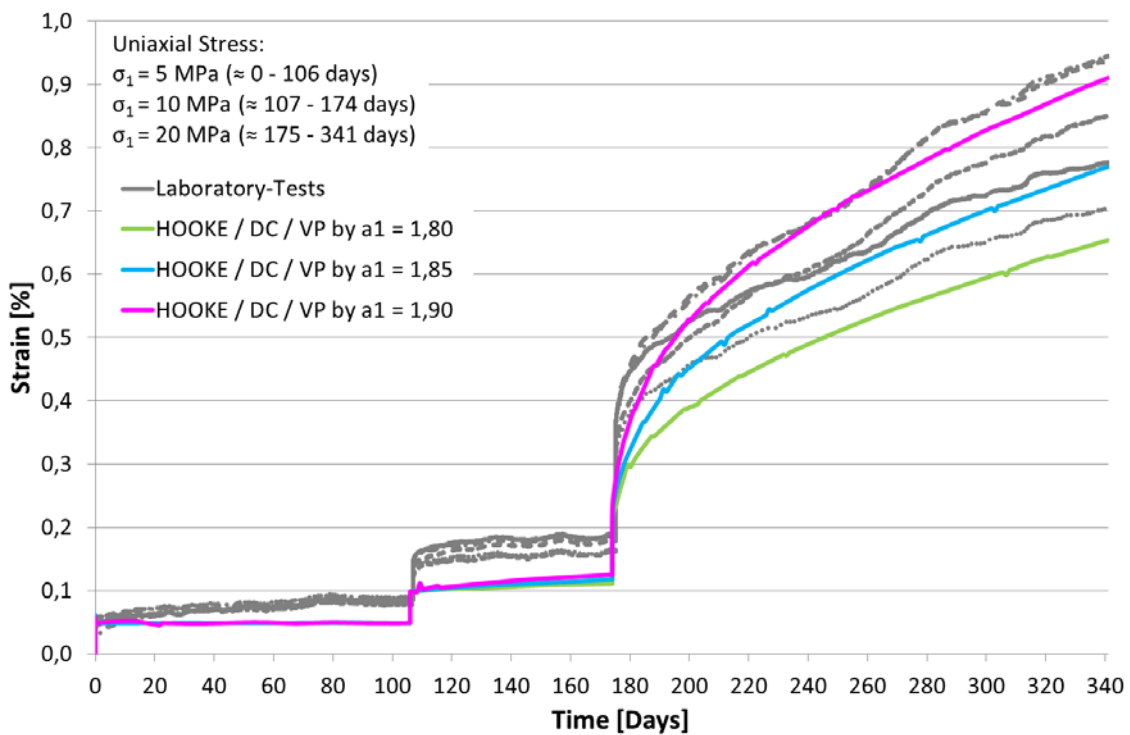


Fig. 4.27 Depiction of the deformation behaviour by considering LINEAR ELASTICITY LAW, DISLOCATION CREEP law and VISCOPLASTICITY model after Exercise UCc 3d

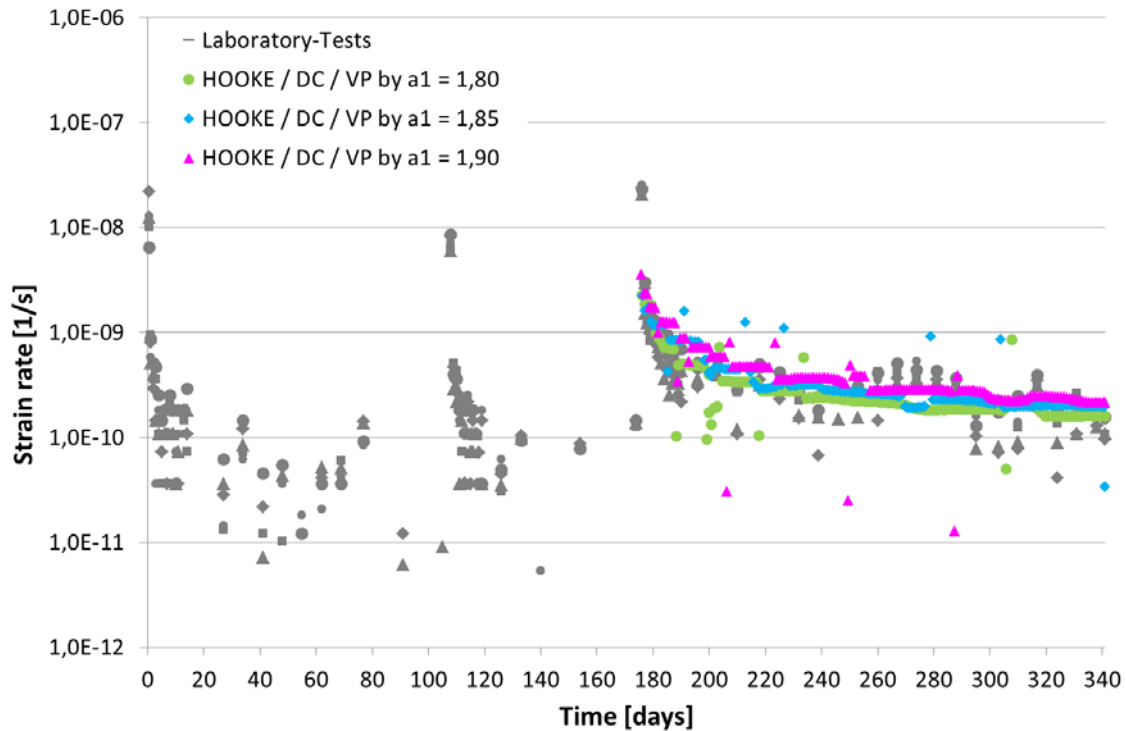


Fig. 4.28 Strains rates in third stress level using parameters of Exercise UCc 3d

Now the parameters of VP were adapted to the first and second stress level. Laboratory tests showed that in this phase transient creep is expected. But with using parameters corresponding to Exercise UCc 3, a transient creep behaviour could not be reproduced in phase 1. Therefore, the influence of three parameters – viscosity, material stability and volumetric extension – on transient creep behaviour was investigated.

In Exercise UCc 4a the influence of viscosity A on transient creep was investigated. The pre-exponential parameter was equal to $0.2 \cdot 10^{-6}$, corresponding to the results of Exercise UCc 2. It was chosen from the third stress level, because investigations before have showed, that only in phase 2 stationary creep can be expected. Deformations in phase 1 occurred probably by elastic deformations and transient creep, so that the pre-exponential parameter has no influence on the evolution of deformations in phase 1. Additionally, a_1 was set to 1.33 as in Exercise TC 2 because onset of dilatancy should be excluded.

Viscosity was set to $5.0 \cdot 10^{-9}$ 1/s in first calculations corresponding to /WIE 10/. The results in Fig. 4.29 show, that only elastic deformations and stationary creep in the third stress level occur (orange curve). This means, that the chosen viscosity is too high for simulating transient creep deformations. Fig. 4.30 shows the development of porosity.

Porosity decreases at each increase of stress for this calculation, so that no onset of dilatancy occurred.

Tab. 4.23 Exercise UCc 4a - Active constitutive laws for salt concrete are colored. Changed respectively varied parameters are marked red.

LINEAR ELASTICITY	E [MPa]	ν [-]	ϕ_0 [-]		
	10 000	0.18	0.06		
DISLOCATION CREEP	A_A [$1/1 \cdot \text{MPa}^n$]	Q_A [J/mol]	n [-]		
	$0.2 \cdot 10^{-6}$	54 000	5		
VISCOPLASTICITY	m [-]	A [$\text{MPa}^{-1} \cdot \text{s}$]	Q [J/mol]	a_6 [-]	W_d [-]
	8	varied	54 000	0.02	3.5
	a_1 [-]	a_2 [-]	a_3 [-]	a_4 [-]	a_5 [-]
	1.33	1.8	2.5	0.7	0.02

Viscosity was increased for next calculation to $5.0 \cdot 10^{-1}$ 1/s and thus deformations increased clearly. The blue curve shows deformations similar to transient creep in all stress levels, but deformations were clearly too high. The porosity increases at second stress level. Hence, transient creep and dilatancy deformation occur, when viscosity is increased.

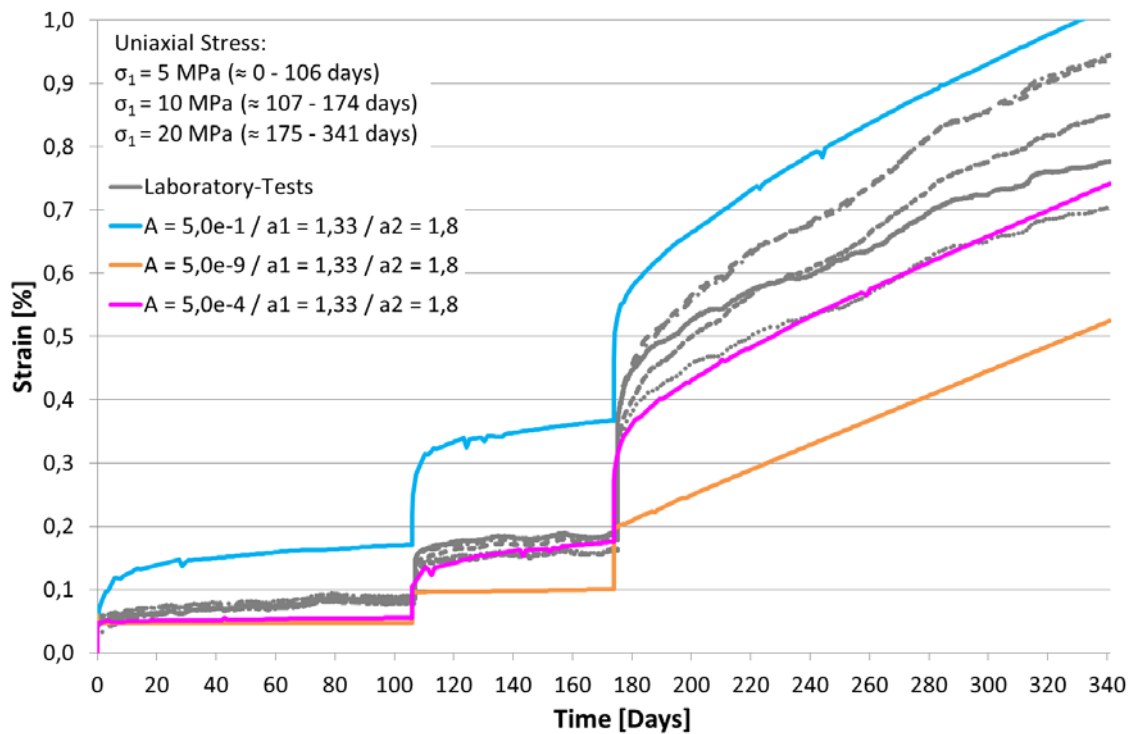


Fig. 4.29 Exercise UCc 4a - Variation of viscosity (A)

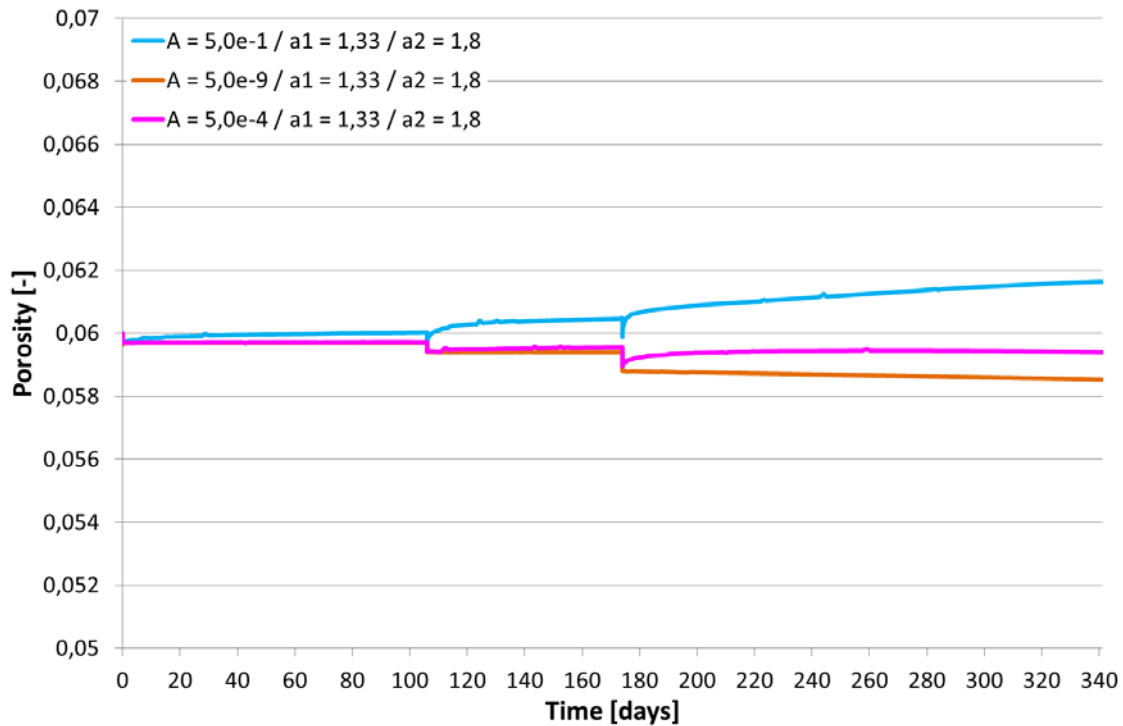


Fig. 4.30 Exercise UCc 4a - Development of porosity by varying viscosity (A)

Hence, viscosity was decreased again to $5 \cdot 10^{-4}$ 1/s. The results show, that transient creep occurred in second stress level, but not in the first one. Porosity increased rarely in second stress level. Elastic deformations are similar to the elastic deformations of laboratory tests. So a viscosity of $5 \cdot 10^{-4}$ 1/s was chosen for the next calculations. A better adaptation should be found by variation of parameters for stability of the material and volumetric strains in following exercises.

The peaks in the blue and pink curves could occur because the process of iteration was not stable at that point. An adaptation of the steps of iteration would be necessary. But the considerations were only quantitative here and the results are not final. So an adaptation of iteration steps follows later only for the final results.

In Exercise UCc 4b parameters were used corresponding to Exercise UCc 4a. But a_1 was increased for a better adaptation of the deformations from transient creep. By increasing a_1 the material stiffness decreased and allowed creep deformations at smaller stress levels.

Tab. 4.24 Exercise UCc 4b - Active constitutive laws for salt concrete are colored. Changed respectively varied parameters are marked red

LINEAR ELASTICITY	E [MPa]	ν [-]	ϕ_0 [-]		
		10 000	0.18	0.06	
DISLOCATION CREEP	A_A [1/1*MPa ⁿ]	Q_A [J/mol]	n [-]		
	0.2e ⁻⁶	54 000	5		
VISCOPLASTICITY	m [-]	A [MPa ⁻¹ *s]	Q [J/mol]	a_6 [-]	W_d [-]
	8	5·10 ⁻⁴	54 000	0.02	3.5
	a_1 [-]	a_2 [-]	a_3 [-]	a_4 [-]	a_5 [-]
	varied	1.8	2.5	0.7	0.02

Results are shown in Fig. 4.31 and the development of porosity in Fig. 4.32. The pink curve shows the calculation result from Exercise UCc 4a using a_1 equal to 1.33. Next calculation was executed using a_1 equal to 1.6 (brown curve). If the material becomes less stiff, deformations increase. But now strains were clearly too high in all stress levels. Consideration of development of porosity shows, that additionally to transient creep shear thickening deformations developed.

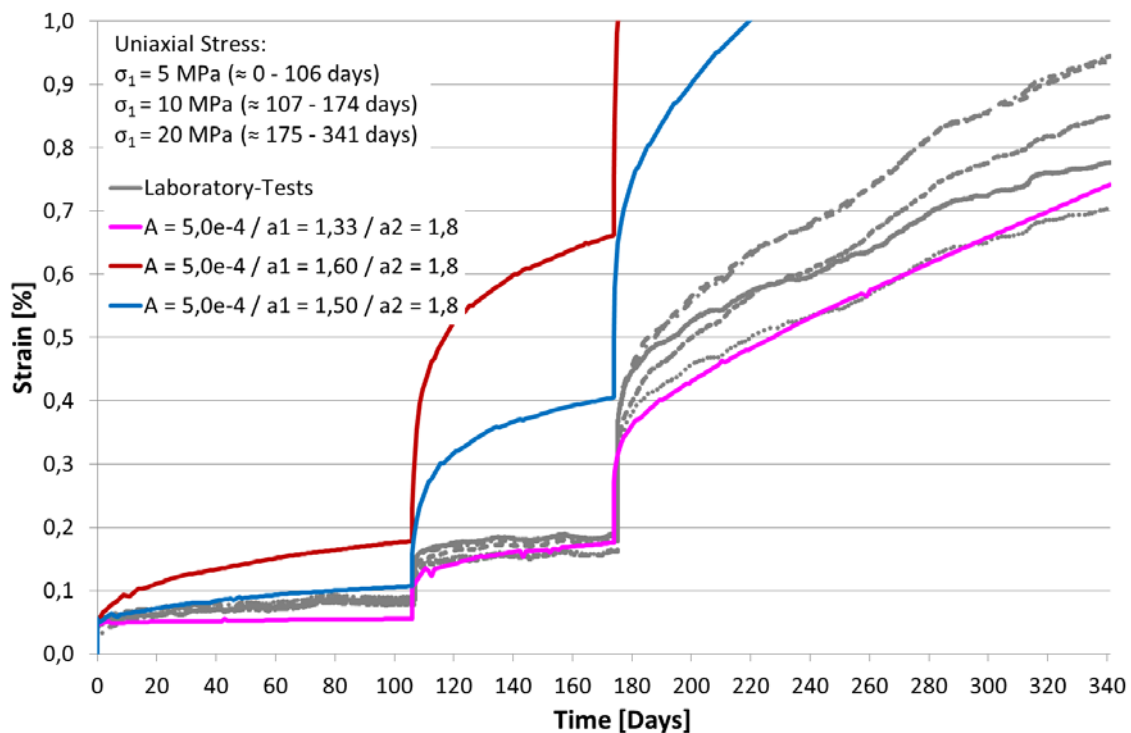


Fig. 4.31 Exercise UCc 4b - Variation of parameter a_1

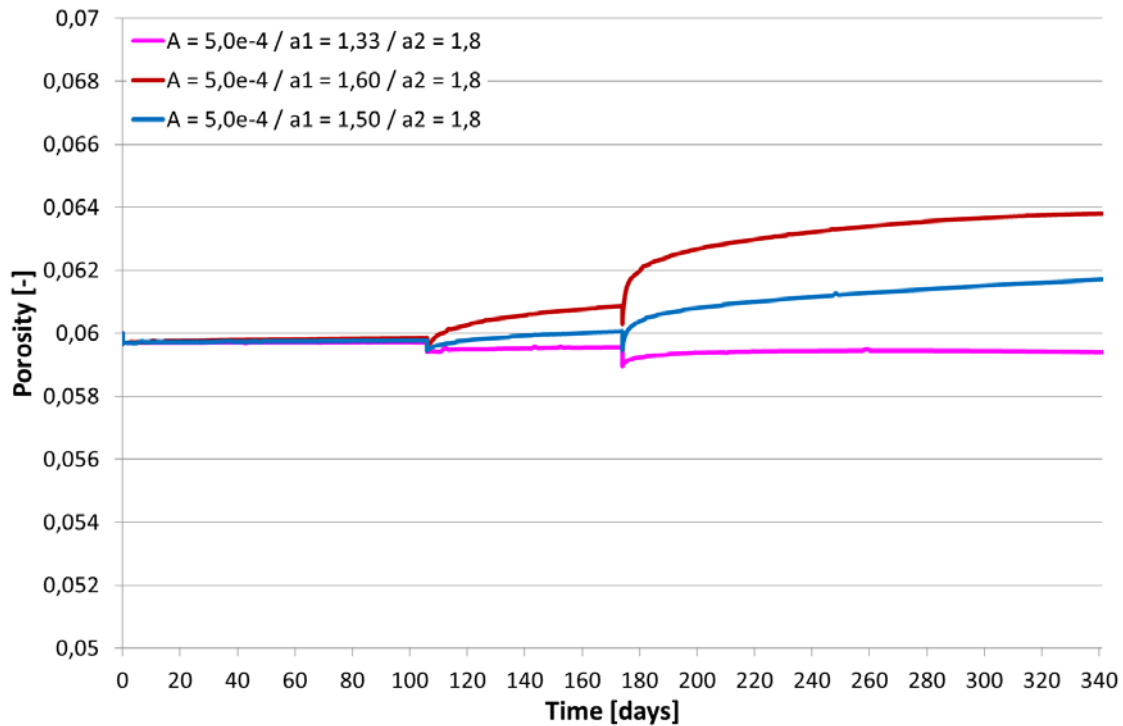


Fig. 4.32 Exercise UCc 4b - Development of porosity

Hence, an a_1 equal to 1.5 was used (blue curve). The development of strains in the first stress level, especially the curvature in the curve, which describes the transient creep, could be described. Strains in the second stress level were too high, additionally the porosity increased. So there are shear thickening deformations, too.

In Exercise UCc 4c volumetric strains have to be limited because strains were still too high and porosity increased in second stress level. Hence, a_2 was varied for limiting the volumetric extension.

Tab. 4.25 Exercise UCc 4c - Active constitutive laws for salt concrete are colored. Changed respectively varied parameters are marked red

LINEAR ELASTICITY	E [MPa]	ν [-]	ϕ_0 [-]		
	10 000	0.18	0.06		
DISLOCATION CREEP	A_A [1/1*MPaⁿ]	Q_A [J/mol]	n [-]		
	$0.2 \cdot 10^{-6}$	54 000	5		
VISCOPLASTICITY	m [-]	A [MPa⁻¹*s]	Q [J/mol]	a_6 [-]	W_d [-]
	8	$5 \cdot 10^{-4}$	54 000	0.02	3.5
	a_1 [-]	a_2 [-]	a_3 [-]	a_4 [-]	a_5 [-]
	1.5	varied	2.5	0.7	0.02

As before, the blue curve in Fig. 4.33 shows calculation results equivalent to Exercise UCc 4b. Below the volumetric strains were limited by increasing a_2 . If a_2 equal to 2.5

was used, strains were similar to laboratory results in first stress level (violet curve). But strains are still too high in the second stress level. So a_2 was increased to 3.0 (green curve). Now the development of strains in the first and second stress level is similar to laboratory results.

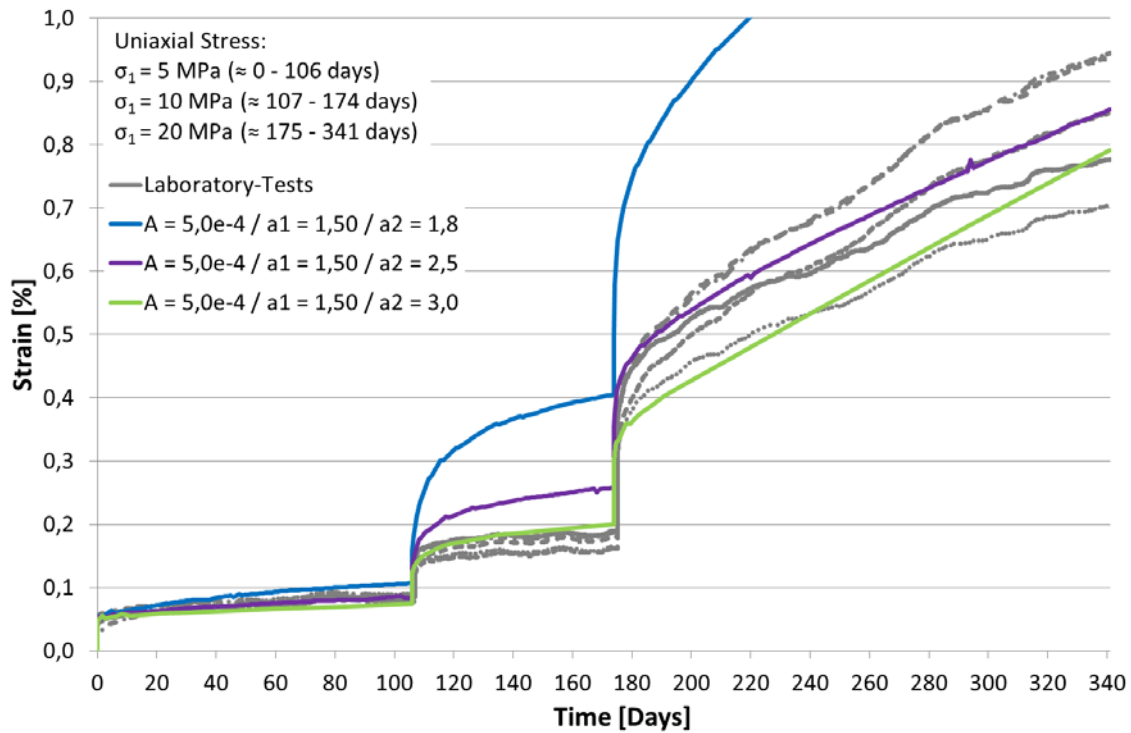


Fig. 4.33 Exercise UCc 4c - Variation of parameter a_2

Additionally, porosity did not increase in the first level and increased marginally in the second stress level (Fig. 4.34). So the part of shear thickening deformations is very small in phase 1 and is in an acceptable range for numerical calculations. In consideration of phase 2 it can be seen, that elastic deformations, transient and stationary creep as soon as dilatancy are in a similar range as in laboratory results. Porosity increased in the beginning of the third stress level, but decreased from 200 days again. So shear thickening deformations are also very small in this phase.

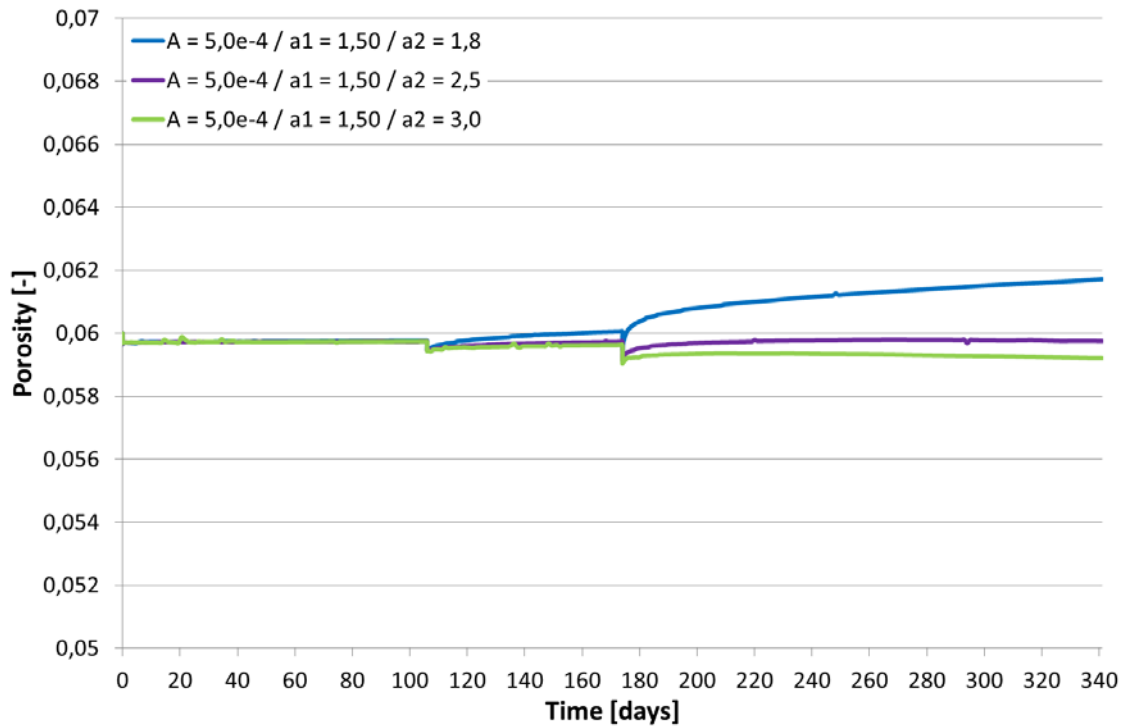


Fig. 4.34 Exercise UCc 4c - Development of porosity

In the sections before parameters for an adaptation in phase 1 and phase 2 were found. But the investigations showed that there was no combination of parameters, which were able to describe the behaviour at all stress levels.

Hence, the parameters of phase 1 and phase 2 were combined in this Exercise UCc 5. In the first and second stress level, parameters of phase 1 were used. In the third stress level, parameters of phase 2 were used. Tab. 4.26 summarizes all constitutive laws and used parameters of phase 1 and phase 2.

Tab. 4.26 Exercise UCc 5 - Active constitutive laws for salt concrete are colored. Changed respectively varied parameters are marked red

LINEAR ELASTICITY (Phase 1 / 2)	E [MPa]	ν [-]	ϕ_0 [-]		
	10 000	0.18	0.06		
DISLOCATION CREEP (Phase 1)	A_A [1/1*MPaⁿ]	Q_A [J/mol]	n [-]		
	0.2·10 ⁻⁶	54 000	5		
DISLOCATION CREEP (Phase 2)	A_A [1/1*MPaⁿ]	Q_A [J/mol]	n [-]		
	0.065·10 ⁻⁶	54.000	5		
VISCOPLASTICITY (Phase 1)	m [-]	A [MPa⁻¹*s]	Q [J/mol]	a_6 [-]	W_d [-]
	8	5·10 ⁻⁴	54 000	0.02	3.5
	a_1 [-]	a_2 [-]	a_3 [-]	a_4 [-]	a_5 [-]
	1.5	3.0	2.5	0.7	0.02
VISCOPLASTICITY (Phase 2)	m [-]	A [MPa⁻¹*s]	Q [J/mol]	a_6 [-]	W_d [-]
	8	5·10 ⁻⁹	54 000	0.02	3.5
	a_1 [-]	a_2 [-]	a_3 [-]	a_4 [-]	a_5 [-]
	1.9	1.8	2.5	0.7	0.02

The result of the combined constitutive laws is shown by the pink curve in Fig. 4.35. Its development corresponds well to the development of strains of the laboratory test. Probably strain rates could be a little bit too small in the first stress level and a little bit too high in the second stress level.

Additionally, the individual deformation components are shown in Fig. 4.35. If the calculation was executed only by HOOKE, there are only elastic deformations at the moment of increasing axial stress and no further deformations until the next increase of axial stress followed. Below HOOKE was combined with transient creep by using VP with parameters analogue to phase 1. Now there are transient creep deformations in all stress levels. Strains increase fastly in the beginning after increasing axial stress. Strain rates decrease gradually and consequently strains increase less with further interval to load increase. This phenomenon can be seen clearly in phase 2.

In the next step DC was used additionally to HOOKE and VP. The development in phase 1 is nearly identical to the calculation before. Stationary creep is of less importance in stress levels up to 10 MPa. In the third stress level stationary creep becomes relevant. The curve increases and strains increase constantly. This corresponds to the assumptions from laboratory results.

4.3.4 Discussion

All components of deformation are pictured by the pink curve, which was described in the beginning of this section. The components – elastic deformations, transient and stationary creep as soon as dilatancy – are considered by using the combined parameters of phase 1 and phase 2.

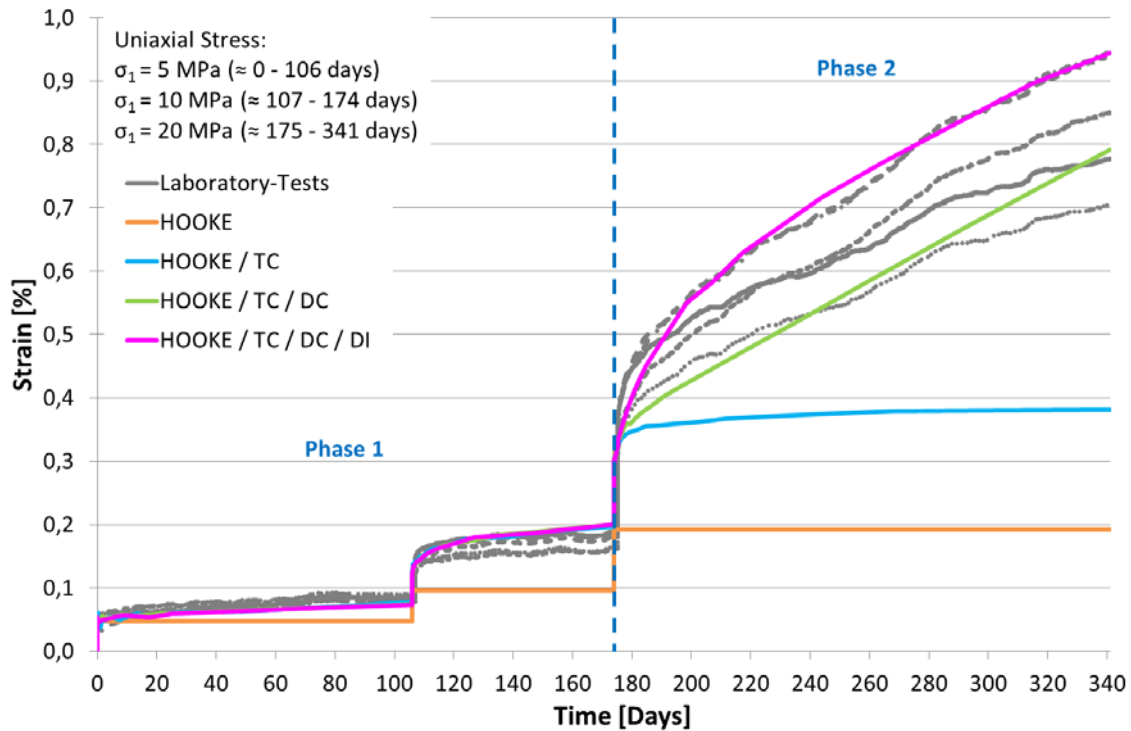


Fig. 4.35 Depiction of the deformation components, which results from the parameter variations before and the combination of adaptation in phase 1 and phase 2. Deformations consist of elastic deformations (HOOKE), transient creep (TC), dislocation creep (DC) and dilatancy (DI)

The development of strain rates is shown in Fig. 4.36 versus time and in Fig. 4.37 versus axial strain. Both figures show the development of strain rates resulting from the individual deformation components corresponding to Fig. 4.35.

If linear elastic and transient creep deformations were combined (using HOOKE and VP with parameters from phase 1), strain rates are high in the beginning after increasing axial stress and become smaller gradually (Fig. 4.36). Two values of strain rate are clearly too small in the first stress level. Probably, this might be a problem of iteration, because the curve in Fig. 4.35 has a small break at this moment. This deviation dissolves in further calculations by using more constitutive models.

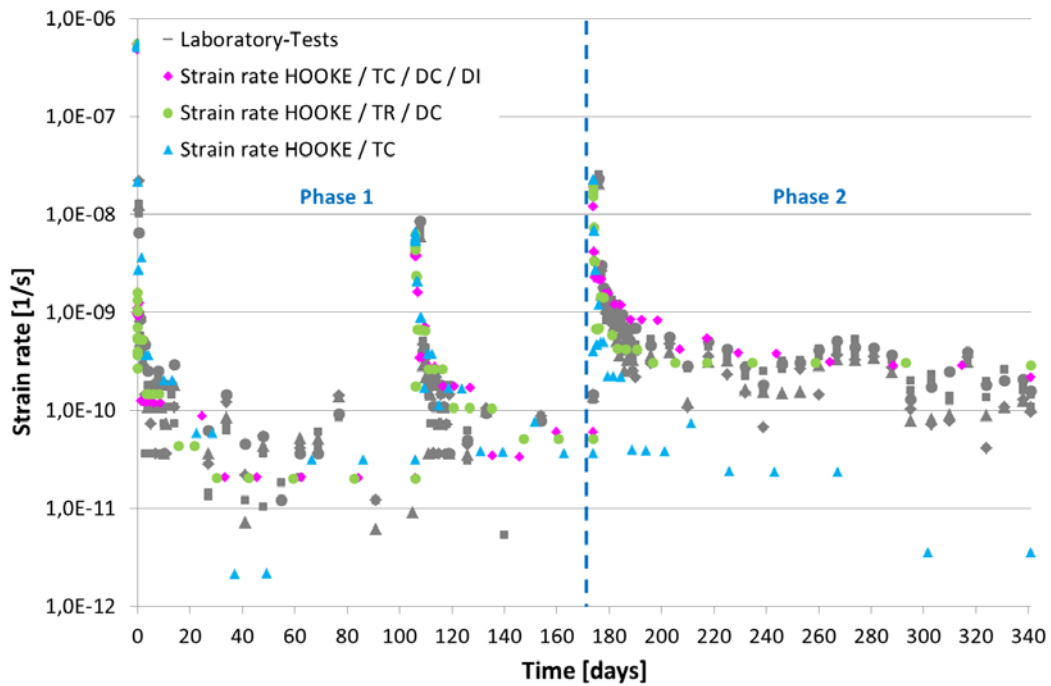


Fig. 4.36 Exercise UCc5 - Comparison between strain rates of laboratory tests and calculation results

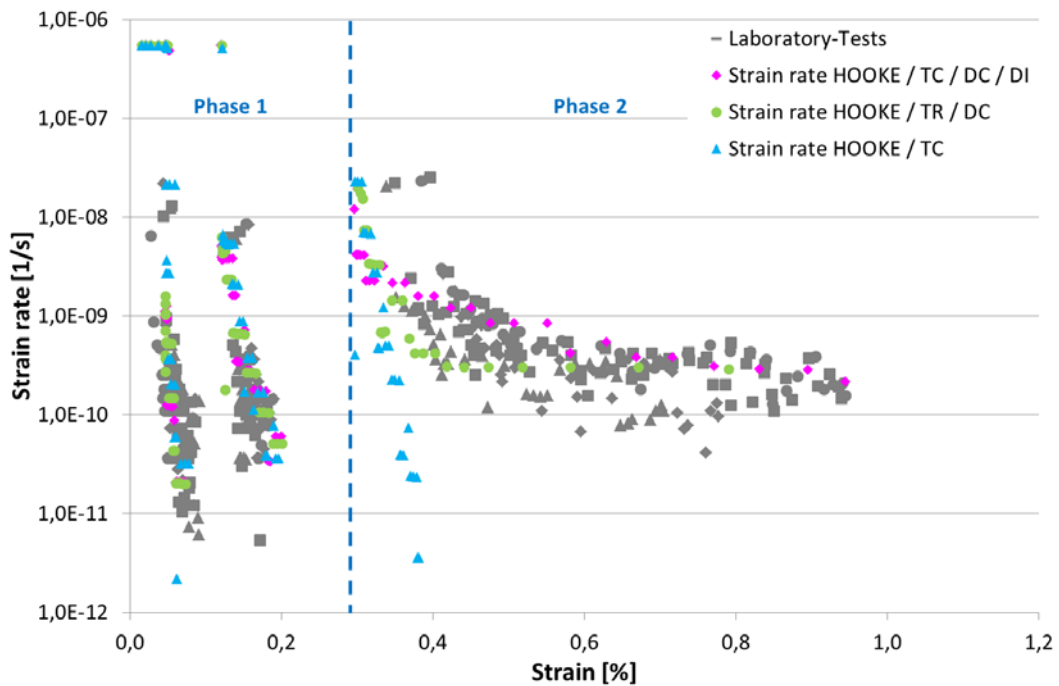


Fig. 4.37 Exercise UCc 5 - Comparison between strain rates versus axial strain of laboratory tests and calculation results

Generally, strain rates are in the right range for phase 1. In phase 2 strain rates are too small, because stationary creep and dilatancy were not considered yet. Fig. 4.37

shows the same circumstances: Strain rates are in the right range for phase 1, but are clearly too small in phase 2. Consequently, strains are too small.

If DC was used additionally to HOOKE and VP (with parameters for phase 1), the development of strain rates is similar as before in phase 1 in Fig. 4.35 and Fig. 4.36. The different steps of iteration can explain the small differences between the calculated strain rates. The deviation of strain rates in the first stress level from calculation before was extinct, which supports the assumption, that the process of iteration can explain the aberrations. Hence, stationary creep has less influence on phase 1. In phase 2, strain rates show a different development versus the calculation without DC. Fig. 4.35 and Fig. 4.36 show that strain rates are higher than before. They adapted much better to the laboratory results. Only in the beginning they decrease too fast, probably.

Finally, strain rates by using DC, HOOKE and VP with combined parameters for phase 1 and phase 2 were considered. Strain rates are in a good range for the second and third stress level in both figures. Strain rates decrease more slowly in phase 2 because of the shear thickening material behaviour. In the first stress level strains are a little bit too small in the second part (Fig. 4.36) as expected from consideration of Fig. 4.35. The depiction of strain rates versus strains shows, that strains develop rarely at a stress level of 5 MPa and become higher in the second stress level. A clear development of strains is shown in the third stress level. This development corresponds to the laboratory results. So the consideration of the development of strain rates supports, that the time dependent deformation behaviour of salt concrete is well simulated by using HOOKE, DC and VP with individual parameters for phase 1 and phase 2.

4.4 Simulation of the triaxial creep test

4.4.1 Model geometry

For simulation of the triaxial creep test, a 2-D-model was designed in GiD. The size specifications can be seen in Fig. 4.38. The model uses an axial symmetry around the y-axis, which is applicable due to the cylindrical shape of the sample. The steel piston is included in the model, as it is required to consider the loading induced conical regions of higher stress, which would else not be reproduced by the simulation.

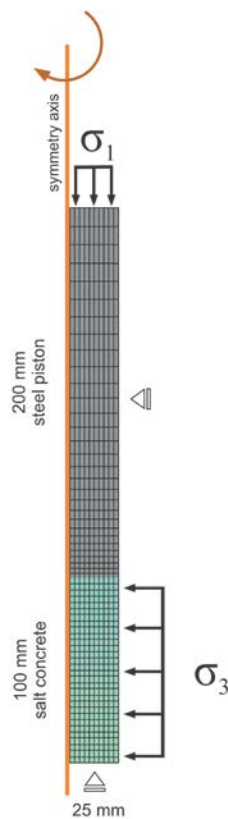


Fig. 4.38 Model layout in GiD for numerical calculation of the TCc-Test, showing geometry and meshing details

The mesh for simulation of the triaxial compression test was carried out with rectangular elements. The salt concrete was meshed by 250 rectangles with dimensions of 4 mm x 2.5 mm, not changing in size over the whole length of the sample. In order to achieve a finer discretization at the material transition, the mesh of the steel piston (250 rectangles) is denser at its lower boundary and gradually coarsens in y-direction. This

is due to the expectation, that the deformation and stresses are sensitive in this zone. The total amount of nodes for the used mesh is 561.

4.4.2 Boundary conditions and material properties

For constraining displacements in horizontal and vertical direction at the bottom of the salt concrete and in horizontal direction at the steel piston, nodal forces were generated at these parts of the model (Fig. 4.38). The fixed boundary condition at the bottom does not accord with the real situation of the test sample, but was necessary for the numerical calculation of the model. Stresses were applied according to the different load levels of the triaxial creep test.

Initial temperature, stress and porosity were assigned on the surfaces of salt concrete and the steel piston. The initial temperature corresponds to average temperature during the laboratory test and the initial stress is equal to atmospheric pressure. Initial porosity of salt concrete was in accordance with average porosity of the samples. The used initial values are shown in Tab. 4.27.

Tab. 4.27 Values of initial conditions for TCc-Test

	Salt concrete	Steel
Initial temperature [°C]	24	24
Initial stress [MPa]	0.1	0.1
Initial porosity [-]	0.058	0.001

Different constitutive laws were used in order to describe the mechanical behaviour of the samples. For the steel piston HOOKE was used. According to previous results from modelling salt concrete in triaxial compression and uniaxial creep tests /CZA 15/, salt concrete is supposed to have a linear elastic part and a viscoplastic part of deformation behaviour. Therefore, HOOKE, DC and VP were used for calculation. Parameters for HOOKE are shown in Tab. 4.28. As the material was already damaged before being tested, the elastic modulus of salt concrete is probably not applicable for the numerical calculation. Therefore, a new elastic modulus was calculated, based on the loading behaviour at the transition of phase 1 to phase 2, as the resolution at this boundary is best for all phases. The initial elastic modulus for pre-compaction of salt concrete has been significantly lowered to fit laboratory data as, due to non-deviatoric loading, an elastic modulus could not be calculated.

Tab. 4.28 Final used parameters for the Linear Elasticity law

	E-Modulus E [MPa]	Poisson ratio ν [-]	Reference porosity Φ₀ [-]
Salt concrete (initial)	5 400	0.18	0.058
Salt concrete	25 000	0.18	0.058
Steel	210 000	0.27	0.001

It is important to note, that the constitutive law for DC is only able to describe stationary creep. Previous studies on material parameters of rock salt, yielded good results for DC parameters similar to those for rock salt, described by /BGR 03/. However the pre-exponential parameters stay in the order of creep classes 0, 1 and 2 (comprising $0.065 \cdot 10^{-6}$ to $0.26 \cdot 10^{-6} 1/1 \cdot \text{MPa}^n$) for triaxial compression and uniaxial creep tests /CZA 15/. Only if those parameters do not sufficiently describe stationary creep in the present study, the full range of creep classes will be considered. The parameters for DC are shown in Tab. 4.29.

Tab. 4.29 Material properties for DISLOCATION CREEP law of saline materials

	Pre-exponential parameter A_A [1/1*MPaⁿ]	Activation energy Q_A [J/mol]	Stress power n [-]
Salt concrete	$0.065 \cdot 10^{-6} - 0.26 \cdot 10^{-6}$	54 000	5

To describe transient creep and dilatancy of salt concrete, the VP model was used. Data from previous parameter calibration /CZA 15/ yielded good results for the parameter sets in Tab. 4.30. Therefore, curve fitting is at first attempted with these parameters, before it is evaluated if an adaption is necessary.

Tab. 4.30 Parameters for the VISCOPLASTICITY model from /CZA 15/; triaxial creep test)

Parameter set 1	Stress power m [-]	Viscosity A [MPa⁻¹*s]	Activation energy Q [J/mol]	a₆ [-]	W_{d0} [-]
	8	$5 \cdot 10^{-9}$	54 000	0.02	3.5
	a₁ [-]	a₂ [-]	a₃ [-]	a₄ [-]	a₅ [-]
	2.5	1.8	2.5	0.7	0.02
Parameter set 2	m [-]	A [MPa⁻¹*s]	Q [J/mol]	a₆ [-]	W_{d0} [-]
	8	$5 \cdot 10^{-9}$	54 000	0.02	3.5
	a₁ [-]	a₂ [-]	a₃ [-]	a₄ [-]	a₅ [-]
	2.5	1.8	2.5	0.7	0.02

Additional to the parameters used for HOOKE, DC and VP, some parameters were needed for description of solid phase properties (Tab. 4.31). The density is the measured average density of the samples from TCc-Tests.

Tab. 4.31 Solid phase properties for calculation using CODE_BRIGHT

	Specific heat C_s [J/(kg*K)]	Density ρ_s [kg/m ³]	Expansion coefficient α_s [1/°C]	Reference temperature T_0 [°C]
Salt concrete	855	2 076	$4.2 \cdot 10^{-5}$	35
Steel	500	7 850	$1,0 \cdot 10^{-5}$	35

4.4.3 Modelling results versus experimental data

Different types of exercises were executed for finding the best approximation of calculation results to the laboratory test findings. During the calibration procedure, it has become evident, that the first deviatoric stress phase cannot be modelled with the same parameter set as phase 2 and 3. In order to obtain deformations that resemble laboratory data during phase 1, parameters would have to be modified in a way, which would produce unrealistically high deformations in the other two phases. In order to allow better comparability of laboratory tests and modelled curves, laboratory data has been fit at the beginning of phase 2.

Exercise 1: The parameter set from a previous study was used (HOOKE, DC and VP), as it has been successfully applied on modelling undamaged salt concrete.

Exercise 2: As the sample consists to 70% of rock salt, the occurrence of dislocation creep is expected. However, no phase of stationary creep could be identified in the experimental data. Therefore, strain rates of a numerical calculation using HOOKE and DC are compared with laboratory strain rates in order to define an upper boundary for the amount of strain, dislocation creep may contribute to absolute deformation.

Exercise 3: Viscoplastic deformation modelled with CODE_BRIGHT using the previously established parameter set was too low (cf. Exercise 1) and tertiary creep did not occur, therefore, parameters of the VP model were modified. The exercise was split in parts a, b and c and exclusively examines the behaviour during phase 3 ($\sigma_{dev} = 36$ MPa), as this phase is crucial for modelling tertiary creep. In Exercise 3a, parameters of HOOKE and DC were used according to Exercise 2 and parameter a_2 in the VP law was varied to allow tertiary creep. Exercise 3b aimed to adjust the onset of tertiary

creep , which - in Exercise 3a - deviates from laboratory data by modifying parameter W_{d0} . As strain rates were still too high after calculating Exercise 3b, parameter a_4 was varied in Exercise 3c to achieve an adequate fit.

Exercise 4: Numerical calculation was executed using HOOKE, DC and VP with the parameters established in Exercises 2-3. The resulting deformations are broken down by mechanical constitutive laws in order to illustrate the contribution of each law.

The level of axial stress is the changing condition between the different intervals in each calculation exercise. The increase in axial stress was simulated in smaller intermediate steps analogue to the progression of pressure in TCc-Test. The calculation was executed in eight intervals as constituted in Tab. 4.32. These time steps apply for all calculations.

Tab. 4.32 Time steps of calculation at TCc-Test; colors represent σ_1 and σ_3 at the end of each interval

Interval	Name	Time [Days]	Simulation
1		0.00 – 0.01	Axial stress increases from 0.1 MPa to 10 MPa; Radial stress increases from 0.1 MPa to 10 MPa
2	Pre-compaction phase	0.01 – 13.04	Axial stress of 10 MPa; radial stress of 10 MPa
3		13.04 – 13.05	Axial stress constant at 10 MPa; radial stress decreases from 10 MPa to 2 MPa
4	phase 1	13.05 – 69.01	Axial stress of 10 MPa; radial stress of 2 MPa
5		69.01 – 69.02	Axial stress increases from 10 MPa to 18 MPa; radial stress constant at 2 MPa
6	phase 2	69.02 – 116.13	Axial stress of 18 MPa; radial stress of 2 MPa
7		116.13 – 116.14	Axial stress increases from 18 MPa to 38 MPa; radial stress constant at 2 MPa
8	phase 3	116.14 – 139.00	Axial stress of 38 MPa; radial stress of 2 MPa

Exercise 1:

In Exercise 1, parameters from /CZA 15/were used in order to model salt concrete with HOOKE, DC and VP, see Tab. 4.33. They were calibrated for triaxial compression tests (set 1) and uniaxial creep tests (set 2) on undamaged salt concrete.

Tab. 4.33 Parameters for numerical calculations in Exercise 1

LINEAR ELASTICITY (set 1 / 2)	E [MPa]	ν [-]	ϕ_0 [-]		
	25 000	0.18	0.06		
DISLOCATION CREEP (set 1)	A_A [1/1*MPaⁿ]	Q_A [J/mol]	n [-]		
	$0.2 \cdot 10^{-6}$	54 000	5		
VISCOPLASTICITY (set 1)	m [-]	A [MPa⁻¹*s]	Q [J/mol]	a_6 [-]	W_{d0} [-]
	8	$5 \cdot 10^{-4}$	54 000	0.02	3.5
	a_1 [-]	a_2 [-]	a_3 [-]	a_4 [-]	a_5 [-]
	1.5	3.0	2.5	0.7	0.02
DISLOCATION CREEP (set 2)	A_A [1/1*MPaⁿ]	Q_A [J/mol]	n [-]		
	$0.065 \cdot 10^{-6}$	54 000	5		
VISCOPLASTICITY (set 2)	m [-]	A [MPa⁻¹*s]	Q [J/mol]	a_6 [-]	W_{d0} [-]
	8	$5 \cdot 10^{-9}$	54 000	0.02	3.5
	a_1 [-]	a_2 [-]	a_3 [-]	a_4 [-]	a_5 [-]
	1.9	1.8	2.5	0.7	0.02

Fig. 4.39 shows the results of numerical calculation compared with laboratory data. It is evident, that the used parameter set cannot sufficiently describe the deformation behaviour, observed in laboratory tests, as a viscoplastic component in modelled deformation is almost completely absent. The cause might be the increased radial stress of 2 MPa, compared to 0.1 MPa in the test for which the parameters were established.

This increase in radial stress leads to a higher stiffness of the sample. Hence, viscoplastic parameters calibrated for the weaker material have to be adapted for the current model. As parameter set 2 shows at least a little amount of viscoplastic deformation, adaption in Exercise 3 will be based on this set.

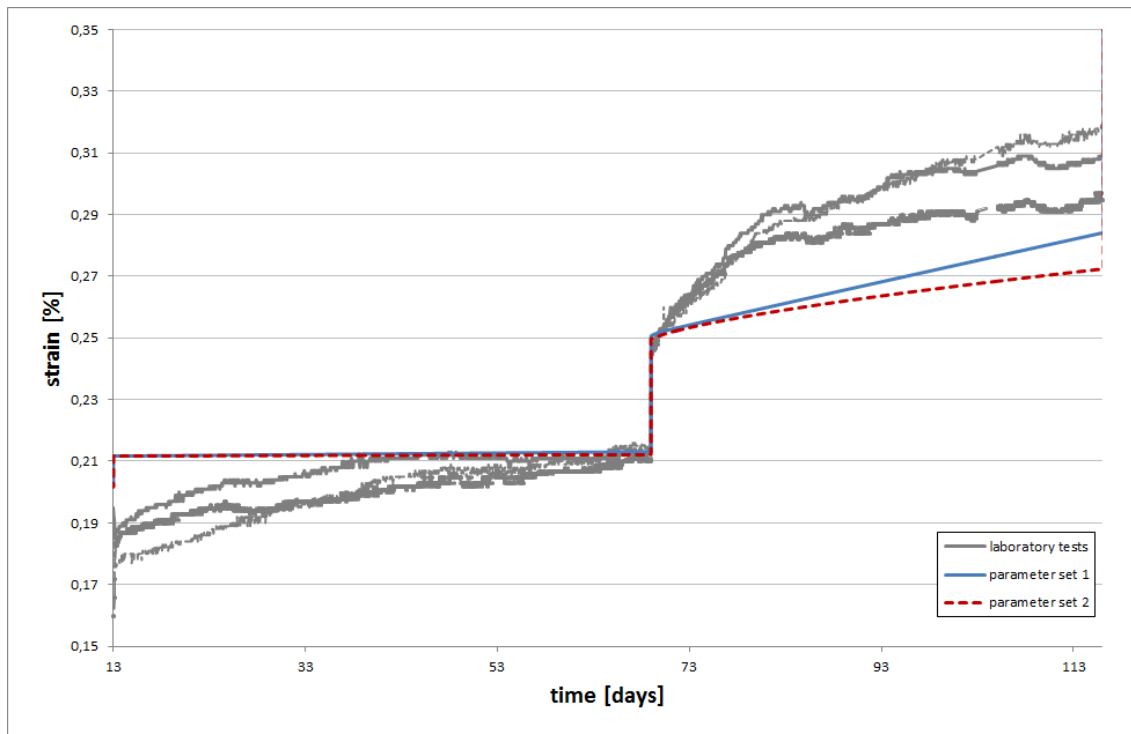


Fig. 4.39 Comparison between the results of the laboratory TCc-Test and the result of numerical calculation using LINEAR ELASTICITY, DISLOCATION CREEP and VISCOPLASTICITY law with parameters from /CZA 15/

Exercise 2:

Before adapting the viscoplastic parameters, an upper boundary for the dislocation creep component in total deformation is established. This serves the purpose to already model absolute deformation in Exercise 3 and avoids a “back and forth” iterative process incorporating continuously changing either viscoplastic or dislocation creep parameters in order to obtain the best fit. Dislocation creep describes the component of transient creep. Phase 2 from 69 to 116 days has been identified as being most vulnerable to dislocation creep among the 3 phases. Therefore, the upper limit is established in this phase.

Numerical calculations were executed using different creep classes, according to /BGR03/. Parameters were as in Tab. 4.34. As previous numerical calculations on salt concrete have been successfully adapted for pre-exponential parameters A_A in the range of creep class 0-2 ($0.065 - 0.26 \cdot 10^{-6} [1/1 \cdot \text{MPa}^n]$), this range is examined in Exercise 2. Furthermore, creep class 3 ($A_A = 0.56 \cdot 10^{-6} [1/1 \cdot \text{MPa}^n]$) has been included.

Tab. 4.34 Exercise 2 - varied parameters are marked red

LINEAR ELASTICITY (set 1 / 2)	E [MPa]	ν [-]	ϕ_0 [-]
		25 000	0.18
DISLOCATION CREEP (set 1)	A_A [1/1*MPa ⁿ]	Q_A [J/mol]	n [-]
	varied	54 000	5

Fig. 4.40 shows the results of numerical calculations using different pre-exponential parameters. It is important to note, that the lowest strain rates occur at the end of phase 2. Strain in creep class 3 is significantly too high. This is also confirmed by the strain rate diagram (Fig. 4.41). Additionally, strain rates in creep class 2 are too high for samples 1060 and 1062 at the end of deviatoric stress phase 2, while creep classes 0 and 1 are in good agreement with laboratory tests. Therefore, the upper boundary of dislocation creep is set at creep class 1, which corresponds to $A_A = 0.13 \cdot 10^{-6}$ [1/1*MPaⁿ]. As viscoplastic deformations will add up to the deformations from dislocation creep, class 1 is probably still too high. Thus, creep class 0 ($0.065 \cdot 10^{-6}$ [1/1*MPaⁿ]) is considered for the following calculations.

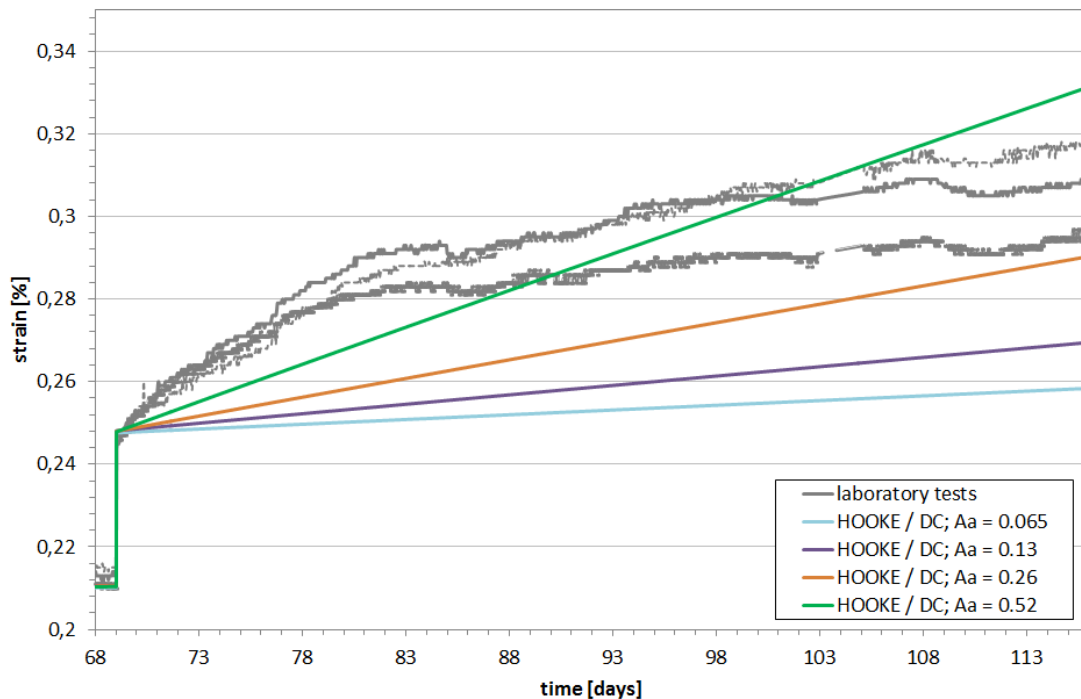


Fig. 4.40 Comparison between the results of the laboratory TCc-Test and modeling, using LINEAR ELASTICITY and DISLOCATION CREEP law with various pre-exponential parameters corresponding to creep classes 0 to 3

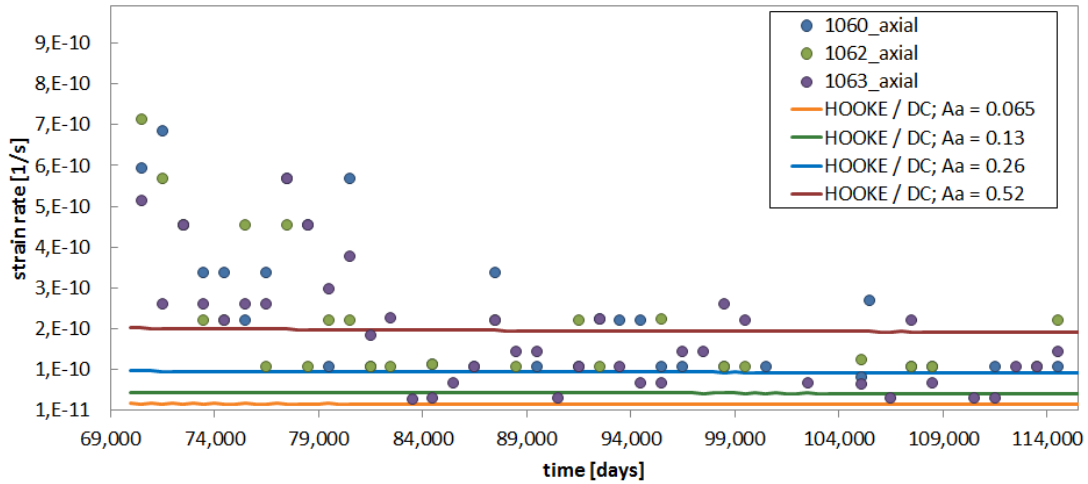


Fig. 4.41 Strain rates for numerical calculations using different pre-exponential parameters in comparison with laboratory data (circles)

Exercise 3a:

Due to the material behaving too stiff in numerical calculations using the parameter sets from /CZA 15/, it was not able to describe tertiary creep (as indicated by strain rate acceleration) observed in laboratory tests. Therefore, a_2 is varied in order to permit greater volumetric extension and, with this, tertiary creep. Due to the fact that a_2 influences both, the flow rule G and the yield function F (cf. Equation 4.11, page 54), it was chosen for this adaption. The parameters used for the numerical calculation can be seen in Tab. 4.35.

Tab. 4.35 Exercise 3a - varied parameters are marked red

LINEAR ELASTICITY	E [MPa]	ν [-]	ϕ_0 [-]		
	25 000	0.18	0.06		
DISLOCATION CREEP	A_A [1/1*MPaⁿ]	Q_A [J/mol]	n [-]		
	0.065·10 ⁻⁶	54 000	5		
VISCOPLASTICITY	m [-]	A [MPa⁻¹*s]	Q [J/mol]	a_6 [-]	W_{d0} [-]
	8	5·10 ⁻⁹	54 000	0.02	3.5
	a_1 [-]	a_2 [-]	a_3 [-]	a_4 [-]	a_5 [-]
	1.9	varied	2.5	0.7	0.02

Fig. 4.42 shows the results of varying a_2 in phase 3 ($\sigma_{dev} = 36$ MPa). In contrast to laboratory data, curves modeled with $a_2 = 0.9$ and 0.8 show no strain acceleration. Only at the tail of the curve $a_2 = 0.7$, a slight upward bending can be observed, which is interpreted as tertiary creep. This becomes more evident in Fig. 4.43, which shows the equivalent strain rates.

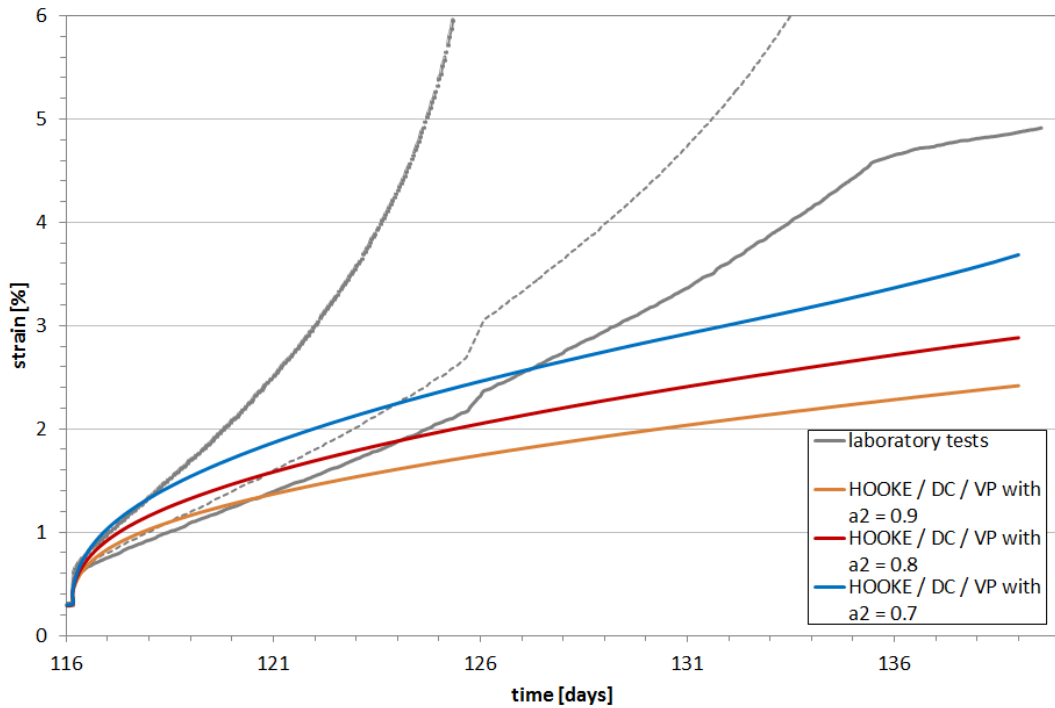


Fig. 4.42 Comparison between the results of the laboratory TCC-Test and modeling, using LINEAR ELASTICITY, DISLOCATION CREEP and VISCOPLASTICITY law with a_2 between 0.9 and 0.7

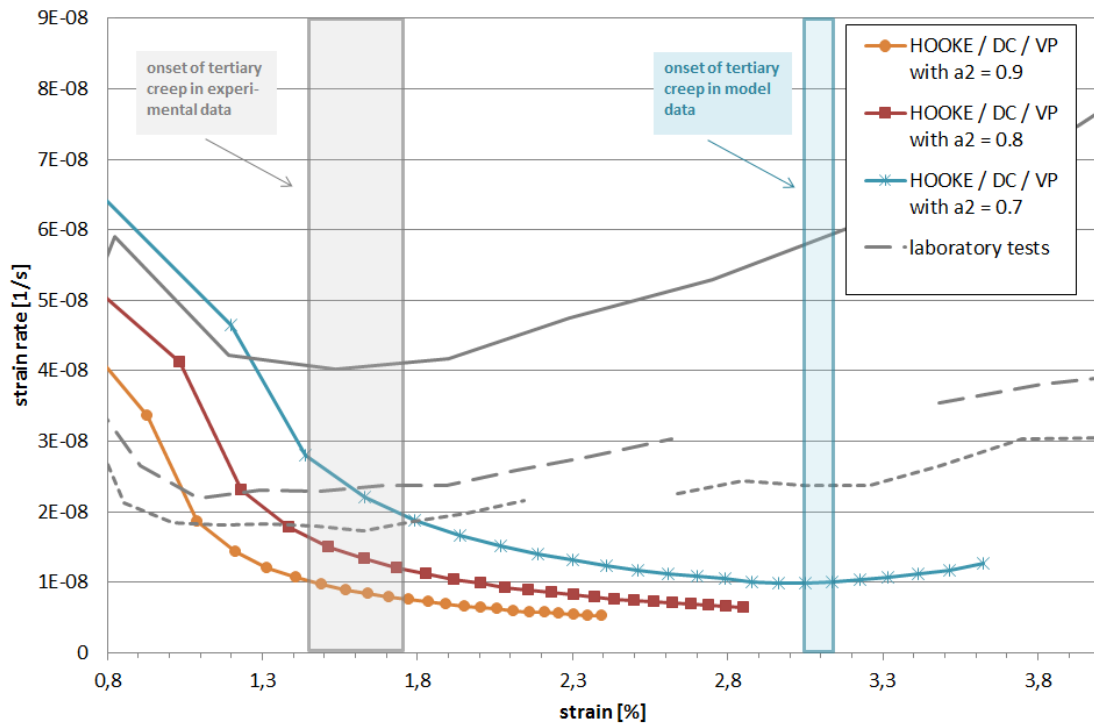


Fig. 4.43 Strain rates for numerical calculations varying parameter a_2 between 0.9 and 0.7

Again, values for a_2 of 0.9 and 0.8 are obviously too high, as they show no strain acceleration and thus no tertiary creep. At axial strain of about 3.1% there is a sudden onset of tertiary creep in the curve using $a_2 = 0.7$, which is indicated by a blue box. After this point, strain rates continuously increase, so strain acceleration and hence tertiary creep occurs. However, in laboratory data, the onset of tertiary creep has been identified at lower axial strains between 1.45 and 1.75% (grey box in Fig. 4.43). This discrepancy will be examined in the forthcoming Exercise 3b.

Exercise 3b:

In Exercise 3a, a parameter set was found, which is able to describe strain acceleration. However, the transition from strain hardening to strain acceleration in the model is still at higher axial strains than in experimental data and has yet to be calibrated. For this purpose, the parameter W_{d0} , representing plastic deformation work is varied. Due to the parameter being in a Foepl-bracket (cf. Equation 4.12, page 54), it constitutes the threshold, at which strain acceleration is permitted. So W_{d0} is reduced in order to allow transition to strain acceleration at lower axial strains. As the threshold is never exceeded in phase 2 ($\sigma_{dev} = 16$ MPa) deformations there are not affected by adjusting W_{d0} . Parameters used for the numerical calculation are displayed in Tab. 4.36.

Tab. 4.36 Exercise 3b - varied parameters are marked red

LINEAR ELASTICITY	E [MPa]	ν [-]	ϕ_0 [-]		
	25 000	0.18	0.06		
DISLOCATION CREEP	A_A [1/1*MPaⁿ]	Q_A [J/mol]	n [-]		
	$0.065 \cdot 10^{-6}$	54 000	5		
VISCOPLASTICITY	m [-]	A [MPa⁻¹*s]	Q [J/mol]	a_6 [-]	W_{d0} [-]
	8	$5 \cdot 10^{-9}$	54 000	0.02	varied
	a_1 [-]	a_2 [-]	a_3 [-]	a_4 [-]	a_5 [-]
	1.9	0.7	2.5	0.7	0.02

Results from varying W_{d0} are shown in Fig. 4.44. Curves for a W_{d0} of 2.2 to 1.9 have their onset of tertiary creep still outside the window, defined by experimental data, so values for W_{d0} are too high. In contrast, the curve for W_{d0} of 1.7 shows an onset of strain acceleration corresponding well with the onset observed in laboratory tests. Therefore, a W_{d0} of 1.7 is chosen for further calculations. However, strain rates become too high around axial deformations of 3.5 %, so this will be adjusted in Exercise 3c. Please note how the curves overlap before tertiary creep is triggered, as this gives evidence for W_{d0} acting as a threshold value.

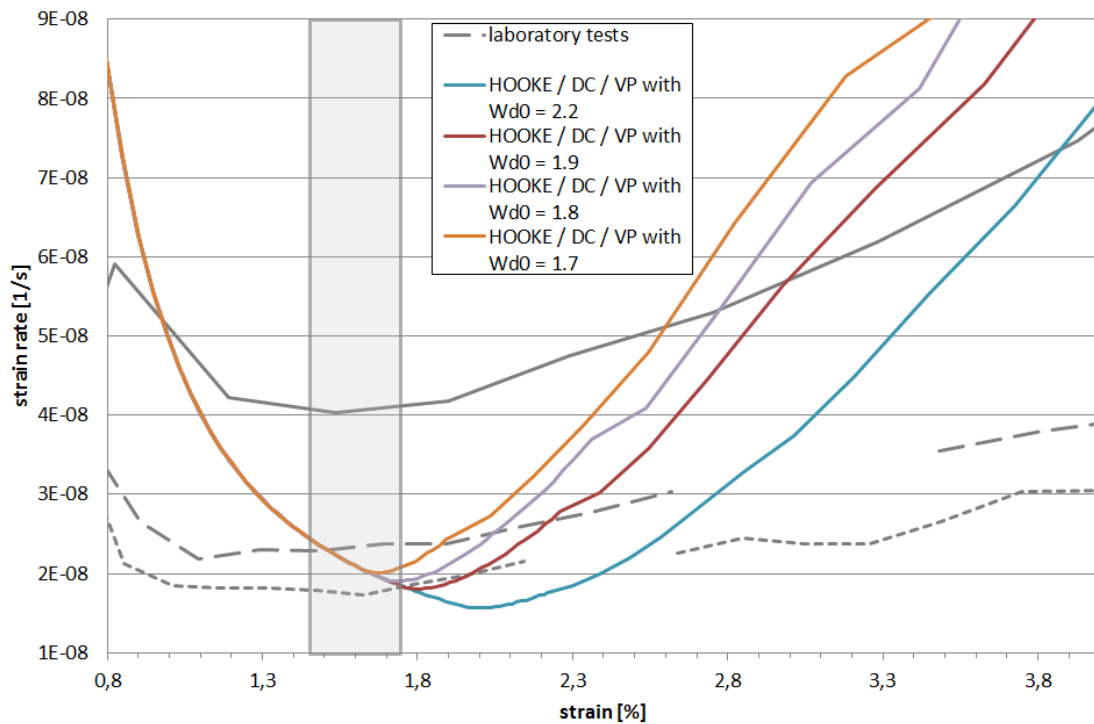


Fig. 4.44 Strain rates of numerical calculations for parameter W_{d0} between 2.2 and 1.7

Exercise 3c:

In Exercise 3b, the onset of tertiary creep was adjusted so that it is in agreement with experimental data. Still strain rates during tertiary creep are a little too high in the model. This can be controlled by decreasing parameter a_4 , which is a pre-factor of the Foeppel-bracket including W_{d0} (cf. Equations 4.12 and Exercise 3b) and therefore is only active during strain acceleration. Hence, reducing a_4 scales down deformations during tertiary creep. It has to be stated for future calculations, that parameter a_6 serves the same purpose with the difference, that it also affects deformations during transient and stationary creep.

In the present exercise, a_4 is gradually decreased until strain rates during tertiary creep fit with those observed in experimental tests. The parameters used for the numerical calculation are shown in Tab. 4.37.

Tab. 4.37 Exercise 3c - varied parameters are marked red

LINEAR ELASTICITY	E [MPa]	ν [-]	ϕ_0 [-]		
		25 000	0.18	0.06	
DISLOCATION CREEP	A_A [$1/1 \cdot \text{MPa}^n$]	Q_A [J/mol]	n [-]		
	$0.065 \cdot 10^{-6}$	54 000	5		
VISCOPLASTICITY	m [-]	A [$\text{MPa}^{-1} \cdot \text{s}$]	Q [J/mol]	a_6 [-]	W_{d0} [-]
	8	$5 \cdot 10^{-9}$	54 000	0.02	1.7
	a_1 [-]	a_2 [-]	a_3 [-]	a_4 [-]	a_5 [-]
	1.9	0.7	2.5	varied	0.02

Reducing a_4 effectively reduces the strain rate observed in numerical calculation (Fig. 4.45). While a value for a_4 of 0.7 seems too high, values between 0.6 and 0.5 appear to be in good agreement with those measured in laboratory tests. But looking at Fig. 4.46 reveals, that for $a_2 = 0.5$, strain acceleration is very low and does not adequately describe the deformation behaviour of the laboratory tests, especially around 135 days. Therefore, an a_4 of 0.6 is chosen for the final calculation.

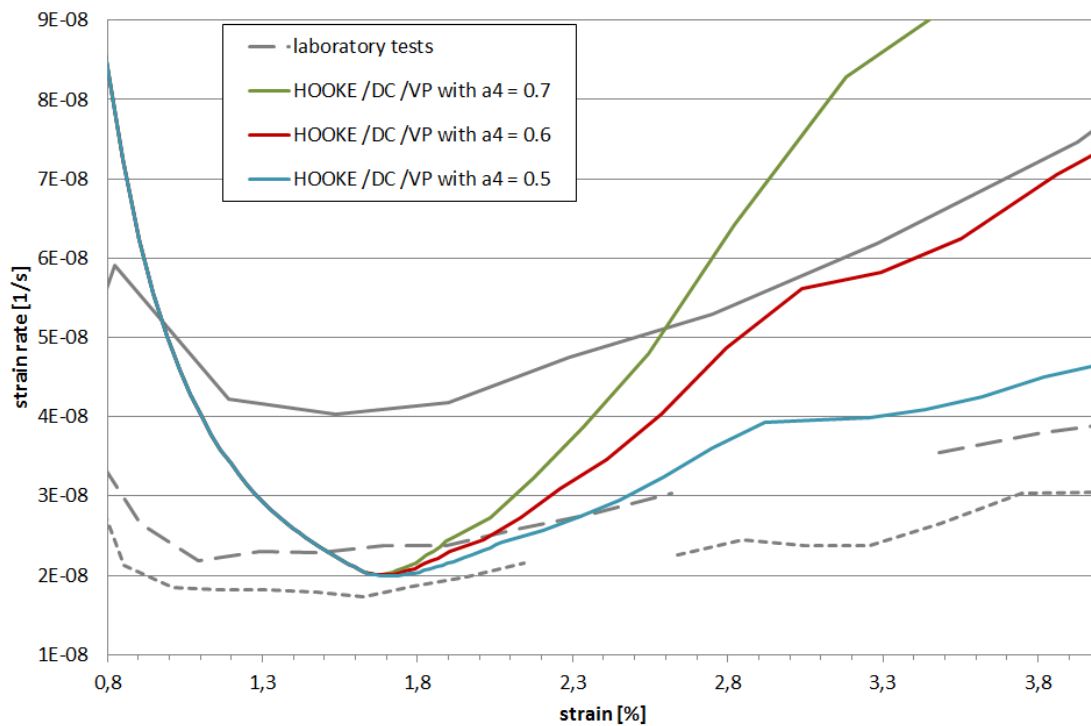


Fig. 4.45 Strain rates of numerical calculations for parameter a_4 between 0.7 and 0.5

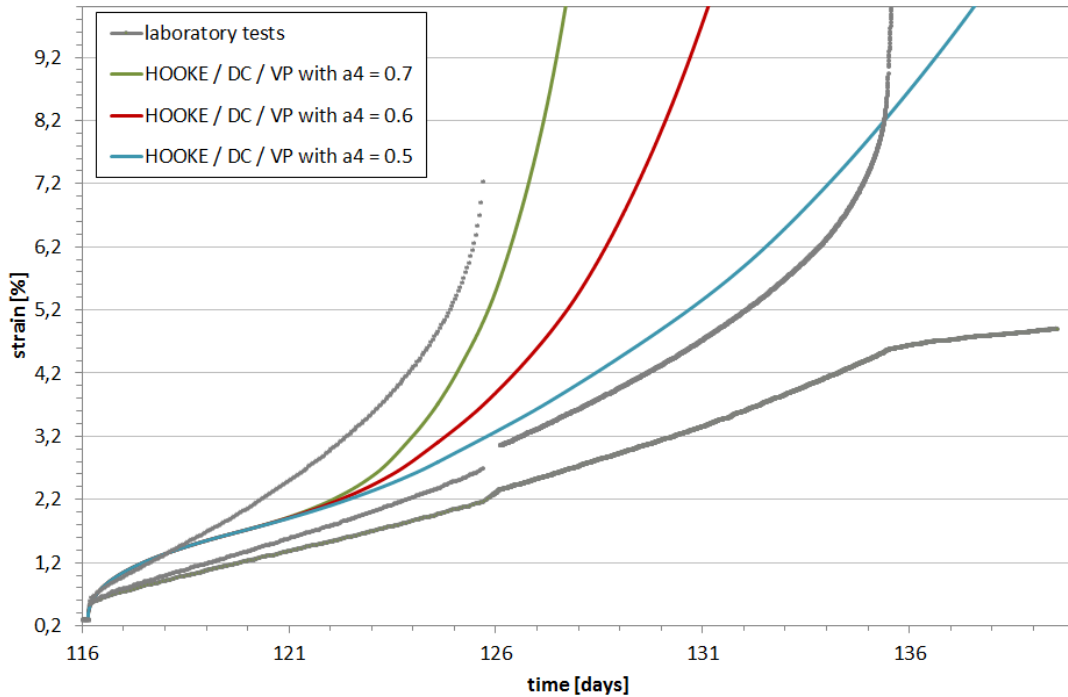


Fig. 4.46 Comparison between the results of the laboratory TCc-Test and modeling, using LINEAR ELASTICITY, DISLOCATION CREEP and VISCOPLASTICITY law with a_4 between 0.7 and 0.5

Exercise 4

Numerical calculation is executed, using HOOKE, DC and VP parameters as established in the previous Exercises 1-3 (cf. Tab. 4.38)

Tab. 4.38 Parameters for numerical calculation of Exercise 4

LINEAR ELASTICITY	E [MPa]	ν [-]	ϕ_0 [-]		
	25 000	0.18	0.06		
DISLOCATION CREEP	A_A [1/1*MPaⁿ]	Q_A [J/mol]	n [-]		
	$0.065 \cdot 10^{-6}$	54 000	5		
VISCOPLASTICITY	m [-]	A [MPa⁻¹*s]	Q [J/mol]	a_6 [-]	W_{d0} [-]
	8	$5 \cdot 10^{-9}$	54 000	0.02	1.7
	a_1 [-]	a_2 [-]	a_3 [-]	a_4 [-]	a_5 [-]
	1.9	0.7	2.5	0.6	0.02

The results of the combined constitutive laws are shown in the red curve of Fig. 4.47 (phase 1 + 2) and Fig. 4.48 (phase 3). Its behaviour corresponds well to laboratory tests in phase 2 and 3, but is not able to describe deformations in phase 1.

Deformation behaviour is broken down into its individual components of each constitutive law in Fig. 4.47 and Fig. 4.48. Calculations executed with only using linear elastic law (HOOKE) show exclusively deformations during deviatoric stress increase. There are no time-dependent deformations. Calculating with HOOKE and the dislocation creep law (DC) yield the same elastic steps after stress increase, but also shows steady-state creep, which leads to continuous deformation. Adding the viscoplastic constitutive law to calculation results in transient creep deformations in phase 2 and 3, shows a strain hardening effect, indicated by diminishing strain rates (Fig. 4.49). If tertiary creep is allowed, it takes place in phase 3 (Fig. 4.48), where after initial transient creep, strain acceleration occurs, which indicates a propagation of micro cracks.

Strains acquired from numerical calculations correspond well with those observed in experimental data (Fig. 4.49). CODE_BRIGHT slightly underestimates viscoplastic deformations at the beginning of phase 2 (however less than half an order of magnitude) and overestimates deformations of the first data point in phase 3 by one order of magnitude.

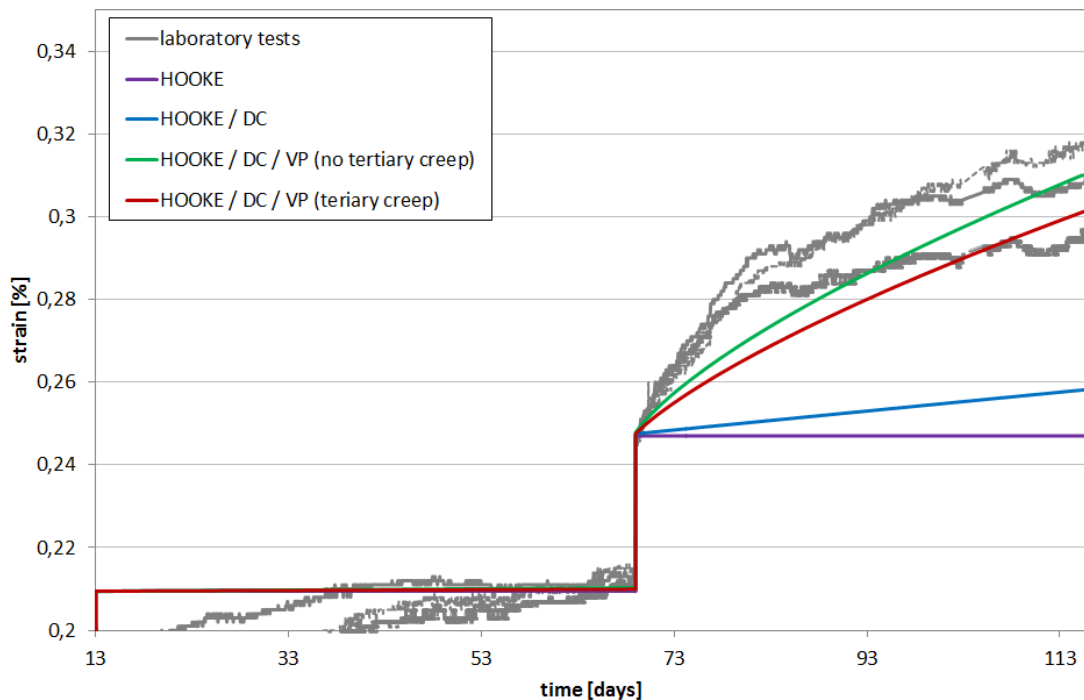


Fig. 4.47 Comparison between the results of the laboratory TCc-Test and modeling in phase 1 and 2, using LINEAR ELASTICITY, DISLOCATION CREEP and VISCOPLASTICITY law

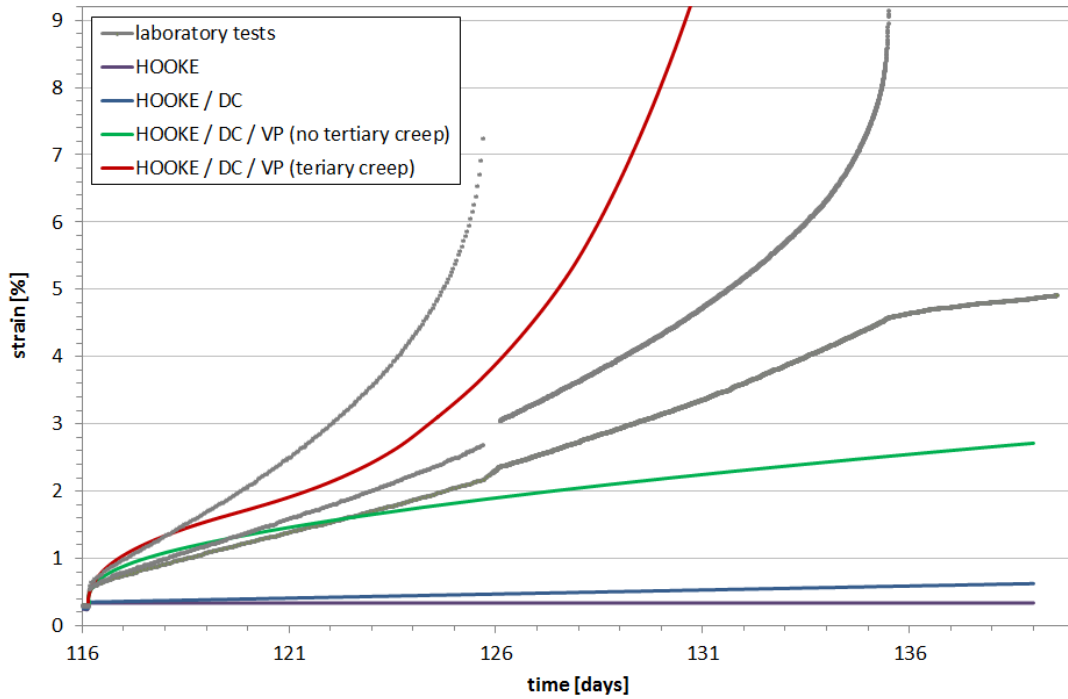


Fig. 4.48 Comparison between the results of the laboratory TCc-Test and modeling in phase 3, using LINEAR ELASTICITY, DISLOCATION CREEP and VISCOPLASTICITY law

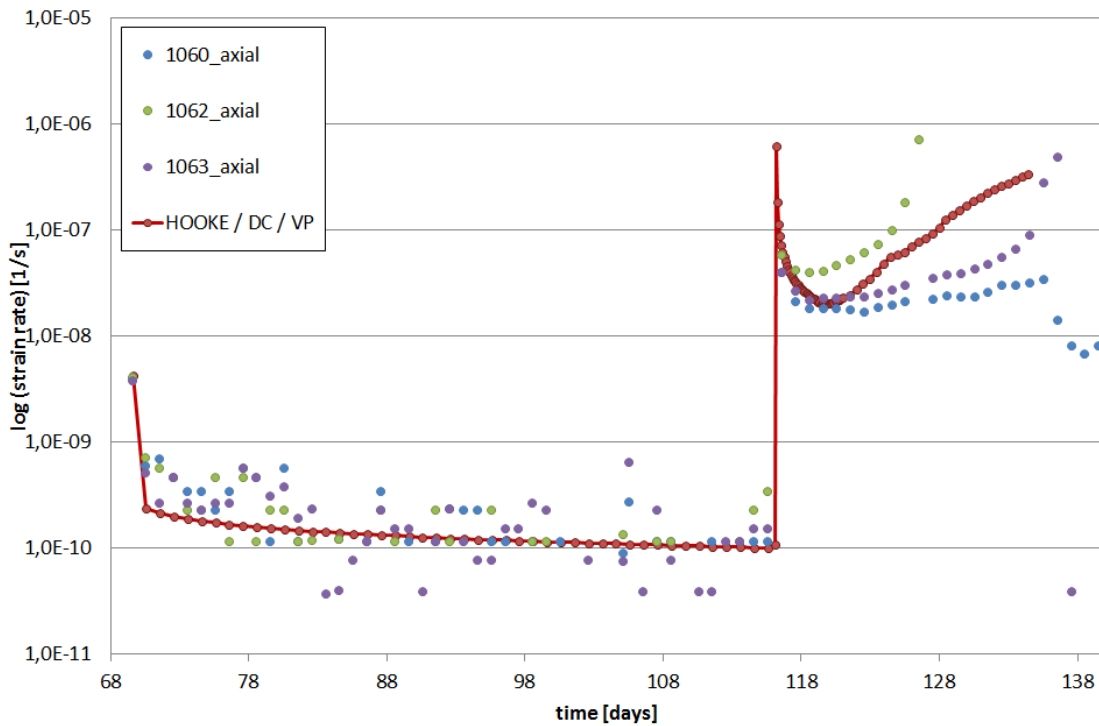


Fig. 4.49 Measured strain rates (colored points) versus strain rates from numerical calculation (red line) in phase 2 and 3

The development of porosity is shown in Fig. 4.50 (please note that there are two y-axes in order to depict porosities for phase 1 and 2 in one diagram). Dilatancy occurs in both, phase 2 and 3, but is in an order of 10^{-3} % for phase 2. For phase 3, porosity significantly increases in conjunction with tertiary creep, which sets in at around 120 days and causes an increase in porosity of about 15%.

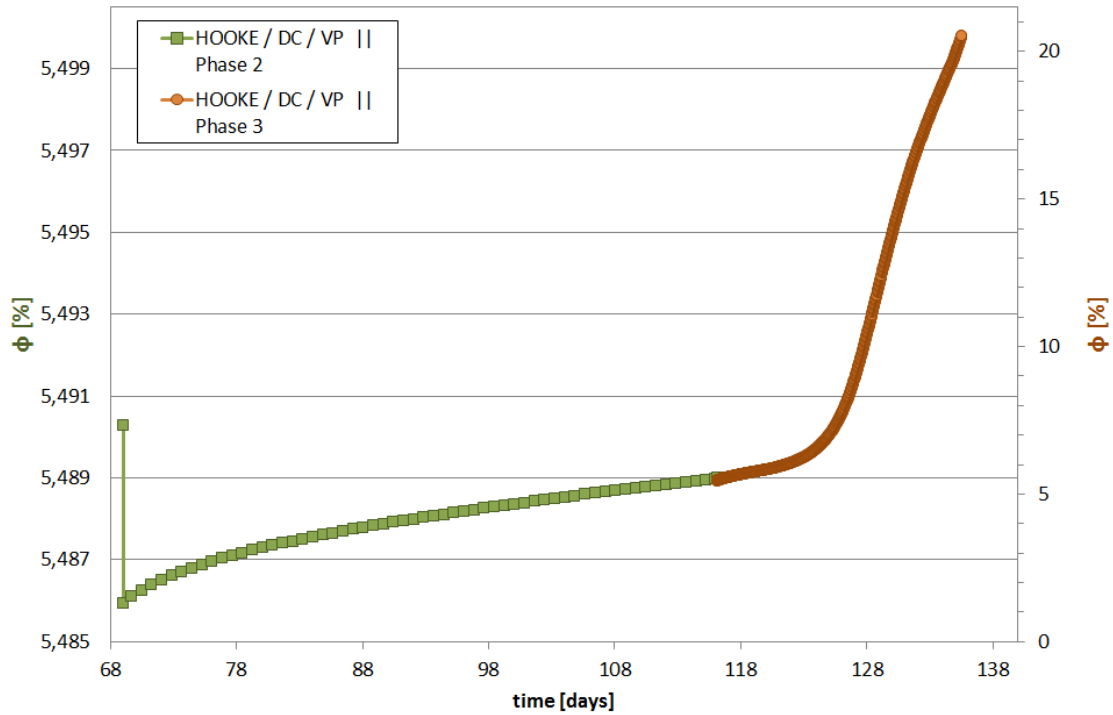


Fig. 4.50 Porosity development in phase 2 and 3 for numerical calculation

4.4.4 Discussion

During the course of Exercises 1-4, it has become evident, that LINEAR ELASTIC, DC and VP laws can sufficiently describe the deformation behaviour in phase 2 and 3. In phase 1, deformations modelled with CODE_BRIGHT are significantly lower than those observed in laboratory tests. When thinking of a possible explanation, one has to bear in mind, that the sample exceeded the dilatancy boundary before being tested in the laboratory, so the sample was already damaged. In the pre-compaction phase, at hydrostatic stress conditions (10 MPa), creep is higher than in phase 1 with 8 MPa deviatoric stress. This makes no sense when only considering processes for undamaged material. We suggest that during pre-compaction and phase 1, damage induced micro cracks and porosity were eliminated by grain rearrangement and creep of rock salt into voids. As the effect on axial deformation of these processes decreases with reduction

of void ratio, it explains the higher strains during pre-compaction, because DC and VP deformations in phase 1 are not yet on a level, which can compensate the diminution of compaction creep. The above mentioned processes have not been implemented in the constitutive laws used for calculations in the present study, so strains in numerical calculations are too low during phase 1. However, there is evidence, that the VISCOPLASTICITY law affecting transient creep shows a higher stress dependence of deformation, as there actually is in laboratory tests. With the parameter set established in the present study, there is no transient creep deformation in calculations of phase 1 whatsoever, although it is present in the current laboratory tests and in tests on undamaged salt concrete at atmospheric pressure /CZA 15/ and on other impure rock salts at a confining pressure of 10 MPa/ZHA 12/. So it seems unlikely, that compaction creep is the only process leading to transient creep during phase 1, which implies, that calculations executed with CODE_BRIGHT yield too low viscoplastic deformations at low stress levels. This phenomenon can also be seen in /CZA 15/, Fig. 4.29, and is therefore not limited to the present study.

Issues of the developed approach, especially the description of the viscoplastic material behaviour, became evident during the calibration work. The assumption that the mechanical behaviour of salt concrete can be simulated similarly to the behaviour of rock salt is limited, because salt concrete is not a homogeneous material /CZA 16/.

Salt concrete represents a composed material, whose global mechanical behaviour is influenced by the mechanical behaviour of its individual components. Hence, a suitable constitutive law has to be found, which is able to distinguish between the mechanical behaviour of the different components (salt grains, cement matrix and voids).

The “Argillite-Model” was implemented in the previously released versions of Code_Bright to describe the mechanical behaviour of soft argillaceous rocks. In general, an argillaceous rock is composed of solid phases, liquid phases and gaseous phases. Beside bigger calcite and quartz grains, microscopic crystals (clay minerals) in form of sheets represent the solid phase or “matrix”. Naturally deposited cement agents (silica, carbonates and hydroxides) can be considered as a paste, which bonds the matrix together. Consequently, the liquid phases (e.g. water molecules) and gaseous phases (e.g. air) are captured by the described bonds and the matrix /VAU 03/.

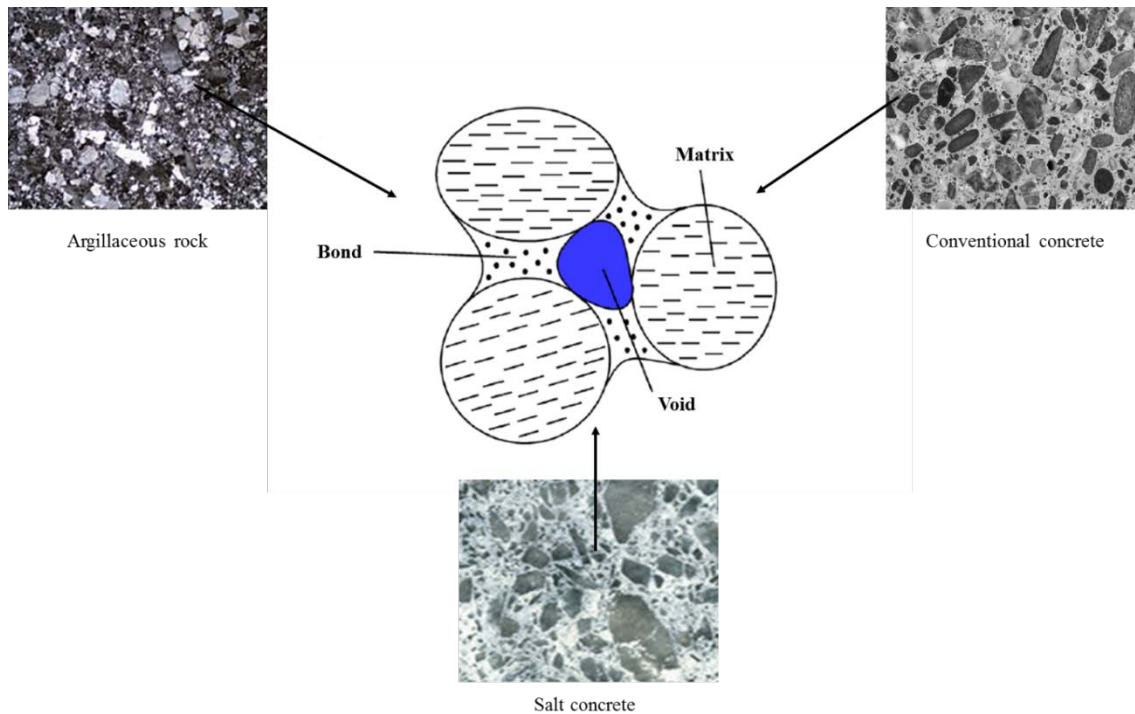


Fig. 4.51 Different composed materials (Argillaceous rock, Conventional concrete and Salt concrete) and their similarities (Matrix, Bonds, and Voids)

As it becomes visible in Fig. 4.51, the hypothesis of applying the “Argillite-Model” to simulate other composed materials than argillaceous rock evolved from the great amount of similarities of composed materials. The application would make sense, because most of composed materials include the above mentioned matrix, bonds and voids. Hence, it should be possible to use the “Argillite-Model” to simulate the mechanical behaviour of salt concrete (salt grains and cement stone).

Currently, there is a Master Thesis in preparation that deals with the description of both, short- and long-term mechanical behaviour involving an advanced plasticity model approach, /MID 17/. The Master thesis is supported by GRS, TUC and UPC.

5 Summary and outlook

This report presents the status of the work performed by GRS during 48 months in the LASA project /FKZ 02E11132/ to improve the way how geotechnical sealings are represented in integrated performance assessment models for radioactive waste repositories in salt.

The deformation behaviour of salt concrete was investigated by laboratory testing and numerical modelling. In the laboratory different types of tests were carried out: Triaxial compression tests, uniaxial and triaxial creep tests. The tests were simulated using CODE_BRIGHT and the calculation results were compared to the laboratory results. The simulation of the triaxial tests aimed at the investigation of material changes between the second and third stress level in the uniaxial tests. The results were useful because the onset of dilatancy could be pinpointed. In all the simulations, the onset of dilatancy occurred before the load limit was reached. The perceptions of the uniaxial tests in combination with the results of the triaxial tests showed that the material behaviour of salt concrete at an axial stress up to 10 MPa is different from the material behaviour at 20 MPa. Strains and strain rates clearly increase at higher stresses. The simulations showed that an adaptation to laboratory results was only possible if two different sets of parameters were used at the lower stress level (phase 1) and the higher stress level (phase 2). The main problem of simulating the deformation behaviour of salt concrete is the description of the viscoplastic (transient creep) material behaviour. Elastic deformations and stationary creep can be adapted by the available material properties. For a better description of transient material behaviour a constitutive model should be adapted or developed. The constitutive model used here allowed only a mathematical adaptation. Salt concrete consists of the cement matrix and the grains of salt concrete. This structure and its changes could not really be considered yet. If the structure of salt concrete could be considered in detail, the description of the deformation behaviour at different stress levels would become easier and clearer. Further investigations and developments in this direction are necessary.

Currently, there is a Master Thesis in preparation that deals with the description of both, short- and long-term mechanical behaviour involving an advanced plasticity model approach.

Furthermore, GRS is investigating the sealing capacity of combined systems of salt concrete seal elements and surrounding rock salt at the laboratory scale. Currently, the

following results have been obtained. At dry conditions and a moderate confining stress up to 5 MPa, the reconsolidation is slow. A potentially existing highly permeable contact seam between the seal element and the rock will not be closed, at least not in the short term. With an intact seal element, a confining stress of 5 MPa is, however, sufficient to prevent brine flow along the seal. In the presence of brine, contact seam and EDZ are quickly closed, resulting in an overall permeability below 10^{-20} m^2 . A pre-damaged seal element (e.g. damaged by shrinkage fracturing during construction) will not be re-consolidated at a confining stress of 5 MPa, even if brine is present. At a confining stress of 10 MPa and a testing time of 6 months the contact seam and the EDZ are closed with time, resulting in an overall permeability below $1 \cdot 10^{-18} \text{ m}^2$.

For a numerical simulation of the seal/rock salt system, available physical models of rock salt and salt concrete will be applied to the experiments described here and simulation/improvement cycles will be performed to advance model validation and calibration. It is foreseen that these hydro-mechanical coupled calculations will be executed within the national project LASA-EDZ /FKZ 02E11243/.

6 Zusammenfassung und Ausblick

In diesem Bericht wird der Stand der GRS-Arbeiten im 48 Monate währenden LASA-Projekt /FKZ 02E11132/ zusammengefasst. Die Arbeiten hatten das Ziel, die Darstellung von geotechnischen Verschlussystemen in integrierten Auswertungsmodellen für radioaktive Abfälle in Endlagern im Salz zu verbessern. Durch Laborexperimente und begleitende modelltheoretische Arbeiten wurde das Verformungsverhalten von Salzbeton untersucht.

Im Labor wurden verschiedene Arten von Versuchen durchgeführt: Triaxiale Kompressionsversuche sowie einaxiale und triaxiale Kriechversuche. Die Laborversuche wurden mit CODE_BRIGHT simuliert und die Berechnungsergebnisse wurden mit den Laborergebnissen verglichen. Zwischen dem zweiten und dritten Druckniveau im einaxialen Versuch auftretende Materialveränderungen konnten mit Hilfe von Simulationsergebnissen der triaxialen Versuche erklärt werden. Dabei konnte auch das Einsetzen der Dilatanz aufgezeigt werden. Bei allen Simulationen setzte die Dilatanz ein, bevor die Belastungsgrenze erreicht wurde. Die Erkenntnisse der einaxialen Versuche in Verbindung mit den Ergebnissen der triaxialen Versuche ergaben, dass sich das Materialverhalten von Salzbeton bei einer axialen Belastung bis 10 MPa von dem Materialverhalten bei 20 MPa unterscheidet. Dehnungen und Dehnungsraten steigen bei höheren Drücken deutlich an. Die Simulationen zeigten, dass eine Annäherung an die Laborergebnisse nur möglich war, wenn zwei unterschiedliche Parametersätze bei dem geringeren Druck (Phase 1) und dem höheren Druck (Phase 2) verwendet wurden. Das Hauptproblem bei der Simulation des Verformungsverhaltens von Salzbeton ist die Beschreibung des instationären viskoplastischen Materialverhaltens (transientes Kriechverhalten). Elastische Verformungen und stationäres Kriechverhalten können durch die verfügbaren Materialeigenschaften angepasst werden. Zur besseren Beschreibung des transienten Materialverhaltens sollte ein konstitutives Modell angepasst oder entwickelt werden. Das hier verwendete konstitutive Modell erlaubte nur eine mathematische Annäherung.

Salzbeton besteht aus der Zementmatrix und den Zuschlagskörnern aus Salzgrus. Diese Struktur und ihre Veränderungen konnten bisher noch nicht wirklich berücksichtigt werden. Weitere Untersuchungen und Entwicklungen in dieser Richtung sind notwendig. Derzeit ist eine Masterarbeit in Bearbeitung, die sich mit der Beschreibung von beiden, den kurz- und den langfristigen, mechanischen Verhaltensweisen unter Berücksichtigung eines erweiterten Plastizitätsmodellansatzes befasst.

Darüber hinaus untersuchte die GRS die Verschlusswirksamkeit von kombinierten Systemen aus Salzbeton-Verschlusselementen und dem umgebenden Steinsalz im Labormaßstab. Bisher wurden die folgenden Ergebnisse erzielt: Bei trockenen Bedingungen und einer moderaten Minimalspannung von bis zu 5 MPa erfolgt die Rückbildung der Wegsamkeiten des integralen Systems nur langsam. Eine möglicherweise vorhandene hochdurchlässige Kontaktzone zwischen dem Verschlusselement und dem Gestein wird zumindest nicht kurzfristig geschlossen.

Bei einem ungeschädigten und damit undurchlässigen Salzbetonelement ist jedoch eine Minimalspannung von 5 MPa ausreichend, um einen Lösungsdurchfluss entlang des Verschlusses zu verhindern. Bei Anwesenheit von Lösung werden Kontaktzone und EDZ schnell verschlossen, was zu einer Gesamtlösungspermeabilität von unter 10^{-20} m^2 führt. Ein vorgeschädigtes und damit durchlässiges Verschlusselement (das vorab triaxial mit Drücken oberhalb der Dilatanzfestigkeitsgrenze beansprucht wurde) wird bei einer Minimalspannung von 5 MPa nicht wiederverschlossen, selbst dann nicht, wenn Lösung vorhanden ist. Bei einem Druck von 10 MPa und einer Versuchsdauer von 6 Monaten werden die Kontaktzone und die EDZ mit der Zeit geschlossen, was zu einer Gesamtpermeabilität unter $1 \cdot 10^{-18} \text{ m}^2$ führt.

Für eine numerische Simulation des Verschluss-/Steinsalzsystems werden die vorhandenen physikalischen Modelle von Steinsalz und Salzbeton auf die hier beschriebenen Experimente angewendet und Simulations-/Verbesserungsläufe durchgeführt, um die Modellvalidierung und Kalibrierung voranzutreiben. Es ist vorgesehen, dass diese hydro-mechanisch gekoppelten Berechnungen im Rahmen des nationalen Projektes LASA-EDZ /FKZ 02E11243/ dokumentiert werden.

7 Acknowledgements

The authors gratefully acknowledge the funding received by the Federal Ministry for Economic Affairs and Energy (BMWi), represented by the Project Management Agency Karlsruhe (PTKA-WTE), contract no. 02E11132 and the funding of the European Commission under FP7 framework programme, contract no. FP7-323273, the DOPAS project.

Special thanks go to Thorsten Hörbrand and Marvin Middelhoff, former student research assistants at GRS, for the great commitment and the necessary persistence in parameter variation for modelling practice.

References

- /ALK 09/ Alkan, H.: Percolation model for dilatancy-induced permeability of the excavation damaged zone in rock salt, *International Journal of Rock Mechanics & Mining Sciences* 46 (2009), 716–724.
- /BGR 03/ Thermomechanisches Verhalten von Salzgestein, Projekt Gorleben, Abschlussbericht, Bundesanstalt für Geowissenschaften und Rohstoffe (BGR), Deutschland 2003.
- /CZA 15/ Czaikowski, O., Hartwig, L., Hertes, U., Jantschik, K., Miehe, R., Müller, J., Schwarzianeck, P.: Full scale demonstration of plugs and seals (DOPAS) Deliverable D3.28 & D5.5: Status report on LASA related laboratory tests and on process modelling activities, Gesellschaft für Anlagen- und Reaktorsicherheit (GRS) gGmbH, GRS-A-3760, Deutschland 2015.
- /CZA 16/ Czaikowski, O., Dittrich, J., Hertes, U., Jantschik, K., Wieczorek, K., Zehle, B.: Full scale demonstration of plugs and seals (DOPAS) Deliverable D3.31: Final technical report on ELSA related testing on mechanical – hydraulic behavior - LASA, Gesellschaft für Anlagen- und Reaktorsicherheit (GRS) gGmbH, GRS-A-3851, Deutschland 2016.
- /FKZ 02E-11132/ Langzeitsicherer Schachtverschluss im Salinar – Kurztitel: LASA. (Förderkennzeichen 02E11132), FuE-Vorhaben der Gesellschaft für Anlagen- und Reaktorsicherheit (GRS) gGmbH
- /FKZ 02E-11243/ Langzeitsicherer Schachtverschluss im Salinar – Ergänzende laborative und modelltheoretische Untersuchungen zum hydro-mechanisch gekoppelten Rekompaktionsverhalten der Auflockerungszone, Kurztitel: LASA-EDZ. (Förderkennzeichen 02E11243), FuE-Vorhaben der Gesellschaft für Anlagen- und Reaktorsicherheit (GRS) gGmbH
- /MID 17/ Middelhoff, M.: Contributions to the simulation of salt concrete: Short-

and long-term mechanical behavior description involving an advanced plasticity model approach. Master Thesis, *in preparation*.

- /MÜL 10/ Müller-Hoeppe, N.: Untersuchungen der Kontaktzone am ASSE-Vordamm – Gesamtinterpretation, Deutsche Gesellschaft zum Bau und Betrieb von Endlagern (DBE), Deutschland 2010.
- /OLI 08/ Olivella, S., Alonso, E. E.: Gas flow through clay barriers, *Geotechnique*, 58 (2008), 157-176.
- /STO 94/ Stockmann, N., Beinlich, A., Droste, J., Flach, D., Gläß, F., Jockwer, N., Krogmann, P., Miehe, R., Möller, J., Schwägermann, F., Wallmüller, R., Walter, F., Yaramanci, U.: Dammbau im Salzgebirge, Abschlussbericht Projektphase II - Berichtszeitraum 01.07.1998 – 31.12.1992, Institut für Tiefenlagerung – Abteilung für Endlagertechnologie, GSF-Bericht 18/94, Forschungszentrum für Umwelt und Gesundheit, Deutschland 1994.
- /UPC 14/ Technische Universität Barcelona (UPC), CODE_BRIGTH User's Guide, Department d'Enginyeria del Terreny, Cartogràfica i Geofísica, Universitat Politècnica de Catalunya, Spanien 2014.
- /VAU 03/ Vaunat, J., Gens, A.: Bond degradation and irreversible strains in soft argillaceous rock, in: 12th Pan American Conference, Soil Mech. Geotech. Engng: Boston, USA, 2003
- /WIE 10/ Wieczorek, K., Förster, B., Rothfuchs, T., Zhang, C.-L., Olivella, S., Kamlot, P., Günther, R.-M., Lerch, C.: THERESA Subproject MOLDAU, Coupled Thermal-Hydrological-Mechanical-Chemical Process in Repository Safety Assessment, Deutsche Gesellschaft zum Bau und Betrieb von Endlagern Technology (DBE Tec), Gesellschaft für Anlagen- und Reaktorsicherheit (GRS) gGmbH, Institut für Gebirgsmechanik (IfG), GRS-262, ISBN: 978-3-939355-37-3, Deutschland 2010.

/ZHA 12/ Zhang, H., Wang, Z., Zheng, Y., Duan, P., Ding, S.: Study on triaxial creep experiment and constitutive relation of different rock salt, Safety Science 50 (2012) 801–805.

Figures

Fig. 2.1	Simplified illustration of the whole dam structure.....	4
Fig. 2.2	Definition of the three devices of a sealing element and identification of the boreholes	4
Fig. 3.1	Salt concrete samples before testing	5
Fig. 3.2	Principle of triaxial compression tests with permeability measurement	6
Fig. 3.3	Stress evolution of a salt concrete sample under isostatic compaction	8
Fig. 3.4	Strain evolution of a salt concrete sample under isostatic compaction	8
Fig. 3.5	Isostatic pre-compaction behaviour of a salt concrete sample	9
Fig. 3.6	Stress-strain behaviour of a salt concrete sample B4KK4 P10 deformed by deviatoric loading at confining stress of 3 MPa.....	10
Fig. 3.7	Strain-permeability behaviour of a salt concrete sample B4KK4 P10 deformed by deviatoric loading at confining stress of 3 MPa.....	10
Fig. 3.8	Stress-strain curves obtained on four of the eight salt concrete samples at different confining stresses. <i>Curve of sample B4KK1 0.68 has been cut at axial strains below 2%, as multiple reloading cycles were executed in this interval, which would confuse the illustration</i>	12
Fig. 3.9	Stress-strain curves obtained on the salt concrete samples at different confining stresses	12
Fig. 3.10	Dilatancy boundary, onset of gas flux and failure of the tested samples compared with data from /CZA 15/. Range of values is indicated by dashed lines.....	13
Fig. 3.11	Stress-strain behaviour of salt concrete sample B4KK4 P9 deformed by deviatoric loading at multiple confining stresses.....	14
Fig. 3.12	Permeability development of salt concrete sample B4KK4 P9 deformed by deviatoric loading at multiple confining stresses. Deformation path is delineated by the black line	15

Fig. 3.13	Permeability as a function of volumetric strain. Laboratory data for confining pressures of 1-3 MPa are compared with calculated permeabilities	17
Fig. 3.14	Samples not considered for porosity-permeability relationship. Sample B4KK1 0.68 shows no development at all; ultimate permeability of sample B4KK4 P10 is too low to allow a prediction by the equations; initial permeability of sample B4KK1 1.38 is probably too high and is therefore not able to be modelled by the relations.....	18
Fig. 3.15	Development of permeability for the multi-stage triaxial test	19
Fig. 3.16	Rig for uniaxial creep tests on five samples one upon another.....	20
Fig. 3.17	Long-term uniaxial creep behaviour of five salt concrete samples under multi-step loads – axial and radial strains	22
Fig. 3.18	Long-term uniaxial creep behaviour of five salt concrete samples under multi-step loads – stress, temperature and relative humidity evolution	22
Fig. 3.19	Long-term uniaxial creep behaviour of salt concrete sample no.1048 under multi-step loads – axial strain and derived creep rates.....	24
Fig. 3.20	Long-term uniaxial creep behaviour of salt concrete sample no.1049 under multi-step loads – axial strain and derived creep rates.....	24
Fig. 3.21	Long-term uniaxial creep behaviour of salt concrete sample no.1050 under multi-step loads – axial strain and derived creep rates.....	25
Fig. 3.22	Long-term uniaxial creep behaviour of salt concrete sample no.1051 under multi-step loads – axial strain and derived creep rates.....	25
Fig. 3.23	Long-term uniaxial creep behaviour of salt concrete sample no.1052 under multi-step loads – axial strain and derived creep rates.....	26
Fig. 3.24	Steady-state creep rates obtained on five salt concrete samples as a function of applied uniaxial loads	26
Fig. 3.25	Steel cylinder for individual oil pressure built-up on a salt concrete sample.....	27

Fig. 3.26	Long-term triaxial creep behaviour of four salt concrete samples under multi-step loads – stress and temperature	29
Fig. 3.27	Long-term triaxial creep behavior of four salt concrete samples under multi-step loads – axial strains	29
Fig. 3.28	Long-term triaxial creep behaviour of salt concrete sample no.1060 under multi-step loads – axial strain and derived creep rates.....	31
Fig. 3.29	Long-term triaxial creep behaviour of salt concrete sample no.1061 under multi-step loads – axial strain and derived creep rates.....	31
Fig. 3.30	Long-term triaxial creep behaviour of salt concrete sample no.1062 under multi-step loads – axial strain and derived creep rates.....	32
Fig. 3.31	Long-term triaxial creep behaviour of salt concrete sample no.1063 under multi-step loads – axial strain and derived creep rates.....	32
Fig. 3.32	Rig for triaxial creep tests with temperature control.....	33
Fig. 3.33	Deformation behaviour of the intact concrete sample at ambient and elevated temperatures	34
Fig. 3.34	Deformation behaviour of the tested concrete samples at ambient and elevated temperatures - standardized curve illustration	35
Fig. 3.35	Deformation behaviour of the intact concrete sample at ambient and elevated temperatures– derived strain rates	36
Fig. 3.36	Deformation behaviour of the tested concrete samples at ambient and elevated temperatures - standardized curve illustration showing derived strain rates	37
Fig. 3.37	Hollow salt cylinder, salt concrete core and salt slurry (left); complete combined sample (right)	38
Fig. 3.38	Principal sketch of the modified Hassler cell for determining gas and water permeability.....	39
Fig. 3.39	Coated test sample (left); test equipment (right)	39
Fig. 3.40	Gas permeability of salt concrete cores and salt cylinders before assembly of combined samples	41

Fig. 3.41	Permeability of combined samples as a function of confining stress	43
Fig. 3.42	Permeability to brine of the sample with damaged seal element as a function of time	44
Fig. 4.1	Model of the salt concrete specimens for TC-Test for the numerical calculation using CODE_BRIGHT.....	48
Fig. 4.2	Specimen for the TC-Test: Boundary conditions for numerical calculation using CODE_BRIGHT.....	50
Fig. 4.3	Nodes on the specimen, at which stresses and displacements were detected.....	54
Fig. 4.4	Results of Exercise TC 1. Here LINEAR ELASTICITY law and VISCOPLASTICITY model are used. Axial load is 44 MPa.....	55
Fig. 4.5	Results of Exercise TC 2. Here LINEAR ELASTICITY law and VISCOPLASTICITY model are used. Parameters a_2 , a_4 and a_6 are set to zero. a_1 is varied. For further calculations $a_1 = 2.05$ is chosen (green curve)	56
Fig. 4.6	Comparison of calculation results of Exercise TC 2 and TC 3 with and without DISLOCATION CREEP law. The results confirm that DISLOCATION CREEP law is only considered by longer time periods. Calculations, which were executed with DISLOCATION CREEP law are marked with "DC"	58
Fig. 4.7	Calculation results of Exercise TC 2 and a radial stress of 3 MPa. The pink curve shows the results without dilatancy, the green one with dilatancy. The onset of dilatancy is defined as the start of deviation of the curve with dilatancy to the linear curve without dilatancy	59
Fig. 4.8	Calculation results of Exercise TC 2 and a radial stress of 2 MPa. The pink curve shows the results without dilatancy, the green one with dilatancy. The onset of dilatancy is defined as the start of deviation of the curve with dilatancy to the linear curve without dilatancy	60

Fig. 4.9	Calculation results of Exercise TC 2 and a radial stress of 1 MPa. The pink curve shows the results without dilatancy, the green one with dilatancy. The onset of dilatancy is defined as the start of deviation of the curve with dilatancy to the linear curve without dilatancy	61
Fig. 4.10	Model of the salt concrete specimens for UCc-Test for the numerical calculation using CODE_BRIGHT, showing geometry and meshing details	63
Fig. 4.11	Specimen for the UCc-Test: Depiction of conditions for numerical calculation using CODE_BRIGHT	64
Fig. 4.12	Comparison between the results of the laboratory UCc-Test and the calculation of UCc-Test using LINEAR ELASTICITY law and DISLOCATION CREEP law by a pre-exponential parameter of $2.08 \cdot 10^{-6}$ (creep class 5)	68
Fig. 4.13	Comparison between the results of the laboratory UCc-Test and the modelling using LINEAR ELASTICITY law and DISLOCATION CREEP with various pre-exponential parameters corresponding to creep classes 0 to 6	69
Fig. 4.14	Average determination of strain rates for specimen SC(1048)	71
Fig. 4.15	Average strain rates of the various specimen of the laboratory UCc-Test and calculated strain rate using LINEAR ELASTICITY law and DISLOCATION CREEP with a pre-exponential parameter of $0.26e-6$ (creep class 2)	71
Fig. 4.16	Variation of pre-exponential parameter in first stress level of 5 MPa	73
Fig. 4.17	Variation of pre-exponential parameter in second stress level of 10 MPa	73
Fig. 4.18	Variation of pre-exponential parameter in third stress level of 20 MPa	74
Fig. 4.19	Calculation using an individual pre-exponential parameter for each stress level	75
Fig. 4.20	Strain rates for calculation using different pre-exponential parameters in each stress level	75

Fig. 4.21	Calculation of the UCc-Test using the LINEAR ELASTICITY law and VISCOPLASTICITY model with parameters of Exercise TC 2	78
Fig. 4.22	Development of porosity using the LINEAR ELASTICITY law and VISCOPLASTICITY model with parameters of Exercise TC 2	78
Fig. 4.23	Exercise UCc 3a-b - Variation of parameter a_1 and a_2 plus variation of the pre-exponential parameter (PP)	79
Fig. 4.24	Exercises UCc 3a-b - Development of porosity for calculations in phase 2.....	80
Fig. 4.25	Exercise UCc 3c - Variation of parameter a_1 and a_2 plus variation of the pre-exponential parameter (PP) by using LINEAR ELASTIC LAW, DISLOCATION CREEP law and VISCOPLASTICITY model.....	81
Fig. 4.26	Exercises UCc 3c-d - Development of porosity for calculations in phase 2.....	82
Fig. 4.27	Depiction of the deformation behaviour by considering LINEAR ELASTICITY LAW, DISLOCATION CREEP law and VISCOPLASTICITY model after Exercise UCc 3d	83
Fig. 4.28	Strains rates in third stress level using parameters of Exercise UCc 3d	84
Fig. 4.29	Exercise UCc 4a - Variation of viscosity (A)	85
Fig. 4.30	Exercise UCc 4a - Development of porosity by varying viscosity (A).....	86
Fig. 4.31	Exercise UCc 4b - Variation of parameter a_1	87
Fig. 4.32	Exercise UCc 4b - Development of porosity.....	88
Fig. 4.33	Exercise UCc 4c - Variation of parameter a_2	89
Fig. 4.34	Exercise UCc 4c - Development of porosity	90
Fig. 4.35	Depiction of the deformation components, which results from the parameter variations before and the combination of adaptation in phase 1 and phase 2. Deformations consist of elastic deformations (HOOKE), transient creep (TC), dislocation creep (DC) and dilatancy (DI)	92

Fig. 4.36	Exercise UCc5 - Comparison between strain rates of laboratory tests and calculation results	93
Fig. 4.37	Exercise UCc 5 - Comparison between strain rates versus axial strain of laboratory tests and calculation results.....	93
Fig. 4.38	Model layout in GiD for numerical calculation of the TCc-Test, showing geometry and meshing details	95
Fig. 4.39	Comparison between the results of the laboratory TCc-Test and the result of numerical calculation using LINEAR ELASTICITY, DISLOCATION CREEP and VISCOPLASTICITY law with parameters from /CZA 15/	101
Fig. 4.40	Comparison between the results of the laboratory TCc-Test and modelling, using LINEAR ELASTICITY and DISLOCATION CREEP law with various pre-exponential parameters corresponding to creep classes 0 to 3.....	102
Fig. 4.41	Strain rates for numerical calculations using different pre-exponential parameters in comparison with laboratory data (circles)	103
Fig. 4.42	Comparison between the results of the laboratory TCc-Test and modelling, using LINEAR ELASTICITY, DISLOCATION CREEP and VISCOPLASTICITY law with a_2 between 0.9 and 0.7	104
Fig. 4.43	Strain rates for numerical calculations varying parameter a_2 between 0.9 and 0.7.....	104
Fig. 4.44	Strain rates of numerical calculations for parameter W_{d0} between 2.2 and 1.7	106
Fig. 4.45	Strain rates of numerical calculations for parameter a_4 between 0.7 and 0.5	107
Fig. 4.46	Comparison between the results of the laboratory TCc-Test and modelling, using LINEAR ELASTICITY, DISLOCATION CREEP and VISCOPLASTICITY law with a_4 between 0.7 and 0.5	108
Fig. 4.47	Comparison between the results of the laboratory TCc-Test and modelling in phase 1 and 2, using LINEAR ELASTICITY, DISLOCATION CREEP and VISCOPLASTICITY law.....	109

Fig. 4.48	Comparison between the results of the laboratory TCc-Test and modelling in phase 3, using LINEAR ELASTICITY, DISLOCATION CREEP and VISCOPLASTICITY law.....	110
Fig. 4.49	Measured strain rates (colored points) versus strain rates from numerical calculation (red line) in phase 2 and 3	110
Fig. 4.50	Porosity development in phase 2 and 3 for numerical calculation	111
Fig. 4.51	Different composed materials (Argillaceous rock, Conventional concrete and Salt concrete) and their similarities (Matrix, Bonds, and Voids)	113

Tables

Tab. 2.1	Composition of salt concrete type „Asse“ related to 1 m ³ /MÜL 10/	3
Tab. 3.1	Test samples that were subjected to confining stresses of 1-5 MPa	9
Tab. 4.1	Parameters for VP. Constant and varied parameters are marked and their influence on the process of calculation is described so far as known. Values, marked with *, were only varied by calculation of the triaxial compression test: here the values were set to zero	47
Tab. 4.2	Values of initial conditions for TC-Test.....	49
Tab. 4.3	Material properties for LINEAR ELASTICITY law.....	50
Tab. 4.4	Material properties for DISLOCATION CREEP law.....	51
Tab. 4.5	Parameter for VISCOPLASTICITY model for description of transient creep and dilatancy of rock salt.....	51
Tab. 4.6	Solid phase properties for calculation using CODE_BRIGHT.....	51
Tab. 4.7	Calculation time steps of calculation for the compaction phase of TC-Test with different radial stresses.....	53
Tab. 4.8	Used constitutive laws for modelling salt concrete TC behaviour (varied parameters are marked in red).....	53
Tab. 4.9	Used constitutive laws for modelling salt concrete TC behaviour (varied parameters are marked in red).....	55
Tab. 4.10	Used constitutive laws for modelling salt concrete TC behaviour (varied parameters are marked in red).....	57
Tab. 4.11	Final parameters used for the Linear Elasticity law and VISCOPLASTICITY model in TC-Test.....	62
Tab. 4.12	Finally used parameters for the Linear Elasticity law.....	65
Tab. 4.13	Material properties for DISLOCATION CREEP law of saline materials	65
Tab. 4.14	Parameter for VISCOPLASTICITY model for description of transient creep and dilatancy of salt concrete.....	65

Tab. 4.15	Variation of creep classes and appropriate pre-exponential parameters for first calculations /BGR03/.....	66
Tab. 4.16	Time steps of calculation at UCc-Test.....	67
Tab. 4.17	Exercise UCc 1 - Active constitutive laws for salt concrete are colored. Changed respectively varied parameters are marked red	68
Tab. 4.18	Exercise UCc 2 - Active constitutive laws for salt concrete are colored. Changed respectively varied parameters are marked red	72
Tab. 4.19	Exercise UCc 3a - Active constitutive laws for salt concrete are colored. Changed respectively varied parameters are marked red	77
Tab. 4.20	Exercise UCc 3b - Active constitutive laws for salt concrete are colored. Changed respectively varied parameters are marked red	79
Tab. 4.21	Exercise UCc 3c - Active constitutive laws for salt concrete are colored. Changed respectively varied parameters are marked red	80
Tab. 4.22	Exercise UCc 3d - Active constitutive laws for salt concrete are colored. Changed respectively varied parameters are marked red	82
Tab. 4.23	Exercise UCc 4a - Active constitutive laws for salt concrete are colored. Changed respectively varied parameters are marked red.	85
Tab. 4.24	Exercise UCc 4b - Active constitutive laws for salt concrete are colored. Changed respectively varied parameters are marked red	87
Tab. 4.25	Exercise UCc 4c - Active constitutive laws for salt concrete are colored. Changed respectively varied parameters are marked red	88
Tab. 4.26	Exercise UCc 5 - Active constitutive laws for salt concrete are colored. Changed respectively varied parameters are marked red	91
Tab. 4.27	Values of initial conditions for TCc-Test.....	96
Tab. 4.28	Final used parameters for the Linear Elasticity law	97
Tab. 4.29	Material properties for DISLOCATION CREEP law of saline materials	97
Tab. 4.30	Parameters for the VISCOPLASTICITY model from /CZA 15/; triaxial creep test).....	97

Tab. 4.31	Solid phase properties for calculation using CODE_BRIGHT.....	98
Tab. 4.32	Time steps of calculation at TCc-Test; colors represent σ_1 and σ_3 at the end of each interval.....	99
Tab. 4.33	Parameters for numerical calculations in Exercise 1	100
Tab. 4.34	Exercise 2 - varied parameters are marked red	102
Tab. 4.35	Exercise 3a - varied parameters are marked red	103
Tab. 4.36	Exercise 3b - varied parameters are marked red	105
Tab. 4.37	Exercise 3c - varied parameters are marked red.....	107
Tab. 4.38	Parameters for numerical calculation of Exercise 4.....	108

**Gesellschaft für Anlagen-
und Reaktorsicherheit
(GRS) gGmbH**

Schwertnergasse 1
50667 Köln
Telefon +49 221 2068-0
Telefax +49 221 2068-888

Forschungszentrum
Boltzmannstraße 14
85748 Garching b. München
Telefon +49 89 32004-0
Telefax +49 89 32004-300

Kurfürstendamm 200
10719 Berlin
Telefon +49 30 88589-0
Telefax +49 30 88589-111

Theodor-Heuss-Straße 4
38122 Braunschweig
Telefon +49 531 8012-0
Telefax +49 531 8012-200

www.grs.de